The physics of the interstellar medium

A. C. Raga, J. Cantó

April 10, 2012

Part I

Physical processes in the ISM

Chapter 1

Photoionised Regions

1.1 Indroduction

Starting with the paper of Huggins ([10], "On the spectrum of the great nebula in Orion..."), photoionised regions have been one of the dominant topics in research on the ISM. Photoionised regions in our galaxy fall into two main categories :

1. H II regions : these are regions of the ISM in which massive stars have formed, and the far-UV radiation from these stars photoionises the surrounding gas. The brightest and best studied region is the Orion Nebula (see Fig. 1.1).

2. Planetary nebulae : these are evolved stars which have ejected most of their material in the form of winds. The remaining, hot core of the star emits far-UV radiation which photoionises the still outflowing material which was previously ejected from the star. An example of this kind of object is the Helix Nebula (see Fig. 1.2).

1.2 The ionising photon rate produced by the central star

1.2.1 General considerations

The fundamental process giving rise to the "photoionised region" phenomenon is the production of far-UV photons by the "central source" of the nebula.

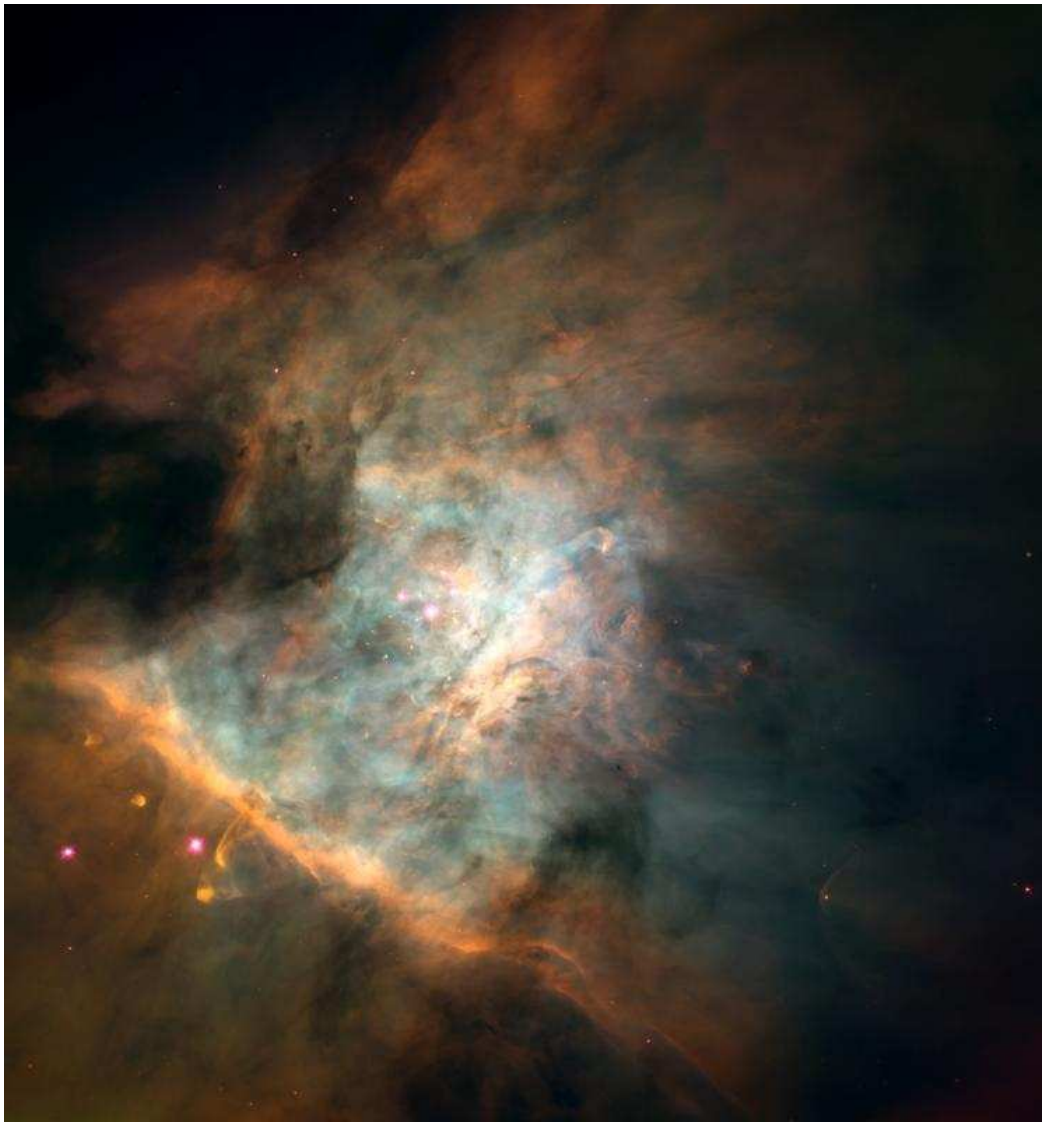

Figure 1.1: Example of an H II region: the Orion Nebula

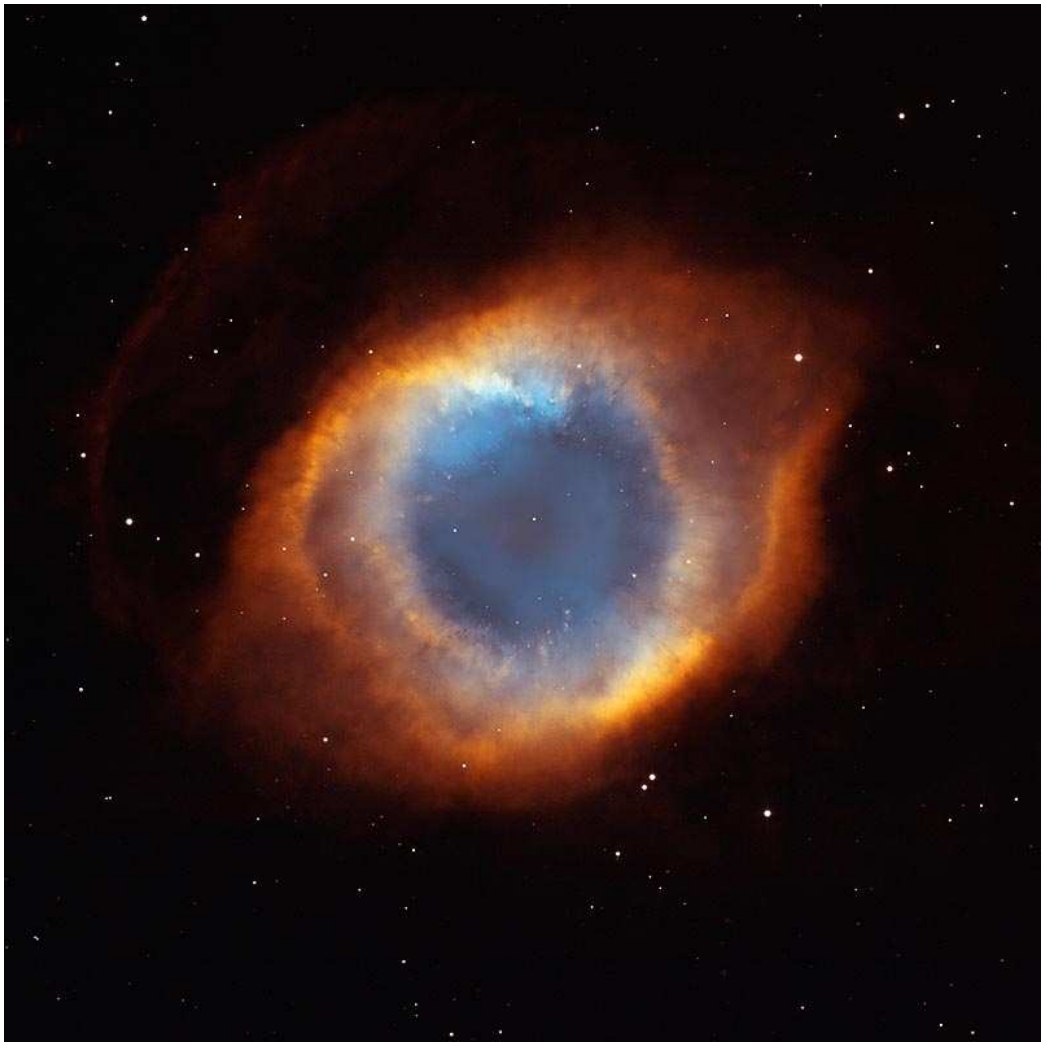

Figure 1.2: Example of a planetary nebula: the Helix

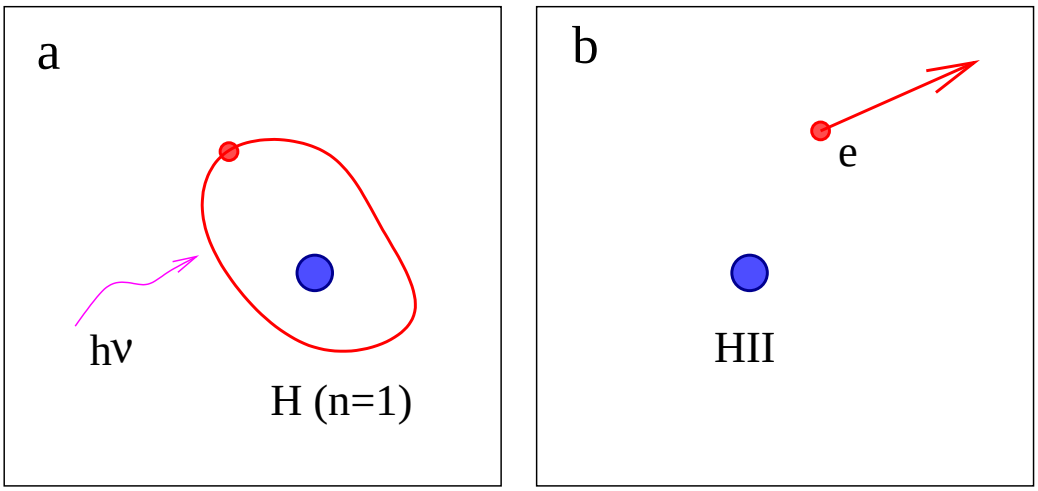

Figure 1.3: Schematic diagram showing the process of H photoionisation. **a.** in the initial state we have a photon of energy $h\nu$ hitting an H atom in the $n = 1$ state. **b.** after the interaction, we have an H nucleus (i. e., an HII ion) and a free electron with a kinetic energy $h\nu - \chi_H$.

This "central source" could in principle be one or several stars which produce the photoionisation.

In the ISM, the gas is mostly composed of hydrogen (H), and most of the H atoms are in the ground, $n = 1$ state. The energy difference between an electron in this state, and the lowest possible energy of a free electron is the "ionisation potential" for the $n = 1$ level of H : $\chi_H = 13.6$ eV. In order to photoionise an electron from this level, it is necessary to have photons with energies $h\nu \geq \chi_H$.

The photoionisation process is shown schematically in Fig. 1.3. A photon of energy $h\nu \geq \chi_H$ (where h is the Planck constant and ν the frequency of the photon) hits an H atom in the $n = 1$ state. The photon is absorbed, and the electron has a transition to a free state with a kinetic energy $E_k = m_e {v_e}^2/2 = h\nu - \chi_H$ (where m_e is the mass and v_e the velocity of the free electron).

Let us call L_ν the luminosity per unit frequency emitted by the central source of the nebula (the total luminosity of the star being $L = \int_0^\infty L_\nu d\nu$). The total number of ionising photons (i. e., of photons with frequencies

larger than $\nu_H = \chi_H/h$) emitted per unit time is then given by :

$$S_* = \int_{\nu_H}^{\infty} \frac{L_\nu}{h\nu} d\nu \,. \tag{1.1}$$

1.2.2 Sources emitting a black body spectrum

Let us consider that we have a star that emits a black body spectrum in the Wien limit ($h\nu/kT_* \gg 1$, where T_* is the black body temperature of the source). The luminosity per unit frequency emitted by the star then is :

$$L_\nu = 4\pi {R_*}^2 (\pi B_\nu) \approx 4\pi {R_*}^2 \frac{2\pi h\nu^3}{c^2} \, e^{-h\nu/kT_*} \,, \tag{1.2}$$

where c is the speed of light and B_ν is the Planck distribution. Using this form for the frequency-dependent luminosity L_ν, eq. 1.1 can be integrated analytically to obtain :

$$S_{*,bb} = \frac{8\pi^2 {R_*}^2}{c^2} \left(\frac{kT_*}{h}\right)^3 \left({x_0}^2 + 2x_0 + 2\right) e^{-x_0} \,, \tag{1.3}$$

where $x_0 \equiv h\nu_H/kT_*$. This equation gives a simple prescription for calculating the ionising photon rate S_* as a function of the radius R_* and the black body temperature T_* of the source.

1.2.3 Sources with more realistic photon distributions

In principle, the emission from a stellar atmosphere can have quite strong deviations from a black body spectrum. It is possible to integrate eq. 1.1 using the results obtained from model atmospheres. Table 1.1 gives the effective temperatures and radii for massive main sequence stars (as a function of the spectral class), and the ionising photon rates S_* computed from appropriate atmosphere models.

Table 1.1 gives the results obtained from such a computation of S_* (including also the radius R_*, the luminosity L, the mass M, the terminal wind velocity v_w and the mass loss rate $\dot{M}$) for massive stars with different effective temperatures T_{eff}, taken from [23].

In Fig. 1.4, we see the values of S_* from Table 1.1 as a function of T_{eff}, as well as the $S_{*,bb}$ obtained from eq. 1.1 for the same values of $T_* = T_{eff}$ and R_*. It is clear that for $T_{eff} > 4 \times 10^4$ K, the two values agree well, though

Table 1.1: Ionising photon rate and other parameters for main sequence (luminosity class V) stars (from [23])

Spectral Type	T_{eff} [K]	R_* [$R_\odot$]	$\log_{10} L$ [$L_\odot$]	M [$M_\odot$]	v_w [km s^{-1}]	$\dot{M}$ [$M_\odot$yr^{-1}]	$\log_{10} S$ [s^{-1}]
O3	51230	13.2	6.04	87.6	3552	2.7E-6	49.87
O4	48670	12.3	5.88	68.9	3266	1.8E-6	49.68
O4.5	47400	11.8	5.81	62.3	3138	1.4E-6	49.59
O5	46120	11.4	5.73	56.6	3026	1.1E-6	49.49
O5.5	44840	11.0	5.65	50.4	2903	8.9E-7	49.39
O6	43560	10.7	5.57	45.2	2784	7.2E-7	49.29
O6.5	42280	10.3	5.49	41.0	2666	5.6E-7	49.18
O7	41010	10.0	5.40	37.7	2543	4.5E-7	49.06
O7.5	39730	9.6	5.32	34.1	2428	3.5E-7	48.92
O8	38450	9.3	5.24	30.8	2313	2.7E-7	48.75
O8.5	37170	9.0	5.15	28.0	2194	2.1E-7	48.61
O9	35900	8.8	5.06	25.4	2083	1.7E-7	48.47
O9.5	34620	8.5	4.97	23.3	1972	1.3E-7	48.26
B0	33340	8.3	4.88	21.2	1853	1.0E-7	48.02
B0.5	32060	8.0	4.79	19.3	1747	7.8E-8	47.71

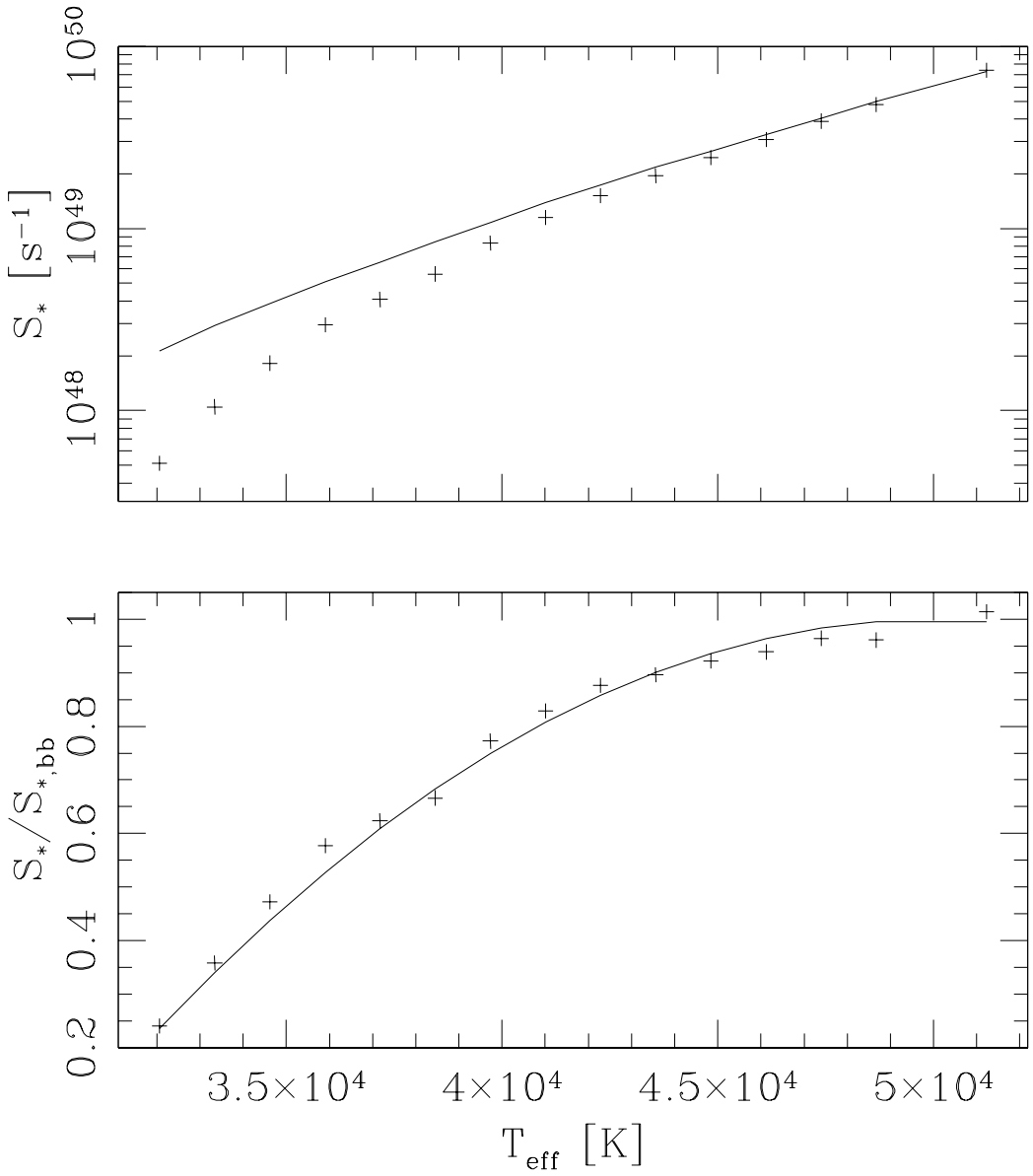

Figure 1.4: Ionising photon rate S_* as a function of T_{eff} for massive main sequence stars. Top: the crosses are the values taken from Table 1.1, and the solid line gives the $S_{*,bb}$ computed for a black-body source. Bottom: the ratio $S_*/S_{*,bb}$ as a function of T_{eff} (crosses) and the fit described in the text.

not so for lower temperatures. This can be seen in the lower frame of Fig. 1.4, which plots the $S_*/S_{*,bb}$ ratio as a function of T_{eff}. This ratio can be fitted with a quadratic polinomial of the form :

$$\frac{S_*}{S_{*,bb}}(T_{eff}) = 2.375\,t(1-t/10) - 4.938\,; \quad t = T_{eff}/10^4\mathrm{K}\,, \tag{1.4}$$

which is shown as a solid curve in Fig. 1.4. This fit has been made for temperatures in the range $30000 < T_{eff} < 50000$ K. It is then possible to use Eq. 1.4 to calculate a correction factor by which one can multiply Eq. 1.1 in order to obtain an ionisation photon rate closer to the one predicted from stellar atmosphere models.

In order to give a complete prescription of how to compute the ionising photon rate for luminous stars along the main sequence, we note that the values of R_* as a function of T_{eff} can be fitted by :

$$\frac{R_*}{R_\odot}(T_{eff}) = 8.225 - 1.773\,t + 0.535\,t^2\,; \quad t = T_{eff}/10^4\mathrm{K}\,. \tag{1.5}$$

Therefore, in order to obtain values of S_* that basically represent an interpolation in between the ones of Table 1.1, for a given T_{eff} one can first compute R_* from Eq. 1.5, then insert the values of T_{eff} and R_* into Eq. 1.1 to obtain $S_{*,bb}$, and finally multiply by the correction factor given by Eq. 1.4 in order to obtain the ionising photon rate S_*.

1.3 Strömgren sphere

The simplest possible model for an H II region can be constructed as follows. We consider a star with an ionising photon rate S_* which is immersed in a homogeneous medium of temperature T and H number denisty n_H. We assume that the star photoionises the gas within a sphere of radius R_S, and that the transition between ionised interior and neutral exterior occurs over a distance $\Delta R \ll R_S$. The balance equation which determines the size of the "Strömgren sphere" is

$$S_* = \dot{N}_{rec}\,, \tag{1.6}$$

where $\dot{N}_{rec}$ is the total number of recombinations per unit time within the sphere. The number of recombinations per unit volume $\dot{n}_{rec}$ is given by

$$\dot{n}_{rec} = n_e\, n_{HII} \alpha_H(T)\,, \tag{1.7}$$

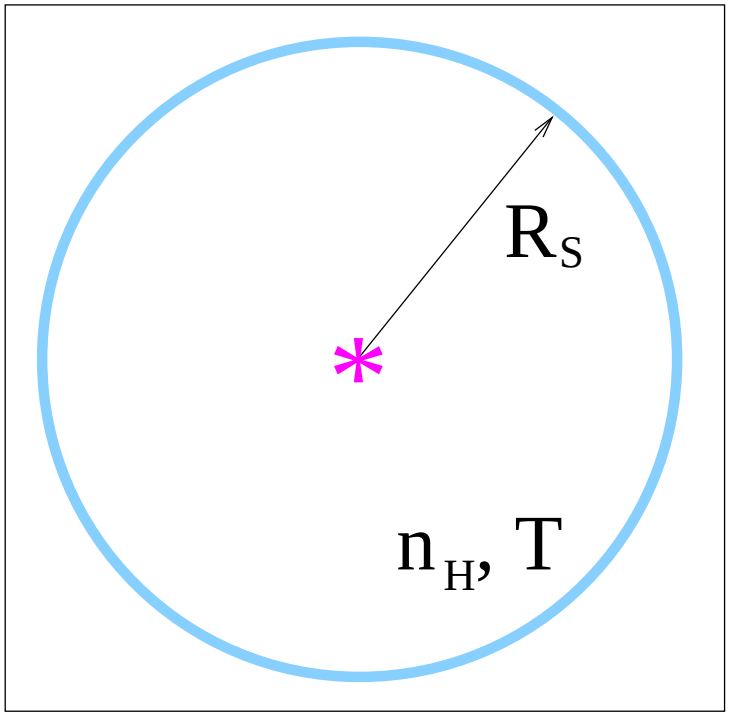

Figure 1.5: Schematic diagram showing the configuration of a spherical "Strömgren sphere" produced by a star with an ionising photon rate S_* which is immersed in a homogeneous medium of temperature T and H atom+ion number density n_H. Within the ionised sphere ($R < R_S$), the gas is almost fully ionised, so that $n_e \approx n_{HII} \approx n_H$. For $R > R_S$, $n_e \approx n_{HII} \approx 0$ and $n_{HI} \approx n_H$.

where the recombination coefficient $\alpha_H(T)$ is described in detail below. Within the ionised sphere, most of the electrons come from the ionised H, so that we can set $n_e \approx n_{HII} \approx n_H$. Then, the integral of the Eq. 1.7 over the volume of the sphere (obtained just by multiplying by $4\pi {R_S}^3/3$, as the medium is assumed to be homogeneous), and substituting into Eq. 1.6 one obtains

$$S_* = \frac{4\pi}{3} {R_S}^3 {n_H}^2 \alpha(T) \;\; \rightarrow \;\; R_S = \left[\frac{3S_*}{4\pi {n_H}^2 \alpha(T)} \right]^{1/3} , \tag{1.8}$$

where the latter equation gives the "Strömgren radius" R_S of the ionised sphere.

The recombination coefficient $\alpha(T)$ is calculated as a sum over the recombination coefficients to all of the energy states of H :

$$\alpha_A(T) = \sum_{n=1}^{\infty} \alpha_n(T) \, , \tag{1.9}$$

and the recombination coefficient to state n is given by

$$\alpha_n(T) = \int_0^{\infty} \sigma_n(v) \, v f(v,T) dv \, , \tag{1.10}$$

where the integral of the product of the Maxwell-Boltzmann distribution $f(v,T)$, the effective cross section for the radiative recombination process $\sigma_n(v)$ and the velocity v is carried out over all of the possible values for the velocity of the electrons.

Actually, the electrons which recombine directly to the ground, $n = 1$ state emit a Lyman continuum photon with energy greater than 13.6 eV. Therefore, these photons contribute to the photoionisation rate, ionising H atoms in other regions of the Strömgren sphere. Because of this, a better approximation is to not consider the recombinations to $n = 1$ in the recombination coefficient, as these are "inefficient recombinations" leading to a new photoionisation within the sphere. It is therefore better to put $\alpha(T) = \alpha_B(T)$ in Eq. 1.8, where

$$\alpha_B(T) = \sum_{n=2}^{\infty} \alpha_n(T) \, , \tag{1.11}$$

is called the "case B" recombination coefficient of H (the "case A" recombination coefficient being given by Eq. 1.9).

Tabulations of the recombination coefficients as a function of gas temperature T are given by Osterbrock (1989). It is possible to carry out simple power law fits to these tabulations, from which one obtains :

$$\alpha_A(T) = 4.15 \times 10^{-13} \mathrm{cm}^3 \mathrm{s}^{-1} \left(\frac{10^4 \mathrm{K}}{T} \right)^{0.72} , \tag{1.12}$$

$$\alpha_B(T) = 2.56 \times 10^{-13} \mathrm{cm}^3 \mathrm{s}^{-1} \left(\frac{10^4 \mathrm{K}}{T} \right)^{0.83} . \tag{1.13}$$

For the calculation of a Strömgren radius, one then sets $\alpha_H(T) \approx \alpha_B(10^4 \mathrm{K})$ in Eq. 1.8. As we shall see below, this is a reasonable value to take for the recombination coefficient because temperatures of H II regions always have values $T \sim 10^4$ K.

1.4 Strömgren regions

1.4.1 Generalization of the Strömgren sphere analysis

The simple argument of balancing the ionising photon rate S_* with the total recombination rate can be applied to more general cases than the one of a photoionised region in a homogeneous medium. In the following, three examples are presented showing how to carry out a "Strömgren region" analysis of a stratified H II region, of an H II region in which the star moves supersonically with respect to the surrounding medium, and of an expanding, constant density H II region.

1.4.2 The photoionisation of a constant velocity wind

Let us consider a stationary wind with a constant velocity v_w, independent of the spherical radius R. The mass $\dot{M}$ going through a spherical surface of radius R is

$$\dot{M} = 4\pi R^2 \rho_w v_w \, , \tag{1.14}$$

where ρ_w is the density of the wind at a radius R. For a stationary wind $\dot{M}$ is independent of R, and is equal to the rate of mass loss from the star. Eq. 1.14 then gives the atom+ion number density

$$n_w(R) = \frac{\rho_w(R)}{m} = \frac{\dot{M}}{4\pi m v_w R^2} \, , \tag{1.15}$$

where m is the mass per atom or ion ($= m_H$ for a pure H wind, and $= 1.3 m_H$ for a wind of 90% H and 10% He).

The balance between ionising and recombination rates (see Eq. 1.8 for the case of a homogeneous medium) can be written as

$$S_* = \int_{R_*}^{R_S} n_w^2(R) \alpha_H(T)\, 4\pi R^2 dR\,, \tag{1.16}$$

where $n_w(R)$ is given by Eq. 1.15, R_* is the stellar radius and R_S is the outer radius of the photoionised region. We now assume that the wind is isothermal, and take $\alpha_H(T) \approx \alpha_B(10^4\mathrm{K})$ out of the integral.

Eq. 1.16 can be integrated and then inverted to obtain

$$\frac{R_S}{R_*} = \left(1 - \frac{S_*}{S_0}\right)^{-1} \;; \quad S_0 \equiv \frac{\dot{M}^2 \alpha_B}{4\pi R_* {v_w}^2 m^2}\,, \tag{1.17}$$

which is plotted in Fig. 1.6. It is clear that $R_S \to \infty$ for $S_* \to S_0$. For $S_* > S_0$, the recombination rate in the full volume of the wind (out to $R \to \infty$) is smaller than the ionising photon rate S_*.

From Table 1.1, one can check numerically that $S_*/S_0 \gg 1$ for all massive main sequence stars. Therefore, these stars only use a very small fraction of their ionising photon production in order to fully photoionise their own winds.

1.4.3 Cometary H II region

Let us consider a star with an ionising photon rate S_* moving at a velocity v_* through a homogeneous medium of density n_H. We will assume that the star has no wind, and that the formation of the H II region does not lead to any modification of the initially homogeneous density of the surrounding medium. This latter assumption is valid provided that v_* is highly supersonic.

If we stand in a reference system travelling with the star, the problem corresponds to a stationary star and an environment that travels at a velocity v_* towards it. This configuration is shown in Fig. 1.7.

We place an axis directed towards the impinging flow (see Fig. 1.7) and consider the spherical radius R and cylindrical radius r of the edge of the H II region, both dependent on the angle θ between the point on the edge of the H II region and the axis (the spherical and cylindrical radii are related through $r = R \sin\theta$). The angle θ subtends a solid angle $\Delta\Omega = 2\pi(1 - \cos\theta)$.

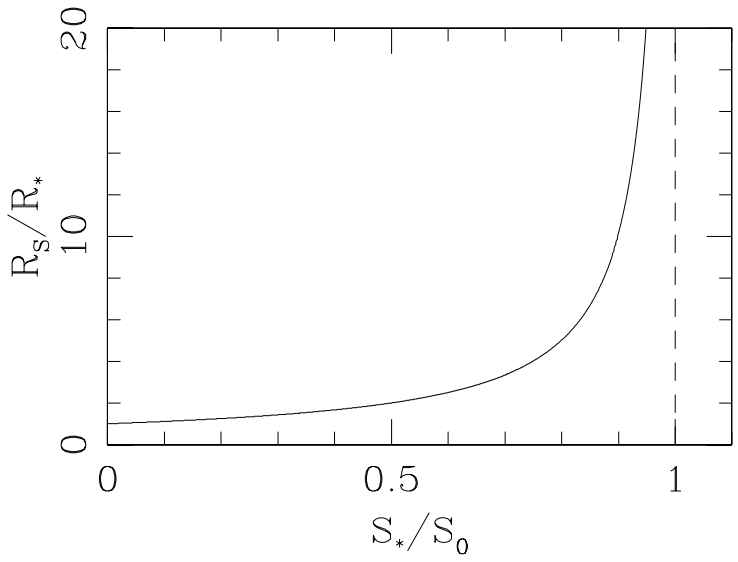

Figure 1.6: Solution for the Strömgren radius of a region with an R^{-2} density stratification. The Strömgren radius goes to infinity for $S_*/S_0 \rightarrow 1$ (see the text).

Let us now consider the ionising photons $S_*\Delta\Omega/(4\pi)$ emitted per unit time by the source into the solid angle $\Delta\Omega$. These photons have to balance the recombinations $\dot{N}_{rec}(\theta)$ in the ionised volume $V(\theta)$ subtended by the angle θ and also have to ionise the neutrals that enter from the upstream direction into the ionised region $\dot{N}_{in}(\theta)$ per unit time into this volume. In other words :

$$\frac{S_*}{4\pi}\Delta\Omega = \dot{N}_{rec}(\theta) + \dot{N}_{in}(\theta)\,, \tag{1.18}$$

where $\Delta\Omega = 2\pi(1-\cos\theta)$ is the solid angle subtended by the angle θ.

The total number of recombinations per unit time can be written as

$$\dot{N}_{rec}(\theta) = {n_H}^2\alpha_H V(\theta)\,; \quad V(\theta) = \frac{2\pi}{3}\int_0^\theta R^3\sin\theta\,d\theta\,, \tag{1.19}$$

where $V(\theta)$ is the ionised volume limited by θ. The number of neutral atoms that enter through the boundary of the H II region per unit time is $\dot{N}_{in}(\theta) = \pi r^2 n_H v_*$.

Equation 1.18 does not have a general analytic solution. However, for larger values of v_*, $\dot{N}_{in}$ grows linearly with v_*. Instead, $\dot{N}_{rec}$ actually decreases

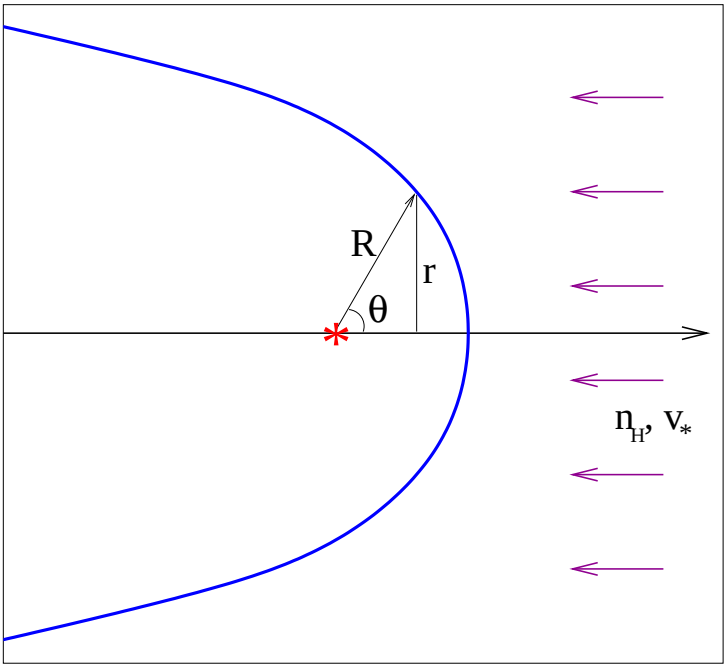

Figure 1.7: Schematic diagram showing a cometary H II region formed around a star which travels at a velocity v_* through a homogeneous ISM of density n_H.

with increasing values of v_*. Therefore for a high enough v_* we have $\dot{N}_{in} \gg \dot{N}_{rec}$, and equation 1.18 becomes

$$\frac{S_*}{4\pi}\Delta\Omega \approx \dot{N}_{in}(\theta)\,. \tag{1.20}$$

If we substitute the appropriate expressions for the solid angle and for the rate of neutrals entering the H II region, we then obtain the solution

$$r(\theta) = \sqrt{\frac{S_*}{2\pi n_H v_*}(1-\cos\theta)}\,. \tag{1.21}$$

For $\theta = 0$, this solution has an on-axis separation

$$R_0 = \lim_{\theta\to 0}\frac{r(\theta)}{\sin\theta} = \sqrt{\frac{S_*}{4\pi n_H v_*}}\,, \tag{1.22}$$

between the star and the "head" of the cometary H II region (see Fig. 1.7). For $\theta \to \pi$, the edge of the H II region reaches a maximum separation

$$r_m = \sqrt{\frac{S_*}{\pi n_H v_*}} \tag{1.23}$$

with respect to the symmetry axis.

One can show that the approximation of neglecting the recombinations within the H II region in the balance equation (Eqs. 1.18 and 1.20) is correct provided that the on-axis standoff distance R_0 (Eq. 1.22) satisfies the condition $R_0 \ll R_S$, where R_S is the "standard" Strömgren radius, defined by Eq. 1.8. Through some simple algebra, this condition can be rewritten as

$$v_* \gg v_S \equiv \left(\frac{\alpha_B}{3}\right)^{2/3}\left(\frac{n_H S_*}{4\pi}\right)^{1/3}\,. \tag{1.24}$$

For example, for an O5 star moving into a medium with $n_H = 1$ cm^{-3}, we have $v_S \approx 260$ km s^{-1} (where we have used the value for S_* from Table 1.1 and for α_B at 10^4 K from Eq. 1.13).

By differentiating with respect to θ (see [14]), the full balance equation (Eqs. 1.18-1.19) can be written as

$$\left(\frac{R}{R_S}\right)^3 + \xi\left(\frac{R}{R_S}\right)\left[\left(\frac{\dot{R}}{R_S}\right)\sin\theta + \left(\frac{R}{R_S}\right)\cos\theta\right] = 1\,, \tag{1.25}$$

where R_S is given by Eq. 1.8, $\dot{R} = dR/d\theta$ and $\xi \equiv v_*/v_S$ (see Eq. 1.24). One can show that for $\xi \gg 1$ one obtains the solution described above (Eq. 1.21). Also, this equation has an analytic solution for the $\xi \ll 1$ limit :

$$R(\theta) = R_S \left(1 - \xi \cos\theta\right)^{1/3} . \tag{1.26}$$

No general analytic solution to Eq. 1.26 has been found, so that in order to obtain the shape of the H II region for $\xi \sim 1$ it is necessary to carry out a numerical integration of the equation.

1.4.4 The initial expansion of an H II region

Let us now consider the problem of a homogeneous H II region in which the star "turns on" at $t = 0$, emitting a constant S_* ionising photon rate for $t > 0$. The outer radius R of the H II region is initially zero (actually, equal to R_* and not strictly 0), and grows monotonically with time until it reaches the value of the Strömgren radius R_S (see Eq. 1.8). If we neglect the light-crossing time in which the ionising photons travel from the star to the outer radius of the nebula, we can write the balance equation

$$S_* = \frac{4\pi}{3} R^3 {n_H}^2 \alpha_B + 4\pi R^2 F \,, \tag{1.27}$$

where R is the (time-dependent) outer radius of the H II region and F is the ionising photon flux (number of ionising photons per unit area and time) reaching the outer boundary of the nebula. Each of these photons ionises a new H atom, so that

$$F = n_H \frac{dR}{dt} \,. \tag{1.28}$$

Combining Eqs. 1.27-1.28, one obtains

$$\frac{dR}{dt} = \frac{S_*}{4\pi R^2 n_H} - \frac{n_H \alpha_B R}{3} \,, \tag{1.29}$$

which can be integrated to obtain

$$R(t) = R_S \left(1 - e^{-t/t_R}\right)^{1/3} , \tag{1.30}$$

with

$$t_R \equiv \frac{3}{n_H \alpha_B} ; \quad R_S \equiv \left(\frac{3S_*}{4\pi {n_H}^2 \alpha_B}\right)^{1/3} . \tag{1.31}$$

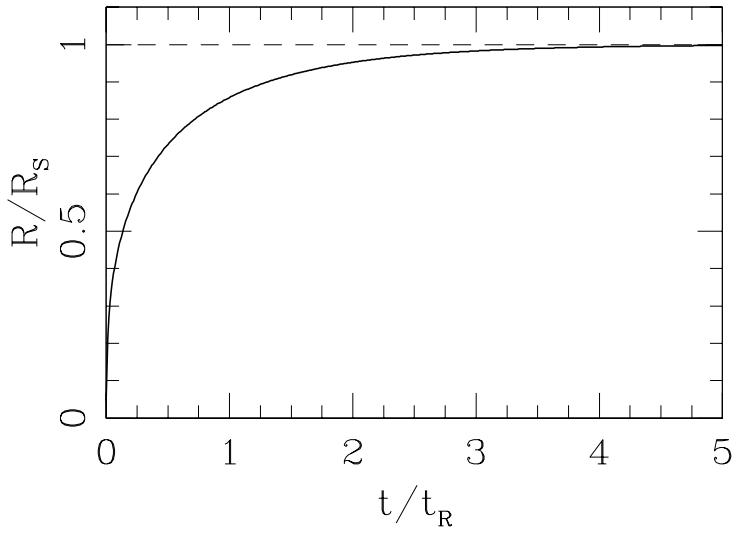

Figure 1.8: Solution for the time-dependent radius of an expanding, constant density H II region (see the text). It is clear that for $t > 3t_R$, the radius approaches R_S.

Using the value of $\alpha_B(10^4\text{K})$ (see Eq. 1.13) and $n_H = 1$ cm^{-3}, we obtain $t_R = 1.24 \times 10^5$ yr. The solution for the expansion of the H II region is shown in Fig. 1.8.

1.5 The structure of the ionisation front

The outer boundary of an H II region is called an "ionisation front" (with H in the form of H II inside the boundary, and H as H I outside). In the treatment above we have assumed that this transition region between H II and H I has a negligible thickness $\Delta R \ll R_S$. In this section we will present an approximate model describing this transition region, from which we can obtain an evaluation of the value of ΔR.

Let us first consider the ionisation equilibrium for H, which is dominated by the processes of photoionisation and radiative recombination :

$$n_{HI}\phi_H = n_e n_{HII}\alpha_H \,, \tag{1.32}$$

where ϕ_H is the photoionisation rate per neutral H atom :

$$\phi_H = \int_{\nu_H}^{\infty} \frac{4\pi J_\nu}{h\nu} \sigma_\nu \, d\nu \,, \tag{1.33}$$

with σ_ν the photoionisation cross section of H and

$$J_\nu = \frac{1}{4\pi} \oint I_\nu d\Omega \tag{1.34}$$

the zero-order moment of the specific intensity I_ν. If the ionising photons only come from the star (in other words, neglecting, e. g., the Lyman continuum photons emitted by the nebula), we have

$$4\pi J_\nu = \frac{L_\nu}{4\pi R^2} e^{-\tau_\nu} \,; \quad \tau_\nu = \int_0^R n_{HI} \sigma_\nu \, dR \,. \tag{1.35}$$

As we will see below, the photoionisation cross section of H has a frequency dependence $\sigma_\nu \propto \nu^{-3}$, which is very slow compared with the fast drop of the distribution $L_\nu/(h\nu)$ of the far-UV stellar photons. Therefore, the terms involving σ_ν can be taken out of the frequency integral in Eq. 1.33, so that we obtain

$$\phi_H = \int_{\nu_H}^{\infty} \frac{L_\nu}{4\pi R^2 h\nu} e^{-\tau_\nu} \sigma_\nu d\nu \approx \sigma_{\nu_H} F \,, \tag{1.36}$$

with

$$F \equiv \frac{S_*}{4\pi R^2} e^{-\tau_{\nu_H}} \,. \tag{1.37}$$

Now, provided that the thickness of the ionisation front is indeed small compared to R_S (this will be shown to be indeed the case with the model that we are developing), in Eq. 1.37 we can put $R = R_S$ (i. e., a constant geometrical dilution throughout the radial structure of the ionisation front). We then have

$$\frac{dF}{dl} = -F n_{HI} \sigma_{\nu_H} \,, \tag{1.38}$$

where $l = R - R_S$ is a radial coordinate measured with respect to the Strömgren radius.

We now introduce the ionisation fraction of H : $x = n_{HII}/n_H$. It is clear that $n_{HII} = x n_H$ and $n_{HI} = (1-x) n_H$. The ionisation equilibrium equation (Eq. 1.32) then takes the form

$$\frac{x^2}{1-x} = \frac{\phi_H}{n_H \alpha_H} = \frac{\sigma_{\nu_H}}{n_H \alpha_H} F \,, \tag{1.39}$$

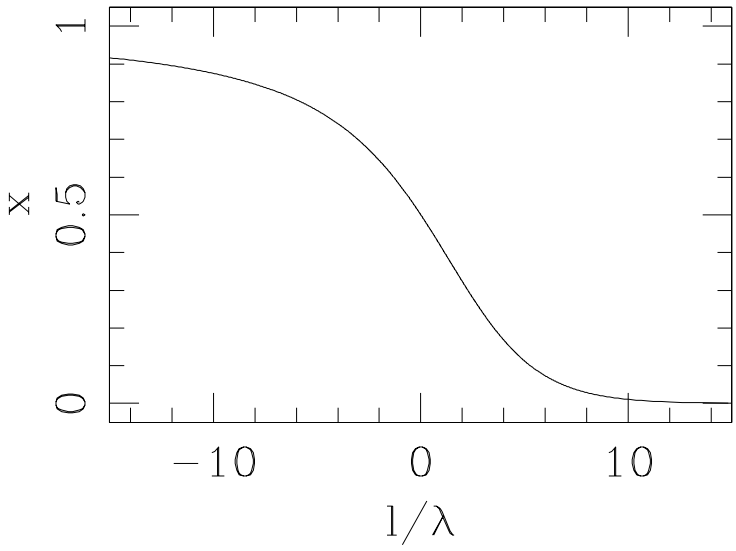

Figure 1.9: Solution for the structure of the ionisation fraction x as a function of the dimensionless distance l/λ from the Strömgren radius (see the text).

where for the second equality we have used Eq. 1.36. From Eq. 1.39 we can find F in terms of x, and differentiate with respect to $l = R - R_S$ to obtain

$$\frac{dF}{dl} = \frac{n_H \alpha_H}{\sigma_{\nu_H}} \frac{d}{dl}\left(\frac{x^2}{1-x}\right) = \frac{n_H \alpha_H}{\sigma_{\nu_H}} \frac{x(2-x)}{(1-x)^2} \frac{dx}{dl}\,. \tag{1.40}$$

We now combine equations 1.38 and 1.40 to obtain

$$\frac{dx}{dl} = -n_H \sigma_{\nu_H} \frac{x(1-x)^2}{2-x}\,, \tag{1.41}$$

which can be integrated to obtain

$$2\,\ln\left(\frac{x}{1-x}\right) + \frac{1}{1-x} = 2 - \frac{l}{\lambda}\,, \tag{1.42}$$

where $\lambda = (n_H \sigma_{\nu_H})^{-1}$ is the photon mean free path in a neutral medium of density n_H. In order to derive this equation we have used the boundary condition $x(l = 0) = 1/2$ (i. e., $x = 1/2$ at the Strömgren radius).

This solution is plotted in Fig. 1.9, from which we see that the thickness of the ionisation front is $\Delta R \approx 10\lambda$. Using the fact that $\sigma_{\nu_H} \approx 6.3 \times 10^{-18}$ cm^2, we obtain $\Delta R \approx 1.6 \times 10^{17}\mathrm{cm}\,(1\,\mathrm{cm}^{-3}/n_H)$, which can be compared with the Strömgren radii predicted for different O/B stars (see Table 1.1 and Eq. 1.8) to see that we indeed have $\Delta R \ll R_S$.

1.6 The ionisation of a nebula with many elements

1.6.1 The rate equations

For the sake of simplicity, in this section we consider the case of a constant density gas, for which the equations for an atomic/ionic network are :

$$\frac{dn_{a,z}}{dt} = {S^c}_{a,z} + {S^{ph}}_{a,z} \,, \tag{1.43}$$

with the collisional (S^c) and photoionisation (S^{ph}) source terms being given by

$${S^c}_{a,z} = n_e \left[n_{a,z-1} c_{a,z-1} + n_{a,z+1} \alpha_{a,z+1} - n_{a,z} \left(c_{a,z} + \alpha_{a,z} \right) \right] \,, \tag{1.44}$$

$${S^{ph}}_{a,z} = n_{a,z-1} \phi_{a,z-1} - n_{a,z} \phi_{a,z} \,. \tag{1.45}$$

If the $n_{a,z}$ are known, the electron density can be computed as

$$n_e = \sum_a \sum_z z \, n_{a,z} \,. \tag{1.46}$$

1.6.2 Ionisation equilibrium

The time-evolution of the ionisation rate equations leads to a final equilibrium for which $dn_{a,z}/dt = 0$ for all a and z. From Eq. 1.43 it can be shown that this condition results in the system of equations :

$$n_{a,z} \left(n_e c_{a,z} + \phi_{a,z} \right) = n_{a,z+1} n_e \alpha_{a,z+1} \,. \tag{1.47}$$

1.6.3 The collisional rate coefficients

The collisional ionisation (c) and radiative+dielectronic recombination (α) coefficients are functions of temperature T given by integrals of the form

$$\alpha(T), \; c(T) \; = \int_0^\infty f(v,T) \sigma_v \, v \, dv \,, \tag{1.48}$$

where $f(v,T)$ is the Maxwell-Boltzmann distribution for the electrons, and σ_v is the velocity-dependent collision cross section for the appropriate process.

It is common to give analytic fits to these coefficients in the "Arrhenius interpolation" form :

$$r(T) = b_1\, T^{b_2}\, e^{b_3/T}\,. \tag{1.49}$$

As an example of other formulae, Aldrovandi & Péquignot ([2], [3]) have used an interpolation

$$r(T) = b_1 \left(\frac{T}{10^4}\right)^{-b_2} + b_3 T^{-3/2} \exp\left(-b_4/T\right)\left[1 + b_5 \exp\left(-b_6/T\right)\right]\,, \tag{1.50}$$

for recombination coefficients.

Then, the b_1, b_2, ... coefficients are tabulated for all of the ionisation and recombination processes that have to be considered. An example of such a tabulation is given in Table 1.2.

Finally, we should note that for some atoms and ions, in the collision source term ${S^c}_{a,z}$ (see eq. 1.44) one also has to include "charge exchange" reactions with H. An example of important charge exchange reactions are the processes HII + OI $\rightarrow$ HI + OII and HI + OII $\rightarrow$ HII + OI (see Table 1.2). These processes have rates of the form $n_{HII} n_{OI} q(T)$ and $n_{HI} n_{OII} q'(T)$, respectively, with the rate coefficients $q(T)$ and $q'(T)$ also given by Arrhenius interpolations (see Table 1.2).

1.6.4 The photoionisation rates

The photoionisation rates are calculated as a function of the average intensity J_ν of the radiative field through the frequency integrals

$$\phi_{a,z} = \int_{\nu_{a,z}}^{\infty} \frac{4\pi J_\nu}{h\nu} \sigma_{a,z}(\nu)\, d\nu\,, \tag{1.51}$$

where ν is the frequency, $\nu_{a,z} = \chi_{a,z}/h$ is the frequency of the ionisation edge and $\sigma_{a,z}(\nu)$ is the photoionisation cross section. Here again, one can find tabulations of coefficients of power law interpolations for the $\sigma_{a,z}(\nu)$ (see, e. g., any of the versions of the book of Osterbrock 1989).

The problem of course is that one has to solve a system of radiative transfer equations of the form

$$\frac{dI_\nu}{dl} = j_\nu - \kappa_\nu I_\nu \tag{1.52}$$

Table 1.2: Ionisation, recombination and charge exchange coefficients

reaction	coefficients[a]
$e + HI \rightarrow 2e + HII$	1: 5.83×10^{-11}, 0.5, -157800
$e + HII \rightarrow HI$	1: 3.69×10^{-10}, -0.79, 0
$e + HeI \rightarrow 2e + HeII$	1: 2.707×10^{-11}, 0.5, -285400
$e + HeII \rightarrow HeI$	2: 4.3×10^{-13}, 0.672, 0.0019, 4.7×10^5, 0.3, 94000
$e + HeII \rightarrow 2e + HeIII$	1: 5.711×10^{-12}, 0.5, -631000
$e + HeIII \rightarrow HeII$	1: 2.21×10^{-9}, -0.79, 0
$e + CII \rightarrow 2e + CIII$	1: 3.93×10^{-11}, 0.5. -283000
$e + CIII \rightarrow CII$	2: 3.2×10^{-12}, 0.770, 0.038, 9.1×10^4, 2.0, 3.7×10^5
$e + CIII \rightarrow 2e + CIV$	1: 2.04×10^{-11}, 0.5, -555600
$e + CIV \rightarrow CIII$	2: 2.3×10^{-12}, 0.645, 7.03×10^{-3}, 1.5×10^5, 0.5, 2.3×10^5
$e + NI \rightarrow 2e + NII$	1: 6.18×10^{-11}, 0.5 -168200
$e + NII \rightarrow NI$	2: 1.5×10^{-12}, 0.693, 0.0031 2.9×10^5, 0.6, 1.7×10^5
$e + NII \rightarrow 2e + NIII$	1: 4.21×10^{-11}, 0.5, -343360
$e + NIII \rightarrow NII$	2: 4.4×10^{-12}, 0.675, 0.0075 2.6×10^5, 0.7, 4.5×10^5
$e + OI \rightarrow 2e + OII$	1: 1.054×10^{-10}, 0.5, -157800
$e + OII \rightarrow OI$	2: 2.0×10^{-12}, 0.646, 0.0014 1.7×10^5, 3.3, 5.8×10^4
$e + OII \rightarrow 2e + OIII$	1: 3.53×10^{-11}, 0.5, -407200
$e + OIII \rightarrow OII$	2: 3.1×10^{-13}, 0.678, 0.0014 1.7×10^5, 2.5, 1.3×10^5
$e + OIII \rightarrow 2e + OIV$	1: 1.656×10^{-11}, 0.5, -636900
$e + OIV \rightarrow OIII$	2: 5.1×10^{-12}, 0.666, 0.0028 1.8×10^5, 6.0, 91000
$e + SII \rightarrow 2e + SIII$	1: 7.12×10^{-11}, 0.5, -271440
$e + SIII \rightarrow SII$	2: 1.8×10^{-12}, 0.686, 0.0049 1.2×10^5, 2.5, 88000
$HI + NII \rightarrow HII + NI$	1: 1.1×10^{-12}, 0, 0
$HII + NI \rightarrow HI + NII$	1: 4.95×10^{-12}, 0. -10440
$HI + OII \rightarrow HII + OI$	1: 2.0×10^{-9}, 0, 0
$HII + OI \rightarrow HI + OII$	1: 1.778×10^{-9}, 0, -220

[a]The interpolation formulae are of the form "1:" Arrhenius, or "2:" Aldrovandi & Péquignot (1973), see equations (1.49) and (1.50)

for the specific intensity I_ν (j_ν and κ_ν being the emission and absorption coefficients, respectively). This is a system of equations, since one has to solve this for many propagation directions (l being the distance element along a given direction) and frequencies. Clearly, only rays passing through the position of the central star have to be considered if one does not consider the diffuse ionising photon field (i. e., the far UV radiation produced by the nebular gas itself).

After integrating these radiative transfer equations, one can then carry out the appropiate angular average

$$J_\nu = \frac{1}{4\pi} \oint I_\nu d\Omega \tag{1.53}$$

in order to obtain the average intensity of the radiative field.

1.6.5 Coronal ionisation equilibrium

If the collisional ionisation rates dominate over the photoionisation rates, Eq. 1.47 takes the form :

$$n_{a,z} c_{a,z} = n_{a,z+1} \alpha_{a,z+1} \,. \tag{1.54}$$

As can be seen, this system gives ionisation fractions $y_{a,z} = n_{a,z}/n_a$ (where $n_a = \sum_z n_{a,z}$) which are exclusively a function of T. This result holds if charge exchange reactions are included. The resulting ionisation fractions ${y^c}_{a,z}(T)$ are called the "coronal ionisation equilibrium" ionisation state.

Clearly, if we have an ionisation fraction $y_{a,z} > {y^c}_{a,z}(T)$, $y_{a,z}$ will evolve to a lower value with time, and the reverse is true for $y_{a,z} < {y^c}_{a,z}(T)$.

As an example, let us consider the coronal ionisation equilibrium for H. Eq. 1.54 then gives

$$n_{HI} c(T) = n_{HII} \alpha(T) \,. \tag{1.55}$$

We can combine this equation with $n_H = n_{HI} + n_{HII}$ to obtain

$$y_{HII} = \frac{n_{HII}}{n_H} = \frac{1}{1 + \alpha(T)/c(T)} \,, \tag{1.56}$$

where the Arrhenius interpolations for the coefficients are $\alpha(T) = 3.69 \times 10^{-10} T^{-0.79}$ and $c(T) = 5.83 \times 10^{-11} T^{0.5}\, e^{-157800/T}$ (see equation 1.49 and the first two lines of Table 1.2). The hydrogen ionisation fraction y_{HII} as a function of temperature T obtained from Eq. 1.56 is shown in Fig. 1.10.

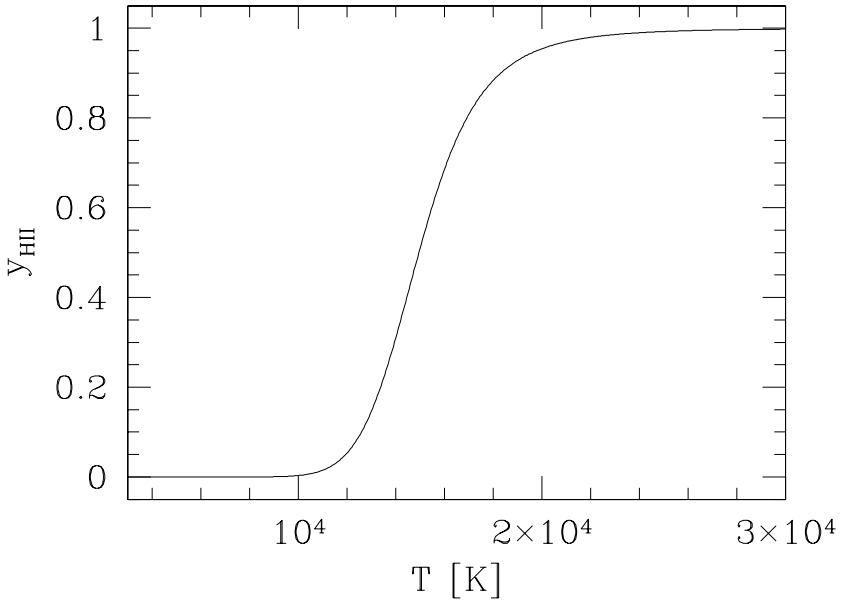

Figure 1.10: Coronal ionisation fraction of H as a function of temperature

1.6.6 Photoionisation equilibrium

If the photoionisation rates dominate over the collisional ionisation rates, Eq. 1.47 takes the form :

$$n_{a,z}\phi_{a,z} = n_e n_{a,z+1}\alpha_{a,z+1}\,. \tag{1.57}$$

This is the system of equations which describe the ionisation state of a stationary H II region. An example of a simplified solution for a pure H region is given in §1.5.

1.7 The energy balance and the heating rate

In order to obtain the thermal structure of a photoionized region it is necessary to integrate a differential equation of the form

$$\frac{3}{2}\frac{d}{dt}(n+n_e)kT = \Gamma - L\,, \tag{1.58}$$

where n is the atom+ion number density, n_e the electron density, k Boltzmann's constant, and Γ and L the energy gain and loss (respectively) per

unit volume and time of the gas. This equation is valid for a nebula in which the mass density is time-independent.

For a steady-state nebula, the time derivative in Eq. 1.58 is equal to zero, and the energy balance equation is simply

$$\Gamma = L\,. \tag{1.59}$$

In photoionized regions, the energy gain is due to the process of photoionization, which introduces "hot" electrons into the gas. The heating therefore is a sum of terms due to the photoionization of the different ions present in the gas, though in practice the dominant heating process is the photoionization of HI, with smaller contributions due to the photoionization of HeI and HeII.

The heating per unit time and volume due to the photoionization of ion a, z is given by $\Gamma_{a,z} = n_{a,z}\psi_{a,z}$, with

$$\psi_{a,z} = \int_{\nu_{a,z}}^{\infty} \frac{4\pi J_\nu}{h\nu} h\left(\nu - \nu_{a,z}\right) \sigma_{a,z}(\nu)\, d\nu\,. \tag{1.60}$$

The integrals in the heating rate terms generally are done numerically. For the case in which the frequency dependence of the incident spectrum is given by a Planck function in the Wien limit at a temperature T_*, the integral in Eq. 1.60 can be carried out analytically, if one also assumes that the $\sigma_{a,z}(\nu)$ is a slow enough function so that it can be taken out of the integral as $\sigma_{a,z}(\nu_{a,z})$. In this case, the integral can be done analytically, obtaining

$$\psi_{a,z} = \phi_{a,z} kT_* \left(\frac{{x_0}^2 + 4x_0 + 6}{{x_0}^2 + 2x_0 + 2}\right)\,, \tag{1.61}$$

where $\phi_{a,z}$ is the photoionization rate and $x_0 = h\nu_{a,z}/(kT_*)$.

1.8 The cooling function

1.8.1 Introduction

In this section, we describe in some detail how to include the more important contributions to the cooling due to different processes. Actually, the cooling is dominated by collisional excitation of emission lines. We describe the radiative recombination and free-free losses only because it is very simple to include them, though they do not make an important contribution to the cooling function (at least for a gas with solar abundances).

1.8.2 Recombination and free-free cooling

When an electron passes by an ion and recombines, the kinetic energy of the electron is lost from the thermal energy reservoir. Analogously, when an electron looses kinetic energy in an inelastic collision (with the resulting emission of a photon), the thermal energy of the gas is reduced.

The free-free energy loss (per unit time and volume) due to the interaction of H ions and free electrons is given by :

$$L_{ff}(HII) = n_e n_{HII} \beta_{ff}(T)\,, \tag{1.62}$$

where the interpolation formula

$$\beta_{ff}(z,T) = 1.846 \times 10^{-27} z^2 T^{1/2}\,, \tag{1.63}$$

can be used (see the book of Osterbrock). In this interpolation function, one has to set a charge $z = 1$ for HII. One can use the same function (i. e., with $z = 1$) for calculating the free-free losses due to He II ions (this of course being only an approximation because He I is not a hydrogenic ion) and the function with $z = 2$ for He III ions.

The radiative losses due to recombination of HII are given by :

$$L_{rec}(HII) = n_e n_{HII} \beta_{rec}(T)\,, \tag{1.64}$$

where the interpolation formula

$$\beta_{rec}(t) = 1.133 \times 10^{-24} t^{-1/2} \left(-0.0713 + 0.5 \ln t + 0.640 t^{-1/3}\right) \tag{1.65}$$

with $t = 157890/T$ (see Seaton 1959). The contribution of the recombination of He ions can be computed with the scaling

$$\beta_{rec}(z,T) = z \beta_{rec}(1, T/z^2)\,, \tag{1.66}$$

with $z = 1$ for HeII and $z = 2$ for HeIII.

1.8.3 Collisional ionisation

The energy loss due to collisional ionisation of the ion a, z can be written as

$$L^{ion}{}_{a,z} = n_e n_{a,z} c_{a,z}(T)\, \chi_{a,z}\,, \tag{1.67}$$

where $c_{a,z}(T)$ is the collisional ionisation coefficient and $\chi_{a,z}$ the ionisation potential of the ion a, z.

The terms that dominate the collisional ionisation cooling are the ionisation of HI, HeI and HeII. These terms dominate the cooling function for a neutral gas that is suddenly shocked to a temperature above a few times 10^4 K.

1.8.4 Collisionally excited lines

For each atom or ion that contributes substantially to the cooling function, one has to solve a system of equations giving the populations of the excited levels n_l ($l = 1, 2, ..., N$ numbering in order of increasing energy all of the relevant levels) of the ion a, z. Of course, we have the relation

$$n_{a,z} = \sum_{l=1}^{N} n_l \,. \tag{1.68}$$

Once we have computed the n_l populations, we can compute the energy loss due to the collisional excitation of all of the relevant levels of the ion a, z as

$$L_{a,z}^{col} = \sum_{l=2}^{N} n_l \sum_{m<l} A_{l,m} h\nu_{l,m} \,, \tag{1.69}$$

where $A_{l,m}$ is the Einstein A coefficient for the spontaneous transition $l \rightarrow m$ and $h\nu_{l,m}$ is the energy associated with this transition.

The non-trivial problem of finding the populations n_l of the excited levels of course still remains. Because the relaxation time for the excitation/de-excitation of the levels is generally much shorter than the cooling and/or dynamical timescales of the flow, the calculation of the n_l is usually done under a statistical equilibrium assumption. The equilibrium condition results in the set of equations :

$$\sum_{m>l} n_m A_{m,l} + n_e \sum_{m\neq l} n_m q_{m,l}(T) = n_l \left[\sum_{m<l} A_{l,m} + n_e \sum_{m\neq l} q_{l,m}(T) \right] \,, \tag{1.70}$$

where we have introduced the $q_{m,l}(T)$ which are the radiative excitation ($m < l$) or de-excitation ($m > l$) coefficients. For $m > l$, these coefficients are given by the expression

$$q_{m,l}(T) = \frac{8.629 \times 10^{-6}}{T^{1/2}} \frac{\Omega_{ml}(T)}{g_m} \,, \tag{1.71}$$

where g_m is the statistical weight of the level at which the transition begins. The collisional excitation coefficients (i. e., $l \rightarrow m$ with $m > l$) are given by the relation

$$q_{l,m}(T) = \frac{g_m}{g_l} e^{-h\nu_{m,l}/kT} q_{m,l}(T)\,. \tag{1.72}$$

The function $\Omega_{ml}(T)$ has a value of order 1, and is only slowly dependent on T. In many calculations, these "collision strengths" are considered to be constant, and taken from tabulations such as the classical one of Mendoza (1983). However, in our modern electronic world there is the database of the Arcetri/Cambridge/NRL "CHIANTI" atomic data base collaboration (http://www.arcetri.astro.it/science/chianti/database/) which has temperature-dependent interpolations of the collision strengths and the Einstein A coefficients of all of the transitions I have ever known.

We now proceed as follows. We assume that the A and q coefficients are known, as well as the temperature T (obtained, e. g., from a dynamical simulation) the electron density n_e and the ionic number density $n_{a,z}$ (both obtained from a solution of the non-equilibrium ionisation rate equations). We can then invert the system of linear Eqs. 1.68 and 1.70 in order to find the populations n_l ($l = 1 \rightarrow N$) of the excited levels of the ion a, z.

Let us show how the equations look for a 3-level atom ($N = 3$). Eq. 1.68 takes the form

$$n_1 + n_2 + n_3 = n_{a,z}\,. \tag{1.73}$$

Now, for $l = 1$, from Eq. 1.70 we obtain

$$n_1\left[-n_e(q_{12} + q_{13})\right] + n_2(A_{21} + n_e q_{21}) + n_3(A_{31} + n_e q_{31}) = 0\,, \tag{1.74}$$

and for $l = 2$, we obtain :

$$n_1(n_e q_{12}) + n_2\left[-A_{21} - n_e(q_{23} + q_{21})\right] + n_3(A_{32} + n_e q_{32}) = 0\,. \tag{1.75}$$

For $l = 3$, we obtain an equation that is a linear combination of Eqs. 1.74-1.75.

Now, the system of 3 linear equations 1.73-1.75 can be inverted in order to find n_1, n_2 and n_3 as a function of $n_{a,z}$, n_e and T.

1.8.5 The 2-level atom

Let us now consider a 2-level atom ($N = 2$). Eq. 1.68 takes the form

$$n_{a,z} = n_1 + n_2\,, \tag{1.76}$$

and Eq. 1.70 takes the form

$$n_1 n_e q_{12} = n_2(n_e q_{21} + A_{21})\,. \tag{1.77}$$

These two equations can be combined with Eq. 1.72 to obtain :

$$n_2 = \frac{n_{a,z}}{(g_1/g_2)e^{E_{21}/kT} + 1 + n_c/n_e}\,, \tag{1.78}$$

where the critical density is defined as $n_c \equiv A_{21}/q_{12}$. Then, for $n_e \ll n_c$ (the "low density regime"), we have

$$n_2 = \frac{n_{a,z} n_e q_{12}}{A_{21}}\,, \tag{1.79}$$

and for $n_e \gg n_c$ (the "high density regime"), we have

$$n_2 = \frac{n_{a,z} g_2 e^{-E_{21}/kT}}{g_1 + g_2 e^{-E_{21}/kT}}\,, \tag{1.80}$$

which is the Boltzmann distribution (LTE) population of level n_2.

The energy loss associated with the transition between levels 2 and 1 is :

$$L_{21} = n_2 A_{21} h\nu_{21}\,, \tag{1.81}$$

which for the low density regime then takes the form

$$L_{21} = n_{a,z} n_e q_{12} h\nu_{21}\,, \tag{1.82}$$

and for the high density regime becomes

$$L_{21} = n_2(LTE) A_{21} h\nu_{21}\,, \tag{1.83}$$

These equations illustrate the well known fact that the collisionally excited line cooling function depends quadratically on the density for the "low density regime" and linearly for the "high density regime".

1.9 The temperature of an HII region

In order to obtain an estimate of the temperature of a photoionised region, we consider the balance between the heating due to H photoionisation :

$$\Gamma \approx n_{HI} \phi_{HI} k T_*\,, \tag{1.84}$$

where T_* is the black-body temperature of the star (see equations 1.60-1.61), and the cooling due to the collisional excitation of a single line of OII :

$$L = n_e n_{OII} q_{12}(T) h\nu_{12} \,, \tag{1.85}$$

in the low density regime (see equation 1.82). This is of course an underestimate of the real cooling function, which has contributions from many collisionally excited lines.

We first use the H photoionisation equilibrium condition (see equation 1.32)

$$n_{HI}\phi_H = n_e n_{HII}\alpha_H(T) \tag{1.86}$$

and consider that inside the HII region we have $n_e \approx n_{HII} \approx n_H$ to obtain an estimate of the neutral H density :

$$n_{HI} \approx \frac{n_H^2 \alpha_H(T)}{\phi_H} \,. \tag{1.87}$$

Substituting this estimate of n_{HI} in the heating term (equation 1.84), we then obtain :

$$\Gamma \approx n_H^2 \alpha_H(T) k T_* \,, \tag{1.88}$$

where from Table 1.2 we have $\alpha_H(T) = 3.69 \times 10^{-10} T^{-0.79}$ (in c.g.s.).

For the cooling function, we assume that inside the HII region $n_{OII} \approx n_O \approx 10^{-4} n_H$, and that the transition has an energy $h\nu_{21} \sim 1$ eV (so that $h\nu_{12}/k \approx 10^4$ K). Using the temperature dependence of the collisional excitation coefficient (see equations 1.71-1.72) we then obtain

$$L \approx 10^{-4} n_H^2 \frac{8.6 \times 10^{-6} \Omega_{21}}{T^{1/2} g_1} e^{-10^4/T} \,, \tag{1.89}$$

where we can set $\Omega_{21} \sim g_1 \sim 1$.

Finally, using equations (1.88-1.89), the energy gain/loss balance condition (equation 1.59) $\Gamma = L$ gives :

$$T = \frac{10^4 \mathrm{K}}{0.29 \ln T - 0.542} \,, \tag{1.90}$$

for a $T_* = 4 \times 10^4$K stellar temperature.

Through a few iterations, it can be shown that the solution to this trascendental equation is $T \approx 5200$ K. More detailed solutions to the energy balance equation (including cooling through many lines, with the correct atomic parameters) typically give temperatures in the $5000 \rightarrow 10000$ K range.

Two interesting points should be noted:

- the temperature resulting from the energy balance is independent of the density of the gas. This result is preserved if one includes a more detailed cooling function, provided that the collisionally excited lines (which dominate the radiative cooling) are in the low density regime,

- very similar temperatures for the nebula are obtained no matter what is the value of the stellar temperature T_*. This is a result of the fact that the collisional excitation coefficients have a very strong temperature dependence at temperatures $T \sim h\nu_{ij}/k$, and that the fine structure lines of many ions have energies $\sim$ 1eV (corresponding to $\sim 10^4$ K). This high temperature dependence of the cooling function fixes the nebular temperature at $\sim 10^4$ K for a wide range of possible values for the energy gain term.

Chapter 2

The emitted spectrum

2.1 Emission lines

In the previous chapter, we have discussed how to calculate the populations of the excited levels of an atom or ion, with the objective of the calculation of the cooling due to collisionally excited lines. We now present the general statistical equilibrium equations for the populations of the excited levels of atoms/ions in the ISM :

$$\sum_{m>l} n_m A_{m,l} + n_e \sum_{m\neq l} n_m q_{m,l}(T) + n_e\, n_{a,z+1}\alpha_{z+1,l}(T) = n_l \left[\sum_{m<l} A_{l,m} + n_e \sum_{m\neq l} q_{l,m}(T)\right] , \tag{2.1}$$

which coincides with Eq. 1.70 with the exception of the second term on the left hand side of the equation, which represents the recombinations of the higher ionization state $a, z+1$ to the excited level l of the ion a, z. The radiative+dielectronic recombination coefficient for this process is $\alpha_{z+1,l}(T)$.

This system of equations giving the populations of the excited levels n_l ($l = 1, 2, ..., N$ numbering in order of increasing energy all of the relevant levels) of the ion a, z. These equations have to be supplemented with the relation

$$n_{a,z} = \sum_{l=1}^{N} n_l \, . \tag{2.2}$$

2.2 Recombination lines

In HII regions, the populations of the excited levels of HI, HeI and HeII are determined mostly by the processes of recombination (of HII, HeII and HeIII, respectively) to excited levels and spontaneous, radiative transitions to lower levels. These processes are represented by the first and third terms on the left and the first term on the right of Eq. 2.1. The lines of H and He in HII regions are therefore called "recombination lines".

The lines of H (resulting from transitions from energy level N to N') are named according to the end state (N') and to the jump in energy quantum number ($\Delta N = N - N'$). For $N' = 1, 2, 3, \ldots$ we have:

1. $N' = 1$: Lyman series lines,
2. $N' = 2$: Balmer series lines,
3. $N' = 3$: Paschen series lines,
4. $N' = 4$: Brackett series lines,
5. $N' = 5$: Pfund series lines,
6. $N' = 6$: Humphreys series lines.

For $\Delta N = 1, 2, 3, \ldots$, the lines are denominated α, β, γ, ..., respectively.

The Lyman series lines are denoted as Lyα ($2 \rightarrow 1$ transition), Lyβ ($3 \rightarrow 1$ transition), Lyγ, ... The Balmer series are denoted as Hα ($3 \rightarrow 2$ transition), Hβ ($4 \rightarrow 2$ transition), Hγ, ... (these are the stronger H lines observed at optical wavelengths). Prefixes "Pa", "Br" and "Pf" are used for the Paschen, Brackett and Pfund series lines, respectively.

2.2.1 The recombination cascade

Let us consider the excited levels of H. These levels are specified with two quantum numbers: N, L, with $N \geq 1$ (the energy quantum number) and $1 \leq L \leq N$ (the angular momentum quantum number). The spontaneous radiative transition rates are given by the Einstein coefficients $A_{NL,N'L'}$ which have non-zero values (for Hamiltonians in the dipole approximation) only for $L' = L \pm 1$.

The energies of the excited levels of H only depend on the energy quantum number N, and are given by

$$E_N = -\frac{\chi_H}{N^2}\,, \tag{2.3}$$

where $\chi_H = 13.6$ eV is the ionization potential from the ground state of H.

The system of equations of statistical equilibrium for the populations n_{NL} of the excited levels of HI (see eq. 2.1) then is:

$$n_e n_{HII} \alpha_{NL}(T) + \sum_{N'=N}^{\infty} \sum_{L'=L\pm1} n_{N'L'} A_{N'L',NL} = n_{NL} \sum_{N'=1}^{N-1} \sum_{L'=L\pm1} A_{NL,N'L'}\,. \tag{2.4}$$

If the $A_{NL,N'L'}$ and $\alpha_{NL}(T)$ coefficients are known, this system of equations can be inverted to find the level populations n_{NL}.

The most simple way of doing this inversion is as follows. One first defines the "branching ratio" :

$$P_{NL,N'L'} = \frac{A_{NL,N'L'}}{\sum_{N''=1}^{N-1} \sum_{L''=L\pm1} A_{NL,N''L''}}\,, \tag{2.5}$$

which gives the probability that a radiative transition out of level NL is a direct transition to $N'L'$. Clearly, $P_{NL,N'L'} \neq 0$ only if $L' = L \pm 1$.

We now calculate the "cascade matrix" $C_{NL,N'L'}$ as the probability that a transition down from NL reaches $N'L'$ either through a direct transition or via one or more transitions through intermediate levels. For $N' = N - 1$ it is clear that we have:

$$C_{NL,N-1\,L'} = P_{NL,N-1\,L'}\,. \tag{2.6}$$

For $N' = N - 2$:

$$C_{NL,N-2\,L'} = P_{NL,N-2\,L'} + \sum_{L''=L'\pm1} C_{NL,N-1\,L''} P_{N-1\,L'',N-2\,L'}\,. \tag{2.7}$$

If we now define

$$C_{NL,NL'} = \delta_{LL'}\,, \tag{2.8}$$

we can write the general expression (for arbitrary $N' < N$) as:

$$C_{NL,N'L'} = \sum_{N''=N'+1}^{N} \sum_{L''=L'\pm1} C_{NL,N''L''} P_{N''L'',N'L'}\,. \tag{2.9}$$

Once the cascade matrix has been computed, the solutions to the equilibrium equations (2.4) can be obtained from the relation

$$n_e n_{HII} \sum_{N'=N}^{\infty} \sum_{L'=0}^{N'-1} \alpha_{N'L'}(T)\, C_{N'L',NL} = n_{NL} \sum_{N''=1}^{N-1} \sum_{L''=L\pm1} A_{NL,N''L''}\,. \quad (2.10)$$

This system of equations give the level populations n_{NL} as a function of n_e, n_{HII} and the temperature T. Once the level populations have been computed, we can compute the emission coefficients for the $N \rightarrow N'$ transitions as :

$$j_{NN'} = \frac{h\nu_{NN'}}{4\pi} \sum_{L=0}^{N-1} \sum_{L'=L\pm1} n_{NL} A_{NL,N'L'} \equiv n_e n_{HII} \alpha^{eff}_{NN'}(T) \frac{h\nu_{NN'}}{4\pi}\,. \quad (2.11)$$

The second equality is the definition of the "effective recombination coefficient" (for the $N \rightarrow N'$ transition).

The recombination cascade is usually calculated under two possible assumptions :

- **case A:** that all of the lines are optically thin,
- **case B:** that the Lyman lines (i. e., the transitions to the 1s level) are optically thick.

The recombination cascade as derived in this section corresponds to "case A". For "case B", the same equations apply if one sets to zero the Einstein A coefficients for all Lyman lines (i. e., $A_{NL,1s} = 0$). It is also possible (in the context of a numerical model) to solve the radiative transfer in the Lyman lines, obtaining a gradual transition between cases A and B as the successive Lyman lines become optically thick.

2.2.2 Including collisions

For higher values of the energy quantum number N, collisions between protons and HI atoms producing transitions with $\Delta L = 1$ and $\Delta N = 0$ become progressively more important. Also, for temperature > 12000 K, collisions with electrons become important for producing transitions with $\Delta N \neq 0$.

Including these processes, the statistical equilibrium condition for level NL becomes:

$$n_e n_{HII} \alpha_{NL}(T) + \sum_{N'=N}^{\infty} \sum_{L'=L\pm1} n_{N'L'} A_{N'L',NL} +$$

$$\sum_{L'=L\pm1} n_{HII} n_{NL'} q_{NL',NL}(T) + \sum_{N'\neq N} \sum_{L'=L\pm1} n_e n_{N'L'} q_{N'L',NL}(T) =$$

$$n_{NL} \left[\sum_{N'=1}^{N-1} \sum_{L'=L\pm1} A_{NL,N'L'} + \sum_{L'=L\pm1} n_{HII} q_{NL,NL'}(T) + \sum_{N'\neq N} \sum_{L'=L\pm1} n_e q_{NL,N'L'}(T) \right] . \tag{2.12}$$

The collisional rates can be calculated as a function of the collision strengths as:

$$q_{NL,N'L'}(T) = \frac{8.629 \times 10^{-6}}{T^{1/2}} \frac{\Omega_{NL,N'L'}(T)}{2(2L+1)} , \tag{2.13}$$

which can be obtained from eq. (1.71) by setting $g_{NL} = 2(2L+1)$.

The Einstein A coefficients, and interpolations for the recombination coefficients and the collision strengths for the $N = 1 \rightarrow 5$ levels of H are given in tables 2.1-2.5. The recombination coefficient fits were carried out with the data in the rrc98##_h1.dat file of the Open-ADAS database. The electron collision strengths are fits to data in the copha#h_hal96h.dat and hlike_aek89h.dat files of this database. The proton collision strengths are fits to the results of Seaton (1955) for the 2s-2p transition and Pengelly & Seaton (1964) and Brocklehurst (1971) for all of the other transitions.

Actually, though He II/H I collisions are not important for the angular momentum redistribution in H I, the He III/H I collisions are indeed important. Therefore, if He III has a substantial ionisation fraction, it is necessary to include terms $\propto n_{HeIII} n_{nL}$ in eq. (2.12). The rate coefficient can be calculated from eq. (2.13) using a value for the collision strength of $\Omega_{HeIII} = Z^2 \sqrt{C_{He}} \Omega_{HII}(T/Z^2 C_{He})$ where Ω_{HII} is the strength of the proton/HI collisions (see Table 2.5), $Z = 2$ is the charge of the He III ion, and

$$C_{He} \equiv \frac{\mu_{(He-p)}}{\mu_{(p-p)}} = \frac{8}{5} , \tag{2.14}$$

where $\mu_{(He-p)}$ is the reduced mass of the He/H system, and $\mu_{(p-p)}$ is the reduced mass of the H/H system.

Table 2.1: Energies and α's for the $N = 1 \rightarrow 5$ levels of H

level	E_N [cm^{-1}]	$\log_{10}(\alpha) = b_0 + b_1 t + b_2 t^2 + b_3 t^3\,;\ \ t = \log_{10}(T)$
1 : 1s	0	-9.9506 -1.2751 0.2385 -0.0244
2 : 2s	82259	-10.938 -1.1858 0.2235 -0.0238
3 : 2p	82259	-12.712 0.3821 -0.1176 -0.0032
4 : 3s	97492	-11.622 -1.0353 0.1896 -0.0215
5 : 3p	97492	-13.256 0.4629 -0.1347 -0.0020
6 : 3d	97492	-14.931 1.8421 -0.4766 0.0223
7 : 4s	102824	-12.087 -0.9310 0.1639 -0.0197
8 : 4p	102824	-13.651 0.5184 -0.1481 -0.0011
9 : 4d	102824	-15.173 1.8650 -0.4814 0.0226
10 : 4f	102824	-15.659 2.3114 -0.6300 0.0348
11 : 5s	105292	-12.442 -0.8533 0.1442 -0.0183
12 : 5p	105292	-13.939 0.5469 -0.1560 -0.0005
13 : 5d	105292	-15.398 1.8720 -0.4835 0.0227
14 : 5f	105292	-15.724 2.3138 -0.6301 0.0348
15 : 5g	105292	-15.455 2.1117 -0.6324 0.0369

2.3 Collisionally excited lines

2.3.1 General formalism

The lines of most of the atoms or ions observed in the ISM (except for the lines of H and He) are populated by collisional excitations up from the ground electronic state. This is because multi-electron atoms/ions do not have the large energy gap between the ground state and the first excited state characteristic of HI and HeI/II. Because of this, collisions with free electrons in a $\sim 10^4$ K (~ 1 eV) gas can easily excite the first few levels in these atoms/ions. The contribution from the recombination cascade then becomes only a small perturbation on the level populations, which are mainly determined only by (upwards and downwards) collisional transitions and by (downwards) radiative transitions. The transitions among the low lying levels of multi-electron atoms/ions are normally "magnetic dipole" or "electric quadrupole" transitions (having non-zero A coefficients only when higher order perturbation Hamiltonians are considered), and are usually called "forbidden lines" (and are denoted as, e. g., [O II] lines, in between square brackets). Some of the collisionally excited lines in multi-electron atoms/ions (particularly, the UV

Table 2.2: A_{ij} and Ω_{ij} for the $N = 1 \rightarrow 5$ levels of H

transition[a,b]		A_{ij} [s^{-1}]	$\Omega_{ij}(T) = b_0 + b_1 T + b_2 T^2$
2s→1s[a]	2 1	8.23	0.230701989 1.98505873E-06 -1.17145274E-11
2p→1s[a]	3 1	627000000.	0.370130298 9.41438027E-06 1.51916572E-11
3s→1s[a]	4 1	...	0.0555455253 1.09205141E-06 -7.22330208E-12
3p→1s[a]	5 1	167000000.	0.098599152 2.85713646E-06 -9.07527461E-12
3d→1s[a]	6 1	...	0.0471315582 1.49942413E-06 -6.83592715E-12
4s→1s[a]	7 1	...	0.0235801449 9.82577622E-07 -6.29846528E-12
4p→1s[a]	8 1	68200000.	0.0459912361 1.91578268E-06 -6.68320426E-12
4d→1s[a]	9 1	...	0.0247052783 4.82612921E-07 -1.93361593E-12
4f→1s[a]	10 1	...	0.0090413543 2.0730546E-08 -2.3834257E-13
5s→1s[a]	11 1	...	0.0118558411 5.12325143E-07 -3.26312452E-12
5p→1s[a]	12 1	34400000.	0.023435627 9.81865036E-07 -3.5210708E-12
5d→1s[a]	13 1	...	0.0127150878 2.43235821E-07 -9.73250094E-13
5f→1s[a]	14 1	...	0.00470449272 1.10018321E-08 -1.29156399E-13
5g→1s[a]	15 1	...	0.00062369044 -7.61068457E-09 3.66057556E-14
2p→2s[b]	3 2	...	378.724659 -0.000613531164 1.75879255E-09
3s→2s[a]	4 2	...	1.17686218 3.96001554E-05 -7.52731563E-11
3p→2s[a]	5 2	22500000.	1.81152248 9.2099616E-05 1.5241836E-10
3d→2s[a]	6 2	...	1.10043841 0.000191744768 -5.29052966E-10
4s→2s[a]	7 2	...	0.341652766 1.58109749E-05 -4.06526299E-11
4p→2s[a]	8 2	9670000.	0.647024189 5.23380315E-05 -1.70490774E-10
4d→2s[a]	9 2	...	0.552293565 5.52457995E-05 -2.56306745E-10
4f→2s[a]	10 2	...	0.399588795 4.43059453E-05 -2.09877084E-10
5s→2s[a]	11 2	...	0.520122966 8.2949122E-06 -3.48249174E-11
5p→2s[a]	12 2	4950000.	0.867017494 4.03942982E-05 -2.03482662E-10
5d→2s[a]	13 2	...	0.7094405 3.14156261E-05 -2.0075731E-10
5f→2s[a]	14 2	...	0.585537946 2.42882913E-05 -1.42870771E-10
5g→2s[a]	15 2	...	0.235978314 3.61284928E-06 -2.77494818E-11
3s→2p[a]	4 3	6310000.	1.94752427 1.92358023E-05 -7.79667781E-11
3p→2p[a]	5 3	...	6.51940845 0.000167401531 -6.12473933E-10
3d→2p[a]	6 3	64700000.	9.38290597 0.000714844201 5.37590056E-11
4s→2p[a]	7 3	2580000.	0.681844753 1.63355835E-05 -1.05496624E-10
4p→2p[a]	8 3	...	1.99947241 9.24779953E-05 -4.1253316E-10
4d→2p[a]	9 3	20600000.	2.58156827 0.000352482476 -1.28581419E-09
4f→2p[a]	10 3	...	2.39511694 0.000125033557 -5.78553883E-10
5s→2p[a]	11 3	1290000.	0.776657809 1.74219443E-05 -1.32396161E-10

[a]coll. strengths from the copha#h_hal96h.dat file, data produced by H. Anderson

[b]coll. strengths from the hlike_aek89h.dat file, with apparently as yet unpublished calculations by Berrington et al. (1988)

Table 2.3: A_{ij} and Ω_{ij} for the $N = 1 \rightarrow 5$ levels of H, continued

transition		A_{ij} [s^{-1}]	$\Omega_{ij}(T) = b_0 + b_1 T + b_2 T^2$
5p→2p[a]	12 3	...	2.43249038 6.02215821E-05 -3.78765622E-10
5d→2p[a]	13 3	9430000.	3.62224098 0.000196222456 -9.9819329E-10
5f→2p[a]	14 3	...	3.26614961 6.91791533E-05 -4.25243164E-10
5g→2p[a]	15 3	...	0.99771057 3.75655605E-06 -4.17823612E-11
3p→3s[b]	5 4	...	1450.93085 -0.00325160827 1.40768513E-08
3d→3s[b]	6 4	...	159.126917 -0.000840487719 3.48162807E-09
4s→3s[a]	7 4	...	1.08111582 0.000380437576 -1.15295628E-09
4p→3s[a]	8 4	3070000.	2.54886314 0.00040309013 5.56322488E-10
4d→3s[a]	9 4	...	3.14373004 0.000745642053 -2.42690635E-09
4f→3s[a]	10 4	...	3.7462125 0.000781879325 -3.57428797E-09
5s→3s[a]	11 4	...	1.54637257 0.000149080149 -6.63657887E-10
5p→3s[a]	12 4	1640000.	4.08813628 0.000169921842 -5.02562755E-10
5d→3s[a]	13 4	...	5.01383832 0.000247476134 -1.33289923E-09
5f→3s[a]	14 4	...	4.10691834 0.000127133679 -8.58848203E-10
5g→3s[a]	15 4	...	4.88714716 0.000244329779 -1.47617099E-09
3d→3p[b]	6 5	...	2146.0592 -0.00593632728 2.11624071E-08
4s→3p[a]	7 5	1840000.	3.40339559 0.000203061141 -6.75501874E-10
4p→3p[a]	8 5	...	8.60902539 0.00151186995 -4.7539148E-09
4d→3p[a]	9 5	7040000.	8.27640654 0.0025566506 -1.11232159E-09
4f→3p[a]	10 5	...	11.9669457 0.00323828319 -1.23422432E-08
5s→3p[a]	11 5	905000.	3.74173931 8.69809273E-05 -5.06385819E-10
5p→3p[a]	12 5	...	13.2467032 0.000539548421 -2.6260229E-09
5d→3p[a]	13 5	3390000.	15.2917815 0.00109804005 -4.70346691E-09
5f→3p[a]	14 5	...	16.2298902 0.000576218201 -3.63526886E-09
5g→3p[a]	15 5	...	18.1883828 0.000832453286 -4.85370914E-09
4s→3d[a]	7 6	...	4.21900483 4.84256639E-05 -2.15917333E-10
4p→3d[a]	8 6	348000.	13.4777083 0.000441890063 -2.29071345E-09
4d→3d[a]	9 6	...	24.9062683 0.00272229022 -1.01404508E-08
4f→3d[a]	10 6	13800000.	9.82447156 0.0119510675 -3.02823382E-08
5s→3d[a]	11 6	...	3.97162814 3.51386987E-05 -3.27759745E-10
5p→3d[a]	12 6	150000.	16.1334958 0.000110362663 -9.71870659E-10
5d→3d[a]	13 6	...	28.3632617 0.000957519873 -5.33191712E-09
5f→3d[a]	14 6	4540000.	49.7607587 0.00325075814 -1.53230468E-08
5g→3d[a]	15 6	...	38.330885 0.0015114171 -7.86878077E-09
4p→4s[b]	8 7	...	2964.29958 -0.00909288594 4.12297852E-08
4d→4s[b]	9 7	...	619.32623 -0.00430283349 2.8734997E-08

Table 2.4: A_{ij} and Ω_{ij} for the $N = 1 \rightarrow 5$ levels of H, continued

transition		A_{ij} [s^{-1}]	$\Omega_{ij}(T) = b_0 + b_1 T + b_2 T^2$
4f→4s[b]	10 7	...	124.174361 -0.00123347544 8.48440058E-09
5s→4s[a]	11 7	...	1.53806207 0.00173503526 -6.68625477E-09
5p→4s[a]	12 7	737000.	6.98282747 0.00152554702 -4.1843167E-09
5d→4s[a]	13 7	...	8.73782844 0.00225377148 -8.18431429E-09
5f→4s[a]	14 7	...	25.3224504 0.00222572566 -1.23041554E-08
5g→4s[a]	15 7	...	32.4265974 0.00129765509 -8.23655146E-09
4d→4p[b]	9 8	...	5549.92453 -0.0223901556 1.16294866E-07
4f→4p[b]	10 8	...	813.908792 -0.00744222541 4.90894342E-08
5s→4p[a]	11 8	645000.	13.3059416 0.00114087942 -6.17355099E-09
5p→4p[a]	12 8	...	22.7873231 0.00728109837 -2.4723519E-08
5d→4p[a]	13 8	1490000.	18.8738115 0.00699294439 -1.36005205E-08
5f→4p[a]	14 8	...	62.7008007 0.00875749509 -4.05388707E-08
5g→4p[a]	15 8	...	106.846064 0.00572769064 -3.40406121E-08
4f→4d[b]	10 9	...	6073.98362 -0.0339745489 1.90841831E-07
5s→4d[a]	11 9	...	15.6264397 0.000478850892 -2.67628835E-09
5p→4d[a]	12 9	188000.	53.7360076 0.00270059254 -1.56288932E-08
5d→4d[a]	13 9	...	84.0809099 0.0136172636 -5.41143791E-08
5f→4d[a]	14 9	2580000.	19.6994986 0.0223537455 -5.43237367E-08
5g→4d[a]	15 9	...	203.182691 0.0186641991 -9.35579156E-08
5s→4f[a]	11 10	...	12.3197499 2.74000635E-05 -3.51956415E-10
5p→4f[a]	12 10	...	47.7768773 0.000422602729 -3.52908665E-09
5d→4f[a]	13 10	50500.	105.135303 0.00307257987 -2.04380745E-08
5g→4f[a]	14 10	...	214.905676 0.018876845 -8.97469485E-08
5g→4f[a]	15 10	4250000.	144.086649 0.0760463582 -2.17769691E-07
5p→5s[b]	12 11	...	3924.60946 -0.00580398959 1.26210156E-08
5d→5s[b]	13 11	...	1442.42044 -0.00109774214 -3.32855828E-09
5f→5s[b]	14 11	...	447.109793 -0.00126487521 7.13987753E-09
5g→5s[b]	15 11	...	177.821648 -0.00169342267 1.00377598E-08
5d→5p[b]	13 12	...	8334.24411 -0.0118233038 2.21988618E-08
5f→5p[b]	14 12	...	2535.51791 -0.00757608021 3.9359465E-08
5g→5p[b]	15 12	...	652.74903 -0.00368088927 1.87021691E-08
5f→5d[b]	14 13	...	11531.0448 -0.023057997 8.77424046E-08
5g→5d[b]	15 13	...	2608.36252 -0.0157262948 8.37538465E-08
5g→5f[b]	15 14	...	12351.5748 -0.0429626285 1.81619962E-07

Table 2.5: Ω_{ij} for the proton collision, $\Delta N = 0$, $\Delta l = \pm 1$ transitions of H

transition		$\Omega_{ij}(T) = b_0 + b_1 \log_{10}(T)$
2p→2s	3 2	-29010.0 9999.0
3p→3s	5 4	-19765.4 20134.4
3d→3s	6 4	-66225.3 45302.3
4p→4s	8 7	-41439.6 67114.5
4d→4p	9 8	-294061.2 193289.8
4f→4d	10 9	80263.0 201343.6
5p→5s	12 11	-145593.4 167786.3
5d→5p	13 12	-650479.8 528526.8
5f→5d	14 13	-18963.3 719084.1
5g→5f	15 14	-247476.4 587252.1

lines) are "permitted" lines (i. e., "electric dipole" transitions).

For these atoms/ions, the statistical equilibrium equation (2.1) reduces to the more simple form given in the previous chapter (see eq. 1.70), which we repeat here:

$$\sum_{m>l} n_m A_{m,l} + n_e \sum_{m\neq l} n_m q_{m,l}(T) = n_l \left[\sum_{m<l} A_{l,m} + n_e \sum_{m\neq l} q_{l,m}(T) \right] , \quad (2.15)$$

where $q_{m,l}(T)$ are the radiative excitation ($m < l$) or de-excitation ($m > l$) coefficients. For $m > l$, these coefficients are given by the expression

$$q_{m,l}(T) = \frac{8.629 \times 10^{-6}}{T^{1/2}} \frac{\Omega_{ml}(T)}{g_m} , \quad (2.16)$$

where g_m is the statistical weight of the level at which the transition begins. The collisional excitation coefficients (i. e., $l \rightarrow m$ with $m > l$) are given by the relation

$$q_{l,m}(T) = \frac{g_m}{g_l} e^{-h\nu_{m,l}/kT} q_{m,l}(T) . \quad (2.17)$$

In eq. (2.15), the indeces m and l refer to a numbering system in which increasing values correspond to higher energy levels. The low lying levels in multi-electron atoms or ions generally correspond to the ground state configuration of the energy quantum number. Therefore, the energy quantum number is not given, and the levels are denoted by their angular momentum configuration in the form

$$^{2s+1}L_j \quad (2.18)$$

where s is the spin, L the orbital angular momentum (denoted S, P, D, ... for $L = 1, 2, 3, \ldots$, respectively) and j the total angular momentum quantum numbers. Two things should be noted:

- the statistical weight of the level is $g = 2j + 1$,
- the levels with the same s and L but different j form groups of $2s + 1$ levels with closely lying energies. These are called "singlet", "doublet" or "triplet" levels for $2s + 1 = 1$, 2 and 3, respectively.

Examples of the possible energy configurations are given in the "Grotrian diagrams" shown in Figures 2.1-2.5. A good source for obtaining the A coefficients and the collision strengths Ω is the material in Anil Pradhan's homepage (in particular, the table found in : http://www.astronomy.ohio-state.edu/ pradhan/table2.ps).

In using the parameters from such tabulations, one has to sometimes divide collision strengths given for a term with several levels into collision strengths for the inividual levels. For example, if a collision strength $\omega(SLJ, S'L')$ is tabulated (for a transition originating in level SLJ and ending in a multiplet $S'L'$), the collision strengths for the transitions between levels SLJ and the indiviual levels $S'L'J'$ of the $S'L'$ multiplet are given by :

$$\Omega(SLJ, S'L'J') = \frac{2J' + 1}{(2S' + 1)(2L' + 1)} \Omega(SLJ, S'L') \,, \tag{2.19}$$

where $2J'+1$ is the statistical weight of the $S'L'J'$ level and $(2S'+1)(2L'+1)$ is the statistical weight of the $S'L'$ term.

2.3.2 The 3-level atom

For an atom/ion with three levels, the equilibrium equations are :

$$n_3 \left[A_{31} + A_{32} + n_e(q_{31} + q_{32})\right] = n_e(n_1 q_{13} + n_2 q_{23}) \,, \tag{2.20}$$

$$n_2 \left[A_{21} + n_e(q_{21} + q_{23})\right] = n_3 A_{32} + n_e(n_1 q_{12} + n_2 q_{32}) \,, \tag{2.21}$$

$$n_e n_1 (q_{12} + q_{13}) = n_3 A_{31} + n_2 A_{21} + n_e(n_2 q_{21} + n_3 q_{31}) \,. \tag{2.22}$$

Actually, only two out of these three equations are linearly independent, so that one has to choose two of them, and solve them together with the conservation equation :

$$n_1 + n_2 + n_3 = n \,, \tag{2.23}$$

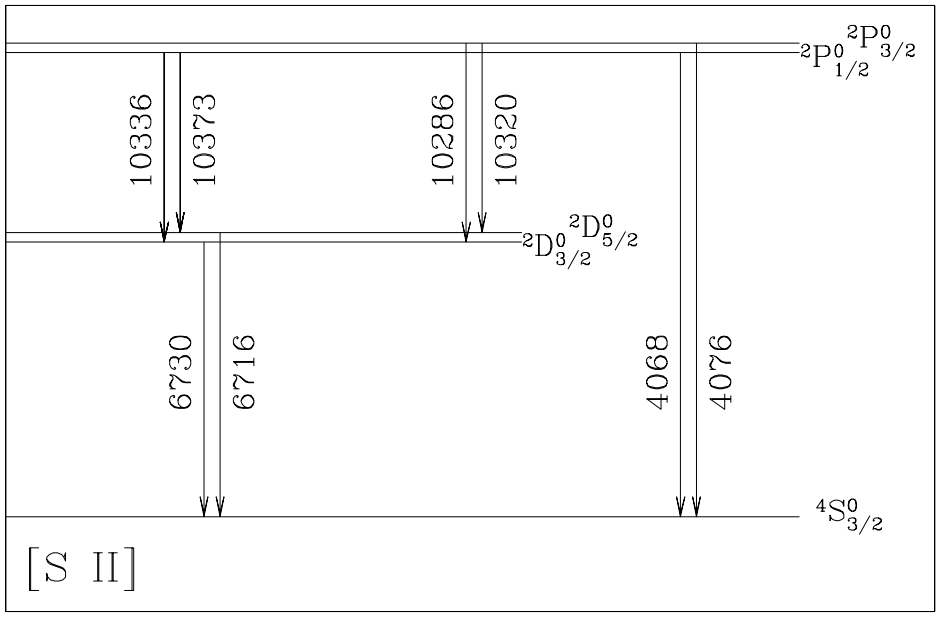

Figure 2.1: Energy level diagram showing the optical and IR forbidden transitions of S II. The wavelengths of the transitions are given in Å. For historical reasons, the $^2D - ^4S$ transitions are called the "nebular", the $^2P - ^4S$ the "auroral" and the $^2P - ^2D$ the "transauroral" lines.

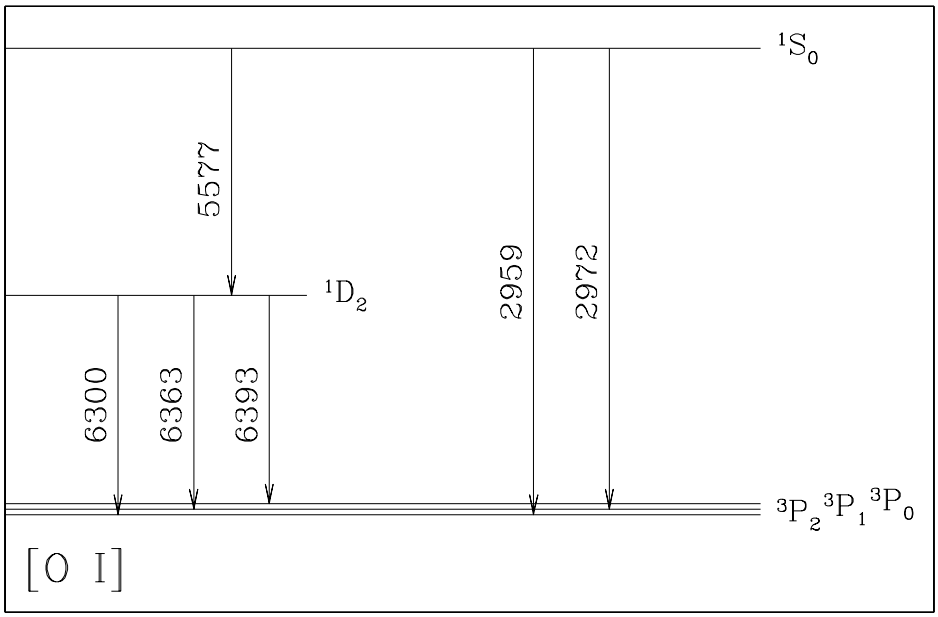

Figure 2.2: Energy level diagram showing the UV, optical and IR forbidden transitions of O I. The wavelengths of the transitions are given in Å.

where n is the total number density of the atom/ion that is being considered. The resulting system of 3 equations (with n_1, n_2 and n_3 as unknowns, and n_e, n and T as given parameters) can be solved.

Let us consider the case in which $A_{32} = 0$ and also $q_{23} = q_{32} = 0$. Equations (2.20-2.21) then take the form :

$$n_3(A_{31} + n_e q_{31}) = n_e n_1 q_{13}\,, \tag{2.24}$$

$$n_2(A_{21} + n_e q_{21}) = n_e n_1 q_{12}\,. \tag{2.25}$$

Dividing these two equations, we have

$$\frac{n_3}{n_2} = \left[\frac{A_{21} g_2 T^{1/2}/(n_e C\Omega_{12}) + 1}{A_{31} g_3 T^{1/2}/(n_e C\Omega_{13}) + 1}\right] \frac{g_3}{g_2} e^{-E_{23}/kT}\,, \tag{2.26}$$

where we have also used eq. (2.16) and the fact that $E_{13} = E_{12} + E_{23}$. In this equation, $C = 8.629 \times 10^{-6}$ (in c.g.s.).

We now consider the emission from an optically thin, homogeneous slab. The ratio of the intensities of the lines corresponding to the transitions $3 \rightarrow 1$

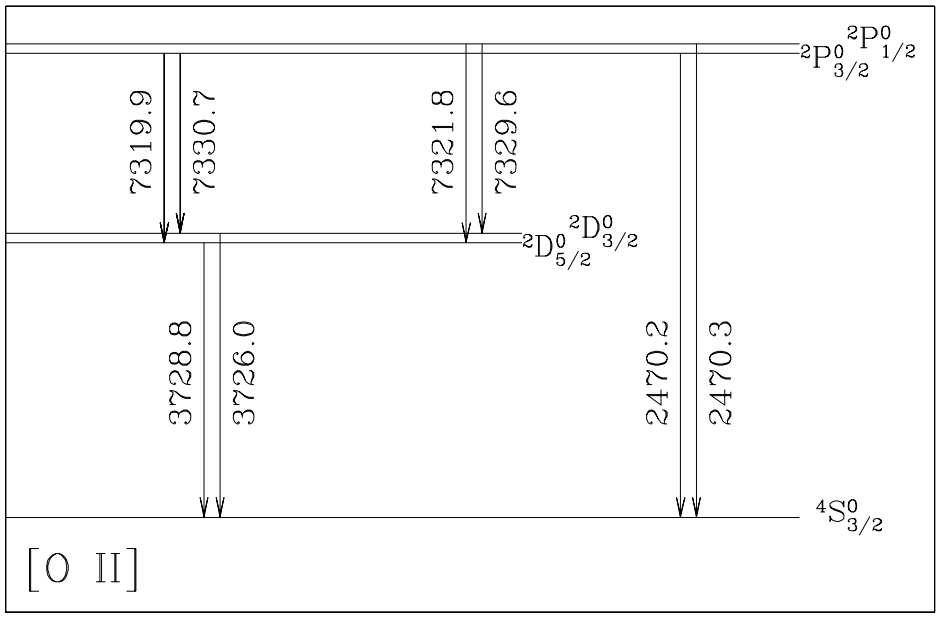

Figure 2.3: Energy level diagram showing the UV, optical and IR forbidden transitions of O II. The wavelengths of the transitions are given in Å.

and $2 \rightarrow 1$ is then given by :

$$\frac{I_3}{I_2} = \frac{n_3 A_{31} E_{31}}{n_2 A_{21} E_{21}} = \left[\frac{A_{21} g_2 T^{1/2}/(n_e C \Omega_{12}) + 1}{A_{31} g_3 T^{1/2}/(n_e C \Omega_{13}) + 1} \right] \frac{g_3}{g_2} e^{-E_{23}/kT} \frac{A_{31} E_{31}}{A_{21} E_{21}} , \quad (2.27)$$

where for the second equality we have used eq. (2.26).

In the low electron density regime, this ratio takes the form :

$$\frac{I_3}{I_2} = \frac{\Omega_{13}}{\Omega_{12}} e^{-E_{23}/kT} \frac{E_{31}}{E_{21}} , \quad (2.28)$$

In the high electron regime, the line ratio takes the form :

$$\frac{I_3}{I_2} = \frac{g_3}{g_2} e^{-E_{23}/kT} \frac{A_{31} E_{31}}{A_{21} E_{21}} . \quad (2.29)$$

coinciding with the line ratio predicted from levels populated with a thermodynamic equilibrium, Boltzmann distribution.

Therefore, both in the high and in the low density regime the line ratio is only a function of the temperature T of the gas. From a line ratio in

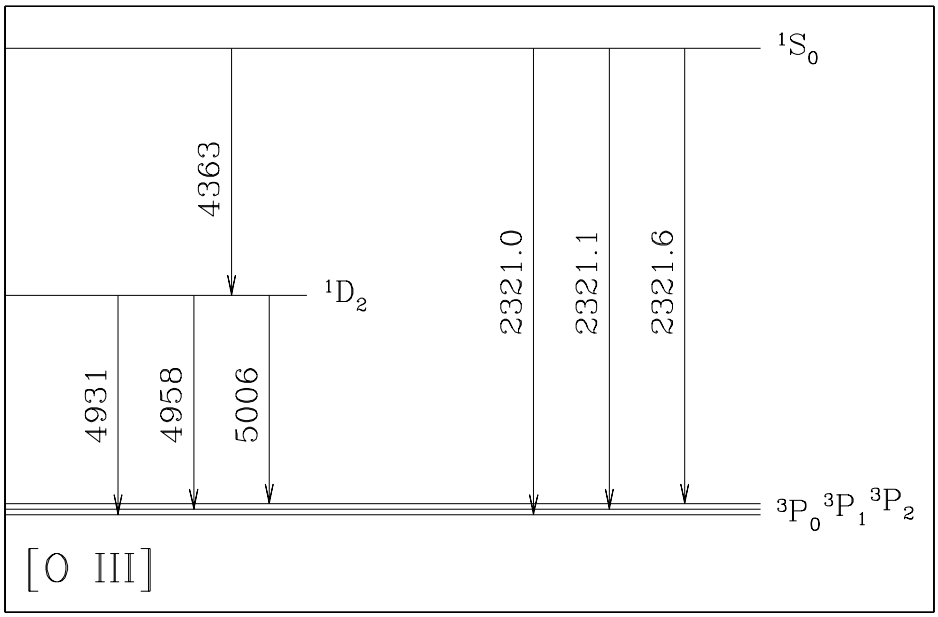

Figure 2.4: Energy level diagram showing the UV, optical and IR forbidden transitions of O III. The wavelengths of the transitions are given in Å.

one of these regimes, we can take an observed value for I_3/I_2 and use eqs. (2.28) or (2.29) to obtain a direct determination of the temperature of the emitting region. If the line ratio is not in the high or low density regime, the observed line ratio can be used to derive a relation between n_e and T (from eq. 2.27) that has to be obeyed by the electron density and temperature of the emitting region.

An interesting case is provided by ions (such as S II, see fig. 2.1) which have two close-spaced levels 2 and 3 (i. e., with $E_{23} \ll kT$). For such levels, eq. (2.27 simplyfies to

$$\frac{I_3}{I_2} \approx \left[\frac{A_{21} g_2 T^{1/2}/(n_e C \Omega_{12}) + 1}{A_{31} g_3 T^{1/2}/(n_e C \Omega_{13}) + 1}\right] \frac{\Omega_{13}}{\Omega_{12}} \frac{A_{31} E_{31}}{A_{21} E_{21}} \,. \tag{2.30}$$

Therefore, the line ratio only has the $T^{1/2}$ temperature dependence explicitly shown in eq. (2.30) and the slow dependence on T of the collision strengths. Because of this slow dependence on T, one can use "density indicators" (i. e., line ratios with $E_{23} \ll kT$) to directly obtain the electron density of the emitting gas as a function of the observed line ratio. This can be done

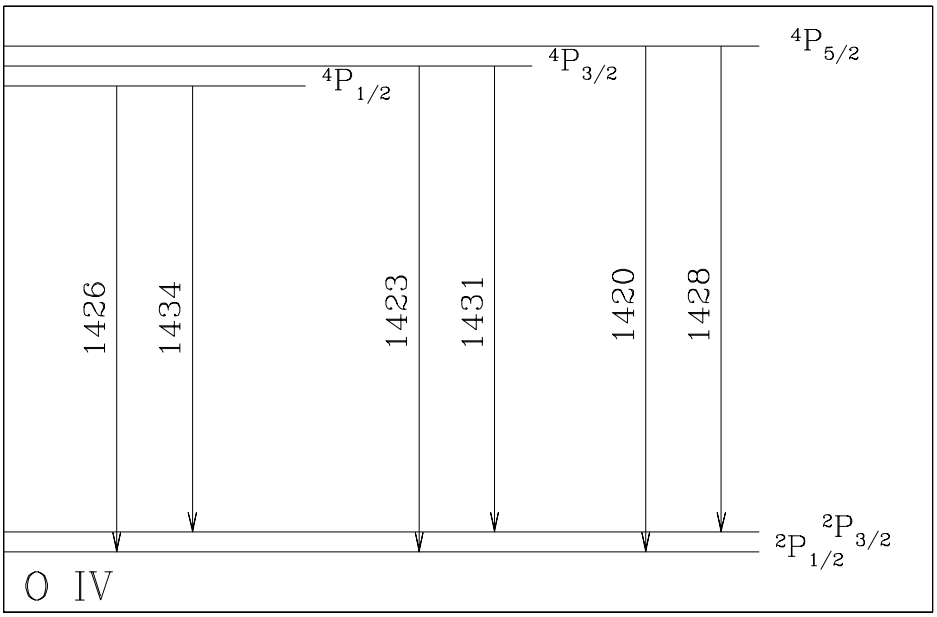

Figure 2.5: Energy level diagram showing the UV permitted/forbidden transitions of O IV. The wavelengths of the transitions are given in Å.

by, e. g., setting $T \approx 10^4$ K in eq. (2.30) and inverting it to find n_e as a function of I_3/I_2.

2.3.3 Diagnostic diagrams

In general, one can determine the fraction of atoms (or ions) in each of the excited levels by inverting the statistical equilibrium conditions given by eq. (2.15). These populations can be used to calculate the line ratios that would be produced by a homogeneous, optically thin slab :

$$\frac{I_{kl}}{I_{mn}} = \frac{n_k A_{kl} E_{kl}}{n_m A_{mn} E_{km}} \,. \tag{2.31}$$

Line ratios involving sums of lines (in the numerator and/or the denominator) are sometimes also used.

As the n_k/n_m ratio only depends on n_e and T, each of the observed line ratios determines an allowed locus in the (n_e, T) plane. Therefore, if one observes several line ratios, each of them should give an allowed locus in the

Table 2.6: A_{ij} and Ω_{ij} for the 5-level O I ion

transition		λ [Å]	$A_{i,j}$ [s^{-1}]	$\Omega = b_0 + b_1 t\,;\ t = \log_{10}(T/10^4\mathrm{K})$
$^3P_1 - ^3P_2$	2 1	6.32E5	8.92E-5	-0.00675 0.1067
$^3P_0 - ^3P_2$	3 1	4.41E5	1.0E-10	0.0026 0.0257
$^3P_0 - ^3P_2$	3 2	1.46E6	1.74E-5	-0.0102 0.0393
$^1D_2 - ^3P_2$	4 1	6300.3	0.0634	0.00365 0.1383
$^1D_2 - ^3P_1$	4 2	6363.8	0.0211	0.00215 0.0820
$^1D_2 - ^3P_0$	4 3	6393.5	7.23E-6	0.00075 0.0277
$^1S_0 - ^3P_2$	5 1	2959.2	2.88E-4	0.00065 0.0166
$^1S_0 - ^3P_1$	5 2	2972.3	0.0732	0.00035 0.0100
$^1S_0 - ^3P_2$	5 3	2979.2	0.0	0.00015 0.0033
$^1S_0 - ^1D_2$	5 4	5577.4	1.22	0.0517 0.0489

(n_e, T) plane, all of which intersect at the n_e and T values of the gas that is emitting the observed lines.

In practice, the allowed locci for three or more line ratios do not intersect exactly at the same point. This can be due to the errors in the observed line ratios and/or to the fact that the emitting region is not homogeneous.

Tables 2.7 and 2.10 give the A coefficients and polynomial fits to the collision strengths Ω from the tabulation found in Anil Pradhan's homepage (http://www.astronomy.ohio-state.edu/ pradhan/table2.ps).

2.3.4 Example: plasma diagnostics with the [S II] lines

With the coefficients given in Table 2.10 one can solve a 5-level atom problem (for the levels shown in fig. 2.1), and obtain predictions for all of the ratios between the [S II] emission lines.

Fig. (2.6) gives a few selected line ratios as a function of electron density, for three chosen temperatures (T = 5000, 10000 and 15000 K). It is clear that the line ratios between lines arising from close-lying upper levels (i. e., the 6730/16 and the 4076/68 ratios, see fig. 2.1) are good "electron density indicators" (i. e., they have a large n_e dependence and shallow T dependence). The $(6030 + 16)$ / $(4076 + 68)$ line ratio (calculated with lines from well separated upper levels, see fig. 2.1) show strong n_e and T dependences (see fig. 2.6).

Now, let us assume that observationally we determine the ratios : $I(6730)$ / $I(6716) = 1.63 \pm 0.03$, $I(4076)$ / $I(4068) = 0.305 \pm 0.015$ and $I(6730 + 16)$

Table 2.7: A_{ij} and Ω_{ij} for the 5-level O II ion

transition		λ [Å]	$A_{i,j}$ [s^{-1}]	$\Omega = b_0 + b_1 t + b_2 t^2\,;\ t = \log_{10}(T/10^4\mathrm{K})$
$^2D^0_{5/2} - ^4S^0_{3/2}$	2 1	3728.8	3.50E-5	0.7890 0.0106 0.0020
$^2D^0_{3/2} - ^4S^0_{3/2}$	3 1	3726.0	1.79E-4	0.5245 0.0104 0.0000
$^2D^0_{3/2} - ^4D^0_{5/2}$	3 2	4.97E6	1.30E-7	1.2750 -0.122 0.020
$^2P^0_{3/2} - ^4S^0_{3/2}$	4 1	2470.3	0.0057	0.2600 0.010 0.000
$^2P^0_{3/2} - ^4D^0_{5/2}$	4 2	7319.9	0.107	0.7080 0.0194 0.002
$^2P^0_{3/2} - ^4D^0_{3/2}$	4 3	7330.7	0.0578	0.3953 0.0113 0.001
$^2P^0_{1/2} - ^4S^0_{3/2}$	5 1	2470.2	0.0234	0.1318 0.0021 0.001
$^2P^0_{1/2} - ^4D^0_{5/2}$	5 2	7321.8	0.0615	0.2850 0.010 0.000
$^2P^0_{1/2} - ^4D^0_{3/2}$	5 3	7329.6	0.102	0.2630 0.0146 -0.002
$^2P^0_{3/2} - ^4P^0_{1/2}$	5 4	5.00E7	2.08E-11	0.2735 0.0132 0.000

Table 2.8: A_{ij} and Ω_{ij} for the 6-level O III ion

transition		λ [Å]	$A_{i,j}$ [s^{-1}]	$\Omega = b_0 + b_1 t + b_2 t^2\,;\ t = \log_{10}(T/10^4\mathrm{K})$
$^3P_1 - ^3P_0$	2 1	883562.	2.62E-05	0.5462 0.0666 -0.0266
$^3P_2 - ^3P_0$	3 1	326611.	3.02E-11	0.2718 0.0527 0.0209
$^3P_2 - ^3P_1$	3 2	518145.	9.76E-05	1.2959 0.2080 -0.0481
$^1D_2 - ^3P_0$	4 1	4932.6	2.74E-06	0.2555 0.0737 0.0371
$^1D_2 - ^3P_1$	4 2	4958.9	0.00674	0.7677 0.2229 0.0941
$^1D_2 - ^3P_2$	4 3	5006.7	0.0196	1.2795 0.3715 0.1543
$^1S_0 - ^3P_0$	5 1	2314.9	...	0.0328 0.0109 0.0074
$^1S_0 - ^3P_1$	5 2	2321.0	0.223	0.0983 0.0325 0.0225
$^1S_0 - ^3P_2$	5 3	2332.1	7.85E-4	0.1639 0.0545 0.0368
$^1S_0 - ^1D_2$	5 4	4363.2	1.78	0.5837 0.1952 -0.3451
$^5S^0_2 - ^3P_0$	6 1	1657.7	...	0.1342 0.0351 -0.0509
$^5S^0_2 - ^3P_1$	6 2	1660.8	212.	0.4032 0.1050 -0.1617
$^5S^0_2 - ^3P_2$	6 3	1666.1	522.	0.6718 0.1758 -0.2744

Table 2.9: A_{ij} and Ω_{ij} for the 5-level O IV ion

transition		λ [Å]	$A_{i,j}$ [s^{-1}]	$\Omega = b_0 + b_1 t + b_2 t^2\,;\ t = \log_{10}(T/10^4\mathrm{K})$
$^2P^0_{3/2} - ^2P^0_{1/2}$	2 1	2.587E5	5.18E-4	2.4020 0.9164 -1.1751
$^4P_{1/2} - ^2P^0_{1/2}$	3 1	1426.46	1.81E3	0.1332 0.0452 0.0146
$^4P_{1/2} - ^2P^0_{3/2}$	3 2	1434.07	1.77E3	0.1024 0.0625 0.0339
$^4P_{3/2} - ^2P^0_{1/2}$	4 1	1423.84	2.28E1	0.2002 0.0801 0.0422
$^4P_{3/2} - ^2P^0_{3/2}$	4 2	1431.42	3.28E2	0.2692 0.1379 0.0898
$^4P_{3/2} - ^4P_{1/2}$	4 3	1.680E6	...	1.0906 0.2002 0.1056
$^4P_{5/2} - ^2P^0_{1/2}$	5 1	1420.19	...	0.1365 0.0904 0.0625
$^4P_{5/2} - ^2P^0_{3/2}$	5 2	1427.78	1.04E3	0.5683 0.2345 0.1108
$^4P_{5/2} - ^4P_{1/2}$	5 3	3.260E5	...	0.6876 0.0359 0.4118
$^4P_{5/2} - ^4P_{3/2}$	5 4	5.620E5	1.02E-4	2.0497 0.2653 0.7749

Table 2.10: A_{ij} and Ω_{ij} for the 5-level S II ion

transition		λ [Å]	$A_{i,j}$ [s^{-1}]	$\Omega = b_0 + b_1 t + b_2 t^2\,;\ t = \log_{10}(T/10^4\mathrm{K})$
$^2D^0_{3/2} - ^4S^0_{3/2}$	2 1	6730.8	0.000882	3.112 -0.712 -0.622
$^2D^0_{5/2} - ^4S^0_{3/2}$	3 1	6716.5	0.00026	4.658 -1.066 -0.865
$^2D^0_{5/2} - ^4D^0_{3/2}$	3 2	3145000.	3.35E-07	7.124 0.750 11.734
$^2P^0_{1/2} - ^4S^0_{3/2}$	4 1	4076.4	0.0906	0.905 0.342 0.304
$^2P^0_{1/2} - ^4D^0_{3/2}$	4 2	10336.3	0.163	1.787 -0.741 2.045
$^2P^0_{1/2} - ^4D^0_{5/2}$	4 3	10373.3	0.0779	2.017 -0.791 2.320
$^2P^0_{3/2} - ^4S^0_{3/2}$	5 1	4068.6	0.225	2.015 0.583 -1.759
$^2P^0_{3/2} - ^4D^0_{3/2}$	5 2	10286.7	0.133	2.778 -1.107 3.224
$^2P^0_{3/2} - ^4D^0_{5/2}$	5 3	10320.4	0.179	4.834 -1.981 5.379
$^2P^0_{3/2} - ^4P^0_{1/2}$	5 4	2140000.	1.03E-06	2.411 0.142 -3.585

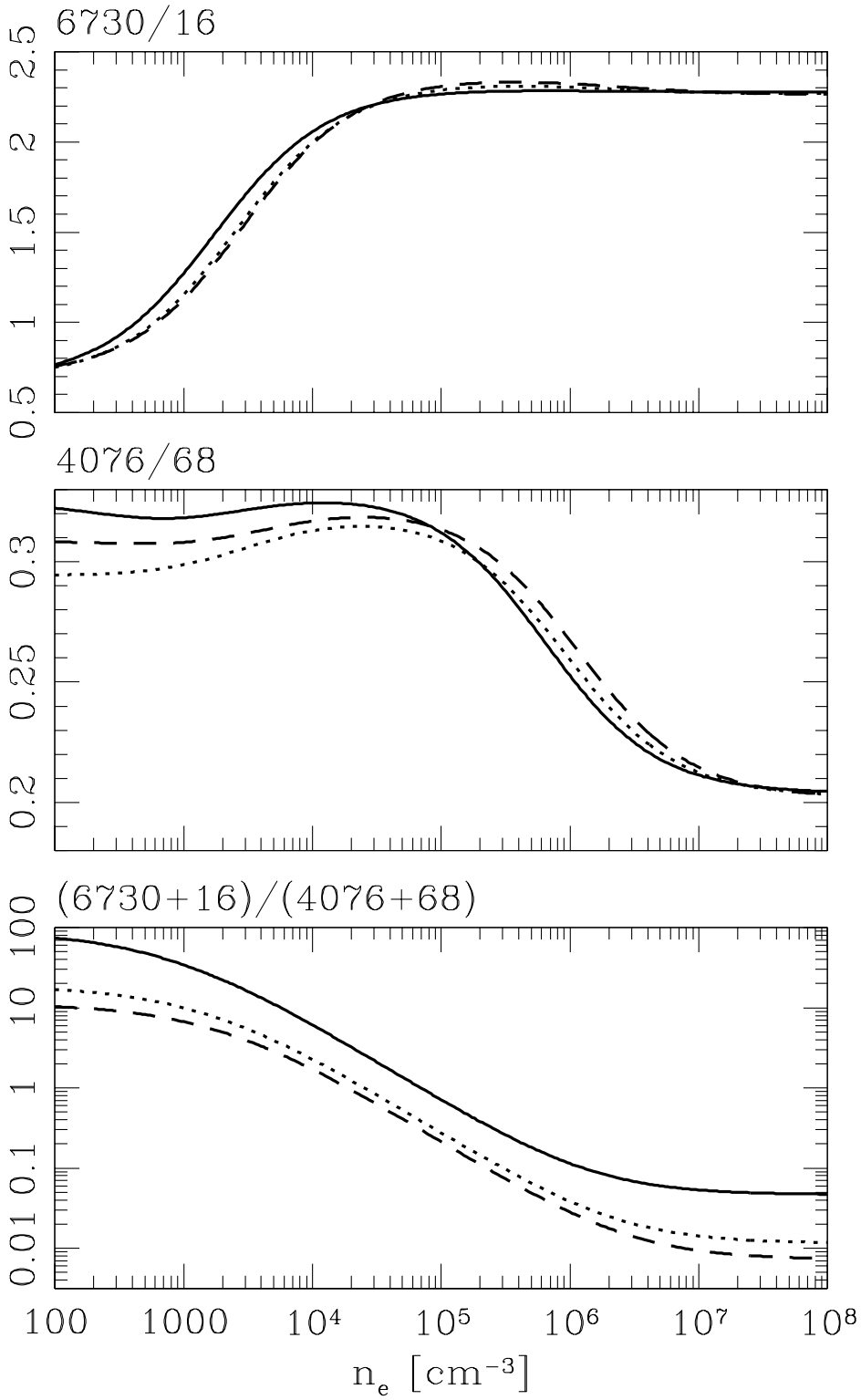

Figure 2.6: Selected [S II] line ratios given as a function of the electron density. Curves calculated for three temperatures are shown : $T = 5000$ K (solid lines), $T = 10000$ K (dotted lines) and $T = 15000$ K (dashed lines).

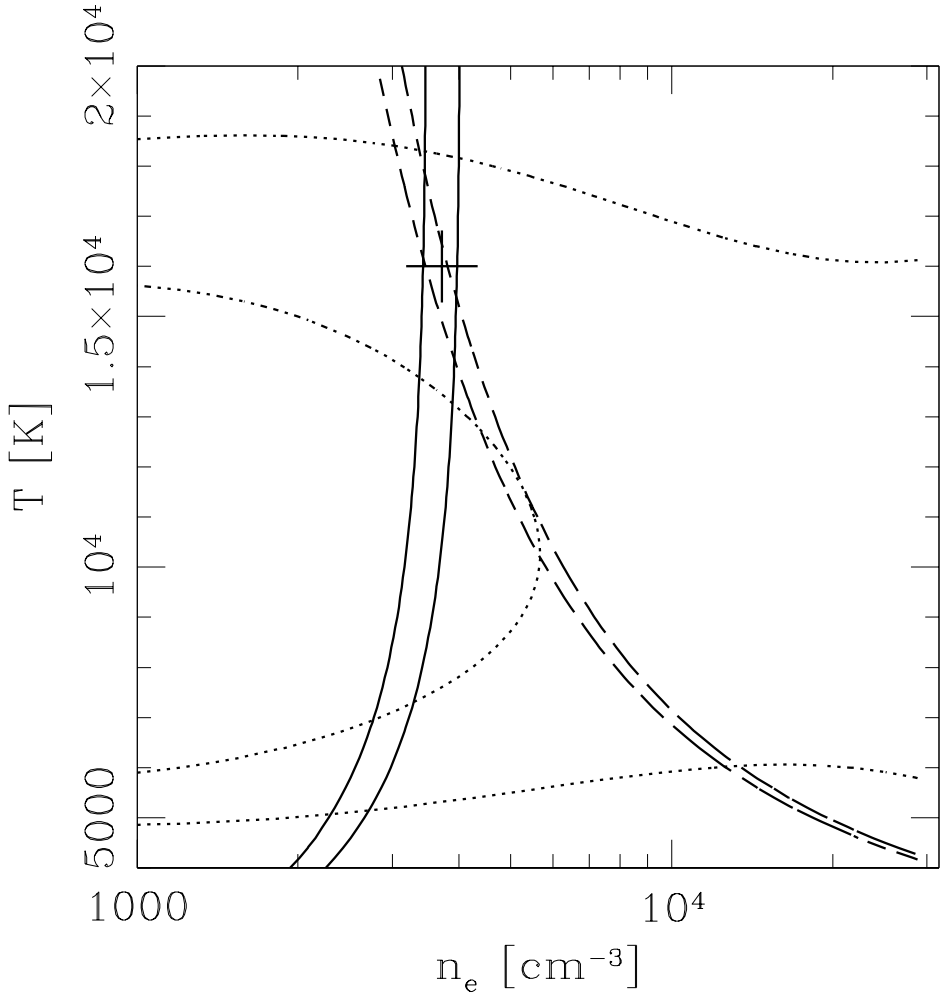

Figure 2.7: [S II] diagnostic diagram showing the regions allowed by an $I(6730)/I(6716) = 1.63 \pm 0.03$ line ratio (solid lines), an $I(4076)/I(4068) = 0.305 \pm 0.015$ ratio (dotted lines) and an $I(6730+16)/I(4076+68) = 3.4 \pm 0.1$ ratio (dashed lines). These ratios determine an electron density $n_e = 3720$ cm^{-3} and a temperature $T = 16000$ K (this point is shown with a cross).

/ $I(4076+68) = 3.4 \pm 0.1$. For each of these line ratios, the solution to the 5-level atom can be used to constrain a possible locus in the (n_e, T)-plane.

The result of this exercise is shown in fig. 2.7. Actually, for each observed line ratio we show two curves : one for the upper boundary and one for the lower boundary of the line ratio range permitted by the observational errors. An analysis of fig. 2.7 shows that a point with $n_e = 3720$ cm^{-3} and $T = 16000$ K is consistent with all of the observed line ratios.

It is also clear that the 4076/4068 line ratio does not provied a lot of information. This is a direct result of the fact that the observed 4076/4068 ratio lies in the "low density regime" (see fig. 2.6).

2.4 Continuum emission

2.4.1 General considerations

The continuum of photoionized regions has three main contributions: the recombination, free-free and two-photon continua of H. In regions in which He is in the form of He II, the He III/II recombination continuum can also have an important contribution.

2.4.2 The recombination continua

Recombinations of free electrons to an excited level N of a hydrogenic ion of charge Z (with energy $\chi_N = Z^2\chi_H/N^2$, where χ_H is the ionization potential from the ground state of H) produce photons with energies

$$h\nu = \frac{1}{2}m_e v^2 + \chi_N \,, \tag{2.32}$$

where m_e is the mass and v the velocity of the free electron.

The recombination continuum can then be calculated as a sum of the continua due to recombinations to all excited levels, which are given by

$$j_\nu^{(N)} = \frac{n_{ion} n_e}{4\pi} v \sigma_N(\nu) f(v,T) h\nu \frac{dv}{d\nu} \,, \tag{2.33}$$

where $\sigma_N(\nu)$ is the cross section for recombination to level N and

$$f(v,T) = \frac{4}{\sqrt{\pi}} \left(\frac{m_e}{2kT}\right)^{3/2} v^2 e^{-m_e v^2/(2kT)} \,, \tag{2.34}$$

is the Maxwell-Boltzmann distribution of the electrons, and $dv/d\nu = h/(m_e v)$ [obtained from the relation $d(m_e v^2/2) = d(h\nu)$, see eq. 2.32].

From the principle of detailed balancing, it is possible to derive a Milne relation of the form:

$$\sigma_N(v) = \frac{w_{HI}}{w_{HII}} \frac{h^2\nu^2}{m_e^2 c^2 v^2} a_N(\nu)\,, \tag{2.35}$$

where $a_N(\nu)$ is the photoionization cross section from level N and $w_{HI} \approx 2$ and $w_{HII} = 1$ are the HI and HII partition functions, respectively. This relation is derived in Appendix 1 of the book of Osterbrock (1989).

Combining eqs. (2.32-2.35), we obtain:

$$j_\nu^{(N)} = \frac{n_{HII} n_e}{4\pi} \gamma_N(\nu)\,, \tag{2.36}$$

with

$$\gamma_N(\nu) = \left(\frac{2}{\pi}\right)^{1/2} \frac{2N^2 h^4 \nu^3}{c^2 (m_e kT)^{3/2}} a_N(\nu)\, e^{(\chi_N - h\nu)/kT}\,. \tag{2.37}$$

Given the photoionization cross section $a_N(\nu)$, eqs. (2.36-2.37) then give us the continua to all levels N of a hydrogenic ion.

For a hydrogenic ion of charge Z, the photoionization cross section $a_N(\nu)$ is given by

$$a_N(Z,\epsilon) = 7.907 \times 10^{-18} \mathrm{cm}^2 \frac{N}{Z^2} \left(1 + N^2\epsilon\right)^{-3} g_{bf}(N,\epsilon)\,, \tag{2.38}$$

for $\epsilon \geq 0$ and $a_N(Z,\epsilon) = 0$ for $\epsilon < 0$. The photon energy is

$$h\nu = Z^2 \chi_H \left(\frac{1}{N^2} + \epsilon\right)\,, \tag{2.39}$$

with $\chi_H = 13.6$ eV, and the g_{II} Gaunt factor is approximately given by

$$g_{bf}(N,\epsilon) = 1 + 0.1728 N^{-2/3}(u+1)^{-2/3}(u-1) - 0.0496 N^{-4/3}(u+1)^{-4/3}(u^2 + 4u/3 + 1)\,, \tag{2.40}$$

with $u = N^2\epsilon$ (see Seaton 1960). The precision of this expansion for the Gaunt factor has been evaluated by Brown & Mathews (1970).

Finally, the total bound-free emission of the hydrogenic ion can be written as :

$$j_\nu = \frac{n_Z n_e}{4\pi} \gamma(\nu)\,, \tag{2.41}$$

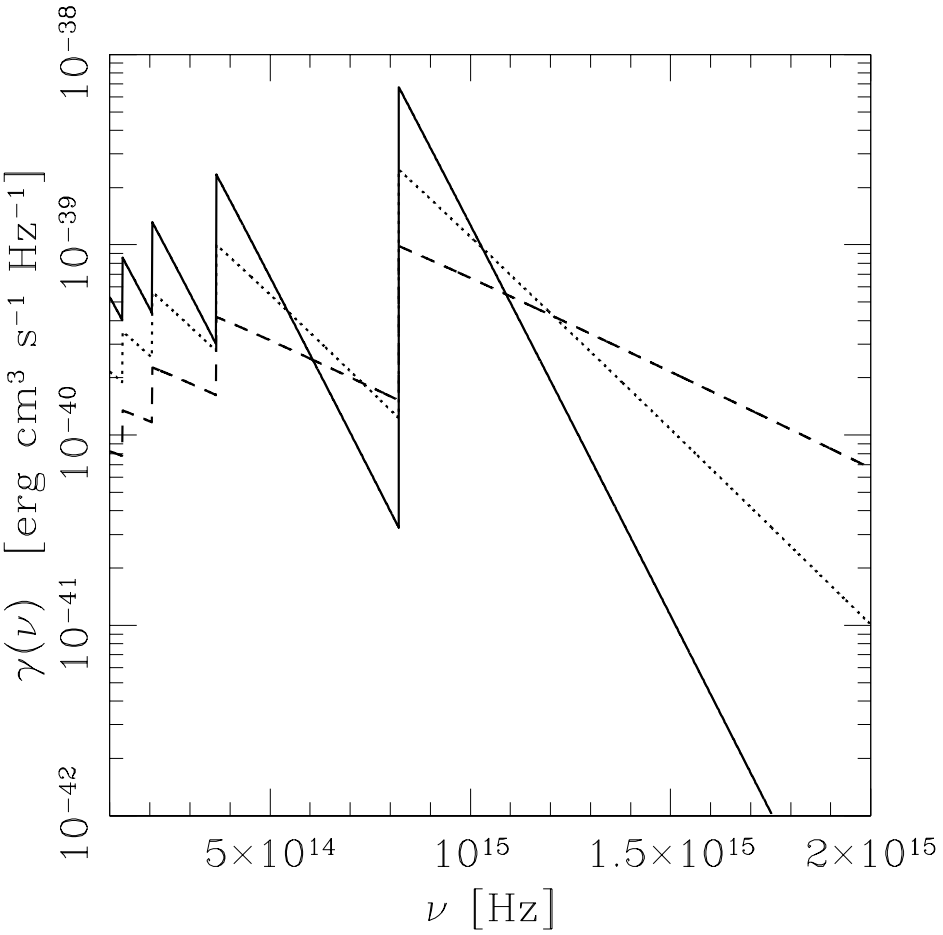

Figure 2.8: Recombination continuum of H. Curves calculated for three temperatures are shown : $T = 5000$ K (solid line), $T = 10000$ K (dotted line) and $T = 20000$ K (dashed line).

with

$$\gamma(\nu) = \sum_{N \geq 1} \gamma_N(\nu)\,. \tag{2.42}$$

The $\gamma(\nu)$ coefficient obtained for H (i. e., setting $Z = 1$) is plotted in Fig. 2.8 for three chosen values of the temperature T. It is clear that the slopes of the continua as well as the "jumps" at the frequencies corresponding to the ionization energies of the levels of H depend quite strongly on the temperature. Therefore, observed values for these parameters can be used as a temperature diagnostic of the emitting plasma.

The formalism used above can be of course be used to derive the HeII recombination continuum (by setting $Z = 2$ in all of the expressions). The intensity of this continuum can be comparable to the H recombination continuum in regions where He is twice ionized. The recombination continuum of HeI has γ values (see eq. 2.41, setting $n_Z = n_{HeII}$) which are similar to the ones of HI (see Brown & Mathews 1970). The HeI recombination emission coefficient is therefore of order 10% of the HI emission coefficient (for an He/H$\sim$ 0.1 abundance).

2.4.3 The free-free continua

The free-free continuum emission coefficient due to electron transitions in the electric field of an ion of charge Z is given by:

$$j_\nu = \frac{n_e n_Z}{4\pi} \frac{32 Z^2 e^4 h}{3 m_e^2 c^3} \left(\frac{\pi \chi_{Z-1}}{3kT}\right)^{1/2} e^{-h\nu/kT}\, g_{ff}(T, Z, \nu)\,, \tag{2.43}$$

where χ_{Z-1} is the ionization potential of the ion with charge $Z - 1$. For a hydrogenic ion $\chi_{Z-1} = Z^2 \chi_H$, and the Gaunt factor g_{ff} is given by :

$$g_{ff}(T, Z, \nu) = 1 + 0.1728 \left(\frac{h\nu}{Z^2 \chi_H}\right)^{1/3} (1 + 2\mu) - 0.0496 \left(\frac{h\nu}{Z^2 \chi_H}\right)^{2/3} \left(1 + 2\mu/3 + 4\mu^2/3\right) \tag{2.44}$$

with $\mu = kT/h\nu$ (see Seaton 1960). This expression leads to $g_{ff} \approx 1$ for the optical region of the spectrum.

The free-free continuum dominates the radio spectrum. For radio frequencies, an appropriariate expression for the Gaunt factor is:

$$g_{ff}(T, Z, \nu) = \frac{\sqrt{3}}{\pi} \left[\ln\left(\frac{8k^3 T^3}{\pi^2 Z^2 e^4 m_e \nu^2}\right)^{1/2} - 1.4425\right]\,. \tag{2.45}$$

With eqs. (2.43-2.45) we can compute the free-free continua of HII and HeIII (setting $n_Z = n_{HII}$, $Z = 1$ and $n_Z = n_{HeIII}$, $Z = 2$, respectively). It is usual practice to include the HeII free-free continuum as well as the HeI recombination continuum in an approximate way by assuming that they have the same temperature and frequency dependence as the corresponding H emission coefficients. As the HeI recombination and HeII free-free continua are down by an order of magnitude with respect to the H continua, this assumption does not introduce a large error in the computed continuum spectrum.

2.4.4 The two-photon continuum

Electrons in the 2s state of H decay to the 1s level through a 2-photon transition with Einstein coefficient $A_{2s,1s} = 8.23\ \mathrm{s}^{-1}$ (see table 2.2).

The emission coefficient is given by :

$$j_\nu^{(2q)} = \frac{n_{2s} A_{2s,1s}}{4\pi} g(\nu)\,, \tag{2.46}$$

where $g(y)$ is given in table 2.11 (tha values are taken from Brown & Mathews 1970). An analytic fit to these values is :

$$g_a(y) = 9.23 \exp\left\{ - \left[\eta/0.3\right]^{(1.3+1.6\eta)} \right\} - 0.61\,, \tag{2.47}$$

in units of 10^{-27} erg Hz^{-1}, with $\eta = 0.5 - y$ and $y = \nu/\nu_{21}$ ($\nu_{21} = 3\chi_H/4h$ being the frequency of the $2 \rightarrow 1$ transition of H). The analytic fit in eq. (2.47) is valid for $y \leq 0.5$. For $y > 0.5$, the relation

$$g(1-y) = \frac{(1-y)\ g(y)}{y}\,, \tag{2.48}$$

should be used in order to compute the $g(y)$ function from the analytic fit (eq. 2.47). This equation represents the fact that the photon distribution (i. e., of the number of emitted photons) is symmetric with respect to $\nu_{21}/2$. The errors of the analytic fit obtained from eqs. (2.47-2.48) can be appreciated in fig. 2.9. We should note that the function $g_a(y)$ (eq. 2.47) becomes negative for $0 \leq y < 0.015$ and should therefore be set to zero. Because of this feature, the cutoff at high energies of the 2-photon continuum computed with eq. (2.47) is shifted by 1.5 % with respect to ν_{21}.

Table 2.11: Frequency dependence of the H 2-photon emission

$y = \nu/\nu_{21}$	$g(y)$ $[10^{-27}$erg Hz$^{-1}]$	$y = \nu/\nu_{21}$	$g(y)$ $[10^{-27}$erg Hz$^{-1}]$
0.00	0.0	0.55	9.46
0.05	0.303	0.60	10.17
0.10	0.978	0.65	10.77
0.15	1.836	0.70	11.12
0.20	2.78	0.75	11.34
0.25	3.78	0.80	11.12
0.30	4.80	0.85	10.40
0.35	5.80	0.90	8.80
0.40	6.78	0.95	5.76
0.45	7.74	1.00	0.0
0.50	8.62		

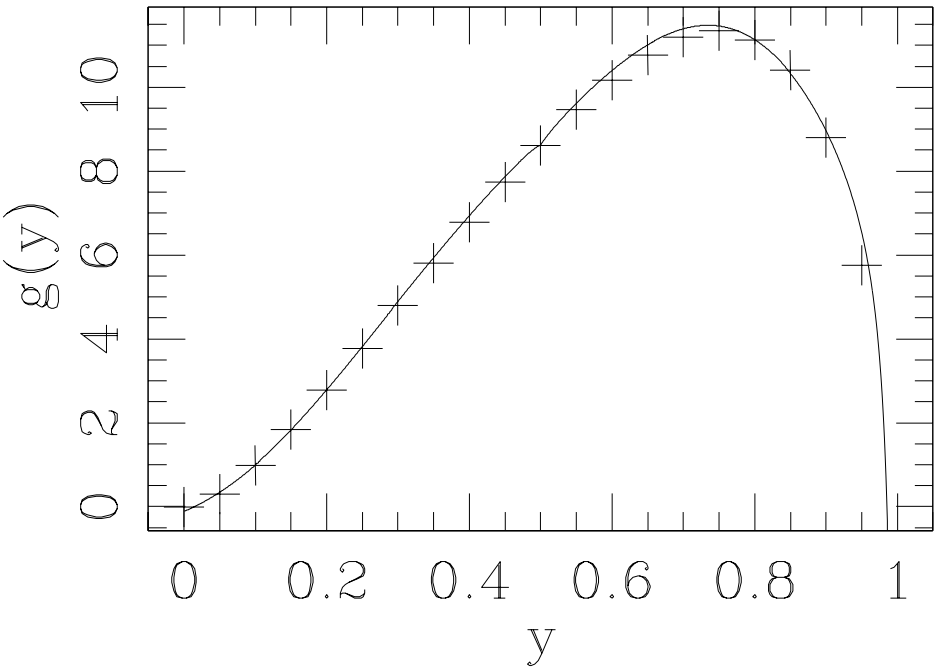

Figure 2.9: Frequency dependence of the 2-photon continuum of H : $g(y)$ (in 10^{-27}erg Hz^{-1}) as a function of $y = \nu/\nu_{21}$. The crosses are the values of Brown & Mathews (1970) and the solid line the analytic fit described in the text.

The simplest possible way of calculating the population of n_{2s} of the $2s$ level is to assume a balance of the form :

$$n_{2s}\left(A_{2s,1s}+n_e q^{(e)}_{1s,2s}+n_{HII}q^{(p)}_{1s,2s}\right)=n_e n_{HII}\alpha_{2s}(T)\,, \qquad (2.49)$$

where the collisional rates $q^{(e)}$ and $q^{(p)}$ can be calculated with the corresponding collision strengths given in tables 2.2 and 2.5. The effective recombination coefficient to the $2s$ level $\alpha_{2s}(T)$ has been tabulated by Brown & Mathews (1970), and can be obtained from the interpolation formula:

$$\log_{10}\left[\alpha_{2s}(T)\right]=-13.077-0.696t-0.0987t^2\,;\;\; t=\log_{10}(T/10^4\mathrm{K})\,, \quad (2.50)$$

in erg cm^3 s^{-1}. Eq. (2.49) represents the balance between the recombination cascade electrons that end in level $2s$ (right hand term) and the electrons that leave $2s$ through 2-photon transitions to $1s$ or through collisional transitions to the $2p$ level. At high enough optical depths of the Lyα line, the population of level $2p$ can be high enough for $2p \rightarrow 1s$ collisional transitions to become important. This effect is discussed by Brown & Mathews (1970). Another possibly important effect is found in a partially neutral gas of temperatures $T \geq 12000$ K, in which $1s \rightarrow 2s$ collisional transitions can be important. This effect can lead to a hugely increased intensity of the 2-photon continuum.

Combining eqs. (2.46) and (2.49) we then obtain :

$$j^{(2q)}_{\nu}=\frac{n_e n_{HII}\alpha_{2s}(T)g(\nu)}{4\pi\left[1+\left(n_e q^{(e)}_{1s,2s}+n_{HII}q^{(p)}_{1s,2s}\right)/A_{2s,1s}\right]}\,. \qquad (2.51)$$

A more detailed model for the intensity of the 2-photon continuum would involve a solution of the recombination cascade with collisions in order to obtain a better estimate of n_{2s}.

Part II

Dynamics of the ISM

Chapter 3

The equations of gasdynamics

3.1 General considerations

It is in principle possible to derive the gasdynamic equations as velocity moments of Vlasov's equation (for a single particle distribution function). In its turn, Vlasov's equation can be derived from Liouville's theorem (i. e., the fundamental equation of statistical mechanics) through methods such as the "BBGKY" heirarchy. These derivations can be found in most standard plasma physics or particle kinetics books. In this chapter, we will describe the mathematically simple and physically more inspiring "macroscopic derivation" of the gasdynamic equations (described in different forms in most books on gasdynamics or hydrodynamics).

In order to be able to describe a gas (a system of many, possibly interacting particles) to be described as a fluid, the following conditions must be satisfied :

- the mean free path λ of the particles must be much smaller than the characteristic distance L of the spatial variations of the macroscopic variables of the gas (such as the density),
- the mean time between collisions t_{coll} must be much smaller than the characteristic timescale t_{flow} of changes in the flow,
- the mean distance $l \sim n^{-1/3}$ (where n is the number density) between neighbouring particles.

The $\lambda \ll L$ condition implies that the gas particles effectively see an infinite, homogeneous environment, and therefore (provided that the $t_{coll} \ll$

t_{flow} condition is also satisfied) attain a local thermodynamic equilibrium. This means that in a reference system moving with the flow the particles have a TE, Maxwell-Boltzmann velocity distribution (with a well defined local temperature T). Therefore, the thermal energy and the pressure/density/temperature law are given by the relations obtained for a (real or ideal) gas in TE.

The $n^{-1/3} \ll L$ condition implies that one can have small volumes in which the flow variables are approximately constant, but which still have very large numbers of particles within them, so that a fluid description is still meaningful within these volumes. As we will see in the following sections, this is a fundamental assumption necessary for deriving the gasdynamic equations.

3.2 Macroscopic derivation

Let us consider a control volume element V, surrounded by a surface S, which has a fixed position and shape as a function of time. Such a fixed volume element (surrounded by an immaterial surface) is called an "Eulerian" control volume. The gas freely flows through this control volume (see Fig. 3.1).

3.3 Fluxes

Let us consider a fixed surface element ΔS, through which flows the gas at a velocity $\underline{u}$. From the diagram shown in figure 3.2, it is clear that all of the material within the volume

$$\Delta V = u_n \, \Delta t \, \Delta S \tag{3.1}$$

(where u_n is the flow velocity normal to the surface element) goes through ΔS in a time Δt.

Therefore, if we have any volumetric quantity A of the flow (for example, we could have $A = \rho$, the mass density of the gas), the flux of this quantity through a unit surface is :

$$F_A = \frac{A \Delta V}{\Delta t \, \Delta S} = A u_n \, . \tag{3.2}$$

For example, for the $A = \rho$ case, F_A corresponds to the mass per unit area and time going through a surface oriented such that u_n is the normal velocity.

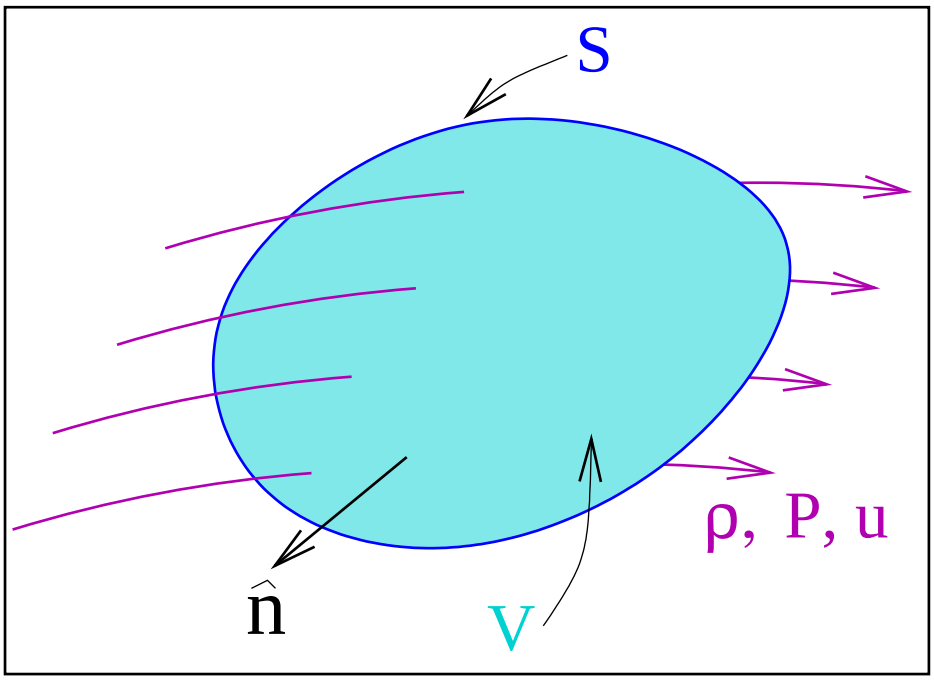

Figure 3.1: An imaginary, fixed ("Eulerian") control volume through which flows a continuous medium of density ρ, pressure P and flow velocity $\underline{u}$. The volume V is surrounded by the surface S. The surface has an outward pointing normal unit vector $\hat{n}$.

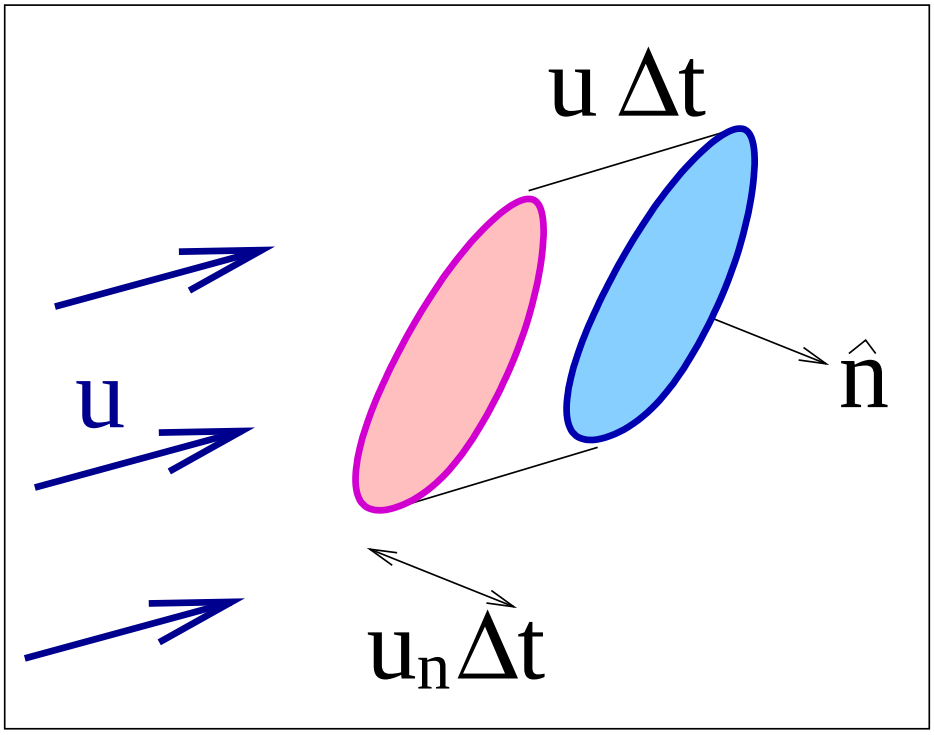

Figure 3.2: The gas (with velocity $\underline{u}$) flows through a fixed surface element (in blue) ΔS, with normal vector $\hat{n}$.

One can then define a vector flux

$$\underline{F_A} = A\underline{u}\,, \tag{3.3}$$

and the mass going through a surface with normal unit vector $\hat{n}$ (per unit area and time) is then given by

$$F_A = \underline{F_A} \cdot \hat{n}\,. \tag{3.4}$$

3.4 The continuity equation

Let us now consider the mass

$$M = \iiint_V \rho\, d^3x \tag{3.5}$$

within the control volume V shown in figure 3.1. In the absence of mass sources or sinks, M will change only as the result of the net mass going in/out through the surface S :

$$\frac{\partial M}{\partial t} = -\oiint_S \rho\underline{u} \cdot \hat{n}\, dS\,, \tag{3.6}$$

where $\rho\underline{u}$ is the mass flux (see §3.3), the "$-$" sign accounts for the fact that $\hat{n}$ points outwards. Combining equations (3.5-3.6), using Gauss's theorem for converting the surface integral into a volume integral and commuting the time derivative with the volume integral, we then obtain :

$$\iiint_V \left[\frac{\partial \rho}{\partial t} + \nabla \cdot (\rho\underline{u})\right] d^3x = 0\,. \tag{3.7}$$

The final step is obtained by noting that for a volume $V \ll L^3$ (where L is the characteristic length of variations along the flow), the integral in eq. (3.7) will have a value $= [\,]\,V$, where the integrand "$[\,]$" is evalued in any point within the volume V. We should note that for a fluid approximation to be valid, a volume satisfying the $V \ll L^3$ condition can still have a very large number of particles within it (see §3.1). Therefore, eq. (3.7) implies that

$$\frac{\partial \rho}{\partial t} + \nabla \cdot (\rho\underline{u}) = 0\,, \tag{3.8}$$

for all times and positions. This differential equation is called the "continuity equation" of gasdynamics.

3.5 The momentum equation

Let us now consider the momentum along the i-th direction

$$\Pi_i = \iiint_V \rho u_i \, d^3x \tag{3.9}$$

within the control volume V shown in figure 3.1, where u_i ($i = 1, 2, 3$) is the i-th component of the flow velocity.

The momentum conservation equation can then be written as :

$$\frac{\partial \Pi_i}{\partial t} = - \oiint_S \rho u_i \underline{u} \cdot \hat{n} \, dS - \oiint_S P \hat{e}_i \cdot \hat{n} \, dS \, , + \iiint_V f_i \, d^3x \tag{3.10}$$

where the first term on the right represents the net amount of i-th momentum going in or out through the surface of the volume element (see fig. 3.1), the second term is the i-th component of the force of the gas pressure on the volume element, and the third term represents the force on the volume due to an external force (per unit volume) f_i acting on the flow along the i-th direction (this could be, e. g., the force due to gravity). The $\hat{e}_i$ are the unit vectors along the coordinate axes.

Following the method of §3.4, from eq. (3.10) we derive :

$$\frac{\partial \rho u_i}{\partial t} + \nabla \cdot (\rho u_i \underline{u}) + \frac{\partial P}{\partial x_i} = f_i \, . \tag{3.11}$$

For the case of a gravitational force, we would have $f_i = \rho g_i$ (with g_i the i-th component of the gravitational acceleration).

3.6 The energy equation

We now consider the equation for the kinetic+thermal energy per unit volume

$$E = \frac{1}{2} \rho u^2 + \frac{P}{\gamma - 1} \, , \tag{3.12}$$

where u is the modulus of the flow velocity and $\gamma = C_p / C_v$ is the specific heat ratio ($= 5/3$ for a monoatomic gas, and $= 7/5$ for diatomic molecules with thermalized rotation states).

For deriving the equation we consider the energy flux $E\underline{u}$, the work $P\underline{u}$ of the pressure force on the surface of the control volume, the work $\underline{f} \cdot \underline{u}$ of possible external forces $\underline{f}$ (per unit volume), and the net energy gain/loss per unit volume $G - L$ due to emission/absorption of radiation. Following the method of §3.4, one obtains the energy equation :

$$\frac{\partial E}{\partial t} + \nabla \cdot [\underline{u}\,(E + P)] = G - L + \underline{f} \cdot \underline{u}\,. \tag{3.13}$$

The "gasdynamic" or "Euler" equations (eqs. 3.8, 3.11 and 3.13) are a closed set of differential equations from which one can in principle derive ρ, $\underline{u}$ and P as a function of position and time, for any given set of initial and boundary conditions. In the following sections, we present the Euler equations in different notations and for different coordinate systems.

3.7 Different forms of the Euler equations

3.7.1 Using Einstein's notation

Continuity equation :

$$\frac{\partial \rho}{\partial t} + \frac{\partial}{\partial x_i}\,(\rho u_i) = 0\,, \tag{3.14}$$

Momentum equation :

$$\frac{\partial \rho u_j}{\partial t} + \frac{\partial}{\partial x_i}\,(\rho u_i u_j + P\delta_{ij}) = f_i\,, \tag{3.15}$$

Energy equation :

$$\frac{\partial E}{\partial t} + \frac{\partial}{\partial x_i}\,[u_i\,(E + P)] = G - L + f_i u_i\,, \tag{3.16}$$

where $E = u_i u_i/2 + P/(\gamma - 1)$.

In these equations, i, j =1, 2, 3 represent the three coordinates of a Cartesian reference system. If one of these indeces appears twice in one term, a sum from 1 to 3 is implied. For example,

$$u_i u_i = \sum_{i=1}^{3} u_i u_i\,, \tag{3.17}$$

$$\frac{\partial}{\partial x_i}\left(\rho u_i u_j\right) = \sum_{i=1}^{3} \frac{\partial}{\partial x_i}\left(\rho u_i u_j\right) \,. \tag{3.18}$$

3.7.2 In vector/tensor notation

Continuity equation :

$$\frac{\partial \rho}{\partial t} + \nabla \cdot (\rho \underline{u}) = 0 \,, \tag{3.19}$$

Momentum equation :

$$\frac{\partial \rho \underline{u}}{\partial t} + \nabla \cdot \left(\rho \underline{\underline{u u}} + P \underline{\underline{I}}\right) = \underline{f} \,, \tag{3.20}$$

Energy equation :

$$\frac{\partial E}{\partial t} + \nabla \cdot \left[\underline{u}\,(E + P)\right] = G - L + \underline{f} \cdot \underline{u} \,. \tag{3.21}$$

In the momentum equation, $\underline{\underline{I}} = \delta_{ij}$ is the unit second rank tensor. A Cartesian coordinate system is assumed.

3.7.3 Cartesian equations, all terms written explicitly

Following the normal notation used in gasdynamics, we name (u, v, w) the three components of the flow velocity $\underline{u}$, along the axes of an (x, y, z), Cartesian reference system.
Continuity equation :

$$\frac{\partial \rho}{\partial t} + \frac{\partial}{\partial x}\rho u + \frac{\partial}{\partial y}\rho v + \frac{\partial}{\partial z}\rho w = 0 \,, \tag{3.22}$$

Momentum equation(s) :

$$\frac{\partial}{\partial t}\rho u + \frac{\partial}{\partial x}\rho u^2 + \frac{\partial}{\partial y}\rho uv + \frac{\partial}{\partial z}\rho uw + \frac{\partial P}{\partial x} = f_x \,, \tag{3.23}$$

$$\frac{\partial}{\partial t}\rho v + \frac{\partial}{\partial x}\rho uv + \frac{\partial}{\partial y}\rho v^2 + \frac{\partial}{\partial z}\rho vw + \frac{\partial P}{\partial y} = f_y \,, \tag{3.24}$$

$$\frac{\partial}{\partial t}\rho w + \frac{\partial}{\partial x}\rho uw + \frac{\partial}{\partial y}\rho vw + \frac{\partial}{\partial z}\rho w^2 + \frac{\partial P}{\partial z} = f_z \,, \tag{3.25}$$

Energy equation :

$$\frac{\partial E}{\partial t} + \frac{\partial}{\partial x}u(E+P) + \frac{\partial}{\partial y}v(E+P) + \frac{\partial}{\partial z}w(E+P) = G - L + uf_x + vf_y + wf_z\,, \tag{3.26}$$

where $E = \rho(u^2+v^2+w^2)/2 + P/(\gamma-1)$.

3.7.4 2D Cartesian equations, all terms written explicitly

We name (u, v) the two components of the flow velocity $\underline{u}$, along the axes of an (x, y), Cartesian reference system.
Continuity equation :

$$\frac{\partial \rho}{\partial t} + \frac{\partial}{\partial x}\rho u + \frac{\partial}{\partial y}\rho v = 0\,, \tag{3.27}$$

Momentum equation(s) :

$$\frac{\partial}{\partial t}\rho u + \frac{\partial}{\partial x}\rho u^2 + \frac{\partial}{\partial y}\rho uv + \frac{\partial P}{\partial x} = f_x\,, \tag{3.28}$$

$$\frac{\partial}{\partial t}\rho v + \frac{\partial}{\partial x}\rho uv + \frac{\partial}{\partial y}\rho v^2 + \frac{\partial P}{\partial y} = f_y\,, \tag{3.29}$$

Energy equation :

$$\frac{\partial E}{\partial t} + \frac{\partial}{\partial x}u(E+P) + \frac{\partial}{\partial y}v(E+P) = G - L + uf_x + vf_y\,, \tag{3.30}$$

where $E = \rho(u^2+v^2)/2 + P/(\gamma-1)$.

3.7.5 2D cylindrical equations, all terms written explicitly

We name (u, v) the two components of the flow velocity $\underline{u}$, along the axes of an (z, r), cylindrical reference system.
Continuity equation :

$$\frac{\partial \rho}{\partial t} + \frac{\partial}{\partial z}\rho u + \frac{\partial}{\partial r}\rho v + \frac{\rho v}{r} = 0\,, \tag{3.31}$$

Momentum equation(s) :

$$\frac{\partial}{\partial t}\rho u + \frac{\partial}{\partial z}\rho u^2 + \frac{\partial}{\partial r}\rho uv + \frac{\partial P}{\partial z} + \frac{\rho uv}{r} = f_z\,, \tag{3.32}$$

$$\frac{\partial}{\partial t}\rho v + \frac{\partial}{\partial z}\rho uv + \frac{\partial}{\partial r}\rho v^2 + \frac{\partial P}{\partial r} + \frac{\rho v^2}{r} = f_r\,, \tag{3.33}$$

Energy equation :

$$\frac{\partial E}{\partial t} + \frac{\partial}{\partial x}u(E+P) + \frac{\partial}{\partial y}v(E+P) + \frac{vE}{r} = G - L + uf_z + vf_r\,, \tag{3.34}$$

where $E = \rho(u^2+v^2)/2 + P/(\gamma-1)$.

3.7.6 1D equations

Continuity equation :

$$\frac{\partial \rho}{\partial t} + \frac{\partial}{\partial x}\rho u + \frac{\eta \rho u}{x} = 0\,, \tag{3.35}$$

Momentum equation :

$$\frac{\partial}{\partial t}\rho u + \frac{\partial}{\partial x}(\rho u^2 + P) + \frac{\eta \rho u^2}{x} = f\,, \tag{3.36}$$

Energy equation :

$$\frac{\partial E}{\partial t} + \frac{\partial}{\partial x}u(E+P) + \frac{\eta u E}{x} = G - L + uf\,, \tag{3.37}$$

where $E = \rho u^2/2 + P/(\gamma-1)$. For $\eta = 0$, 1 and 2, we have the 1D Cartesian, cylindrical (with $x = r$, the cylindrical radius) and spherical (with $x = R$, the spherical radius) Euler equations, respectively.

3.8 Gasdynamic equations in Lagrangean form

The "Lagrangean" description of a flow is based on considering a "Lagrangean" fluid parcel, which moves and changes shape following the motion and distortion of the fluid. The free variables in such a description are the initial coordinates $\underline{x}_0$ of all fluid parcels, and the time t. The position of the parcels $\underline{x}$ is obtained as a function of $\underline{x}_0$ and t through the solution to the gasdynamic equations.

Using the chain rule, it is evident that

$$\frac{d}{dt}[\,] = \frac{\partial}{\partial t}[\,] + \underline{u} \cdot \nabla[\,], \tag{3.38}$$

where the total time-derivative is the Lagrangean derivative (i. e., following a fluid parcel) and the partial time-derivative is the Eulerian one (i. e., at a fixed spatial position).

One can then take the Euler equations (in the form given by Eqs. 3.19-3.21) and combine them with Eq. (3.38) to obtain the Lagrangean gasdynamic equations :
Continuity equation :

$$\frac{d\rho}{dt} + \rho \nabla \cdot \underline{u} = 0\,, \tag{3.39}$$

Momentum equation (in the form of Newton's second law) :

$$\rho \frac{d\underline{u}}{dt} + \nabla P = \underline{f}\,, \tag{3.40}$$

Energy equation :

$$\frac{d\epsilon}{dt} + P\frac{d}{dt}\left(\frac{1}{\rho}\right) = \frac{G-L}{\rho}\,, \tag{3.41}$$

where $\epsilon = P/(\gamma-1)\rho$ is the thermal energy per unit mass of the gas.

It is also possible to combine the terms of Eq. (3.41) to derive the "entropy equation" :

$$\frac{d}{dt}\left(P\rho^{-\gamma}\right) = \frac{(\gamma-1)}{\rho^{\gamma}}\left(G-L\right)\,, \tag{3.42}$$

with $S = \ln\left(P\rho^{-\gamma}\right)$ being the specific entropy of the gas.

Chapter 4

Sound waves and linear stability analysis

4.1 General considerations

In this chapter we discuss a few solutions to the gasdynamic equations which are fundamental for applications to astrophysical flows.

4.2 Sound waves

Let us consider the propagation of a 1D (plane) sound wave. A sound wave is defined as a small perturbation (in density, velocity and pressure) which travels through a gas. We will consider the most simple case of a medium which is initially homogeneous (with constant density ρ_0 and pressure P_0) and at rest (zero velocity). We then write the perturbed density, pressure and velocity as

$$P + P_0\,, \quad \rho + \rho_0\,, \quad u\,, \tag{4.1}$$

with $P \ll P_0$, $\rho \ll \rho_0$ and u "with small values" (we will discuss later what this actually means).

If we insert these variables into the 1D, plane gasdynamic equations (Eqs. 3.35-3.37), we obtain

$$\frac{\partial}{\partial t}\left[\rho + \rho_0\right] + \frac{\partial}{\partial x}\left[\left(\rho + \rho_0\right) u\right] = 0\,, \tag{4.2}$$

$$\frac{\partial}{\partial t}\left[(\rho+\rho_0)\,u\right]+\frac{\partial}{\partial x}\left[(\rho+\rho_0)\,u^2+P+P_0\right]=0\,, \tag{4.3}$$

$$\frac{\partial}{\partial t}\left[E\right]+\frac{\partial}{\partial x}\left[u\,(E+P+P_0)\right]=0\,, \tag{4.4}$$

with $E=(\rho+\rho_0)u^2/2+(P+P_0)/(\gamma-1)$.

We now consider that ρ_0 and P_0 are constant, and we neglect all terms with quadratic or cubic dependence on the perturbations (and their spatial or time derivatives). In practive we elliminate all terms involving the terms ρu, u^2 or uP. In this way, we obtain the linearized, plane gasdynamic equations :

$$\frac{\partial\rho}{\partial t}+\rho_0\frac{\partial u}{\partial x}=0\,, \tag{4.5}$$

$$\rho_0\frac{\partial u}{\partial t}+\frac{\partial P}{\partial x}=0\,, \tag{4.6}$$

$$\frac{\partial P}{\partial t}+\gamma P_0\frac{\partial u}{\partial x}=0\,. \tag{4.7}$$

We now play at combining these equations to obtain differential equations for each of the perturbed variables (ρ, P and u). For example, if we take the time derivative of Eq. (4.6), and subtract from this the spatial derivative of Eq. (4.7), we obtain

$$\frac{\partial^2 u}{\partial t^2}-\frac{\gamma P_0}{\rho_0}\frac{\partial^2 u}{\partial x^2}=0\,. \tag{4.8}$$

Through combinations of Eqs. (4.5-4.7) we find that the other two perturbed quantities (ρ and P) follow the same differential equation. Therefore, all three variables f satisfy the differential equation

$$\frac{\partial^2 f}{\partial t^2}-c_s^2\frac{\partial^2 f}{\partial x^2}=0\,, \tag{4.9}$$

with

$$c_s\equiv\sqrt{\frac{\gamma P_0}{\rho_0}}\,. \tag{4.10}$$

Eq. (4.9) allows any solution of the form $f(x-c_st)$ or $f(x+c_st)$ (or linear combinations of these two forms), corresponding to waves travelling in the $-x$ or $+x$ directions (respectively). These waves travel at the sound speed c_s, defined by Eq. (4.10).

4.3 Isothermal sound waves

In ISM flows, it is common to assume that the flow is approximately isothermal. This is a reasonable approximation, e. g., for flows within H II regions in which the rapid heating/cooling processes tend to fix the temperature at a value $T_0 \approx 10^4$ K. In order to model sound waves in such an environment, one uses the linearized continuity and momentum equations (Eqs. 4.5-4.6), and replaces the energy equation with the condition

$$P = \rho \frac{RT_0}{\mu}\,, \tag{4.11}$$

where R is the gas constant and μ the molecular weight.

The solution of this system of equations corresponds to waves that travel at a velocity

$$c_{is} = \sqrt{\frac{RT_0}{\mu}} = \sqrt{\frac{P_0}{\rho_0}}\,. \tag{4.12}$$

This is called the "isotheral sound speed", which coincides with the "adiabatic" sound speed (see Eq. 4.10) evaluated for a $\gamma = 1$ specific heat ratio.

Chapter 5

Shock waves

5.1 General considerations

As in general astrophysical flows range from transonic to hypersonic conditions, an understanding of shock waves is essential. Shock waves are generally produced in supersonic flows.

For example, in Fig. 5.1 we show a numerical simulation of the steady flow pressure stratification produced by a blunt bullet moving at a $M = 30$ Mach number within a uniform, $\gamma = 7/5$ medium. It is clear that the pressure shows two surfaces with discontinuous pressure increases. These two shock waves are called the "bow shock" and the "tail shock".

Many astrophysical flows produce directly observable shock waves. Notable examples are jets (from stars or from massive compact objects) and supernovae.

5.2 Plane-parallel shock waves

Let us now consider the simplest possible shock wave problem : a plane shock wave moving along the direction normal to the plane wave front. If we consider a coordinate system moving with the shock wave, with the x-axis pointing towards the post-shock direction, we have the situation shown in Fig. 5.2.

The transition from the pre-shock flow variables (ρ_0, u_0 and P_0, see Fig. 5.2) to the post-shock variables (ρ_1, u_1 and P_1) occurs over distances comparable to the mean free path λ of the particles in the gas. Therefore, the

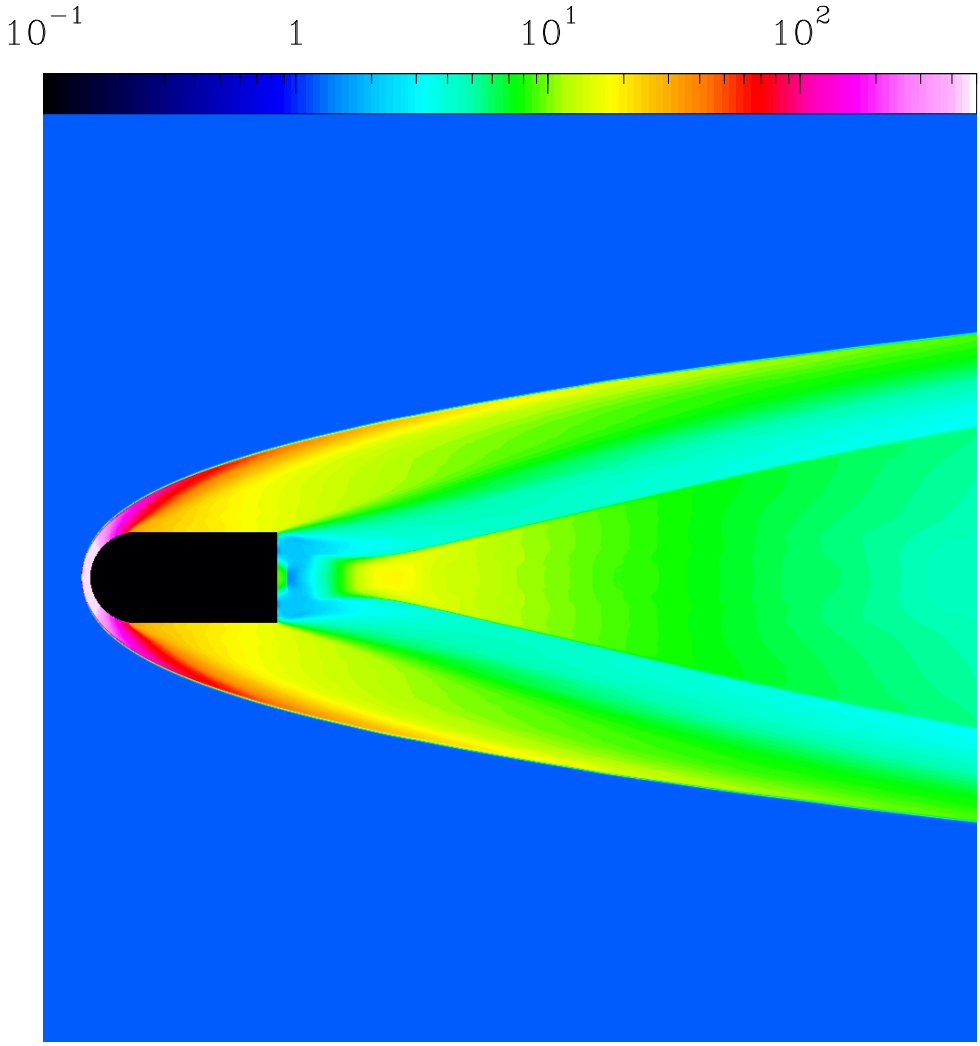

Figure 5.1: Pressure stratification in a blunt bullet flow moving at $M = 30$ in a $\gamma = 7/5$ gas, well into the hypersonic regime.

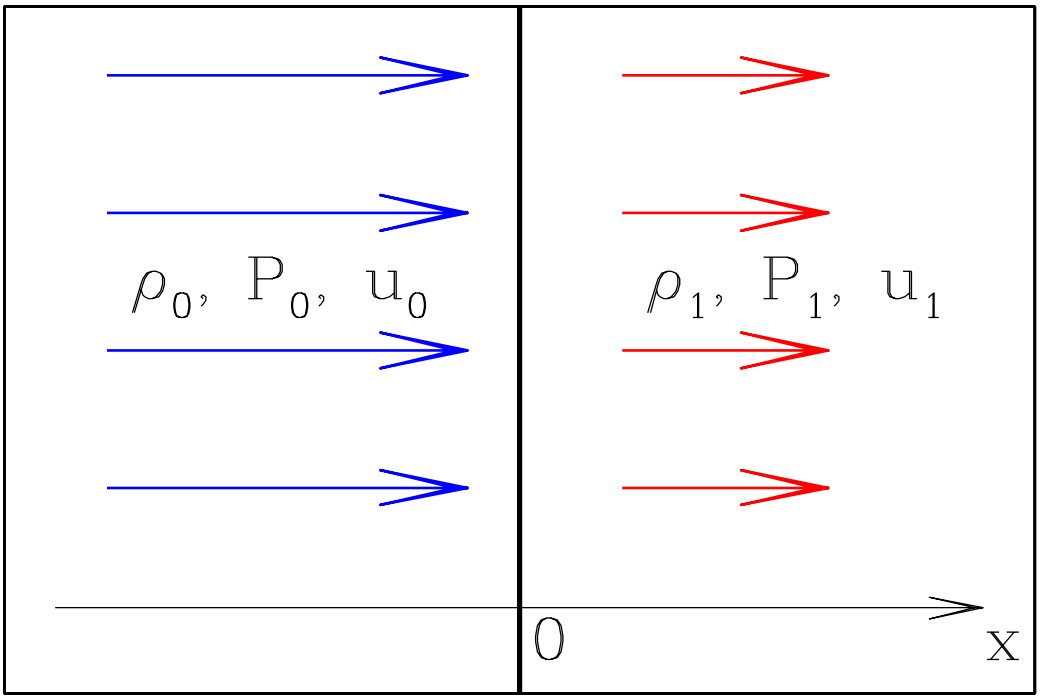

Figure 5.2: Schematic diagram of a plane-parallel shock.

transition is generally not appropriately described by the gasdynamic equations, and a kinetic approach has to be used.

Because shock waves correspond to discontinuous solutions of the gasdynamic equations, the mass, momentum and energy gasdynamic equations (Eqs. 3.35-3.37) do give the appropriate relations between the pre- and post-shock variables. However, a description of the details of the transition lie beyond a gasdynamic description.

In the reference system moving with the shock wave (see Fig. 5.2) the problem has no time-dependence. Hence, the 1D gasdynamic equations simplify to : $\rho u = const.$, $\rho u^2 + P = const.$, $u(E + P) = const.$ (with $E = \rho u^2/2 + P/(\gamma - 1)$), where we have assumed that the energy loss/gain within the shock transition is negligible. Therefore, the pre- and post-shock variables follow the relations :

$$\rho_0 u_0 = \rho_1 u_1 \,, \tag{5.1}$$

$$\rho_0 u_0^2 + P_0 = \rho_1 u_1^1 + P_1 \,, \tag{5.2}$$

$$u_0 \left(\frac{\rho_0 u_0^2}{2} + \frac{\gamma P_0}{\gamma - 1} \right) = u_1 \left(\frac{\rho_1 u_1^2}{2} + \frac{\gamma P_1}{\gamma - 1} \right) . \tag{5.3}$$

From these equations, we can find the postshock variables (ρ_1, u_1 and P_1) as a function of the preshock variables (ρ_0, u_0 and P_0)

In order to do this, we first combine Eqs. (5.1-5.2) to obtain :

$$P_1 = P_0 + \rho_0 u_0^2 \left(1 - \frac{\rho_0}{\rho_1} \right) . \tag{5.4}$$

Substituting u_1 (from Eq. 5.1) and P_1 (from Eq. 5.4) into Eq. (5.3), we obtain a quadratic equation for ρ_1/ρ_0 :

$$\left(\frac{\rho_1}{\rho_0} \right)^2 \left[\frac{(\gamma - 1)M_0^2}{2} + 1 \right] - \left(\frac{\rho_1}{\rho_0} \right) \left(\gamma M_0^2 + 1 \right) + \frac{(\gamma + 1)M_0^2}{2} = 0 \,, \tag{5.5}$$

where $M_0 = u_0/c_0$, with $c_0 \sqrt{\gamma P_0/\rho_0}$. This equation has solutions

$$\frac{\rho_1}{\rho_0} = \frac{\gamma M_0^2 + 1 \pm \sqrt{(M_0 - 1)^2}}{(\gamma - 1)M_0^2 + 2} \,, \tag{5.6}$$

giving $\rho_1/\rho_0 = 1$ for the "$-$" sign, and giving the compression at a shock wave for the "+" sign :

$$\frac{\rho_1}{\rho_0} = \frac{(\gamma + 1)M_0^2}{(\gamma - 1)M_0^2 + 2} \,. \tag{5.7}$$

Combining Eqs. (5.7) and (5.1) we then obtain

$$\frac{u_1}{u_0} = \frac{(\gamma-1)M_0^2+2}{(\gamma+1)M_0^2} \quad \left(= \frac{\rho_0}{\rho_1}\right), \tag{5.8}$$

and using Eq. (5.4) we finally obtain :

$$P_1 = P_0 + \frac{2(M_0^2-1)}{(\gamma+1)M_0^2}\rho_0 u_0^2 \,. \tag{5.9}$$

Eqs. (5.7-5.9) are called the "shock jump relations" (alternatively, the "Rankine-Hugoniot" or just "Hugoniot" relations).

For $M_0 = u_0/c_0 \gg 1$, we obtain the so-called "strong shock" jump relations :

$$\frac{\rho_1}{\rho_0} = \frac{u_0}{u_1} = \frac{\gamma+1}{\gamma-1}\,, \tag{5.10}$$

$$P_1 = \frac{2}{\gamma+1}\rho_0 u_0^2 \,. \tag{5.11}$$

As in most cases ISM shocks are indeed hypersonic (i. e., with $M_0 \gg 1$), these strong shock relations are applicable in most of the problems that will be covered in this book.

5.3 Shock with radiative cooling

From the strong shock jump conditions (Eqs. 5.10-5.11), we see that the post-shock temperatre T_1 is given by :

$$T_1 = \frac{P_1 \mu m_H}{k\rho_1} = \frac{2(\gamma-1)}{(\gamma+1)^2}\frac{\mu m_H u_0^2}{k} = 1.13\times10^5\,\mathrm{K}\,\left(\frac{u_0}{100\,\mathrm{km\,s^{-1}}}\right)^2 , \tag{5.12}$$

where k is Boltzmann's constant, μ is the molecular weight of the gas and m_H is the mass of H. The third term of the equation was calculated assuming $\gamma = 5/3$ and $\mu = 1/2$ (appropriate for a fully ionized, H gas). We have normalized the relation to a typical $u_0 = 100$ km s^{-1} velocity for a shock in a SNR or in a HH object.

This hot gas cools, emitting radiation at IR, optical and UV wavelengths to a temperature of a few thousand K. So, we assume that the cooling region ends when the gas has attained a temperature $T_2 \sim 10^3$ K. At this point, the

gas has recombined, and has an isothermal sound speed $c_2 = \sqrt{kT_2/\mu m_H} \sim 3$ km s^{-1}.

We can then use the mass and momentum conservation equations (Eqs. 5.1-5.2) to determine the value of ρ_2 after the cooling region. Combining these two equations, we obtain the quadratic equation

$$\rho_2 c_2^2 - \rho_2 \left(u_0^2 + P_0\right) + \rho_0^2 u_0^2 = 0\,, \tag{5.13}$$

which has the shock solution :

$$\frac{\rho_2}{\rho_0} = \frac{c_0^2}{2c_2^2}\left[M_0^2 + 1 + \sqrt{M_0^4 + 2M_0^2(1-2\alpha)+1}\right]\,, \tag{5.14}$$

where $M_0 = u_0/c_0$ and $\alpha = (c_2/c_0)^2$, with c_0 and c_2 being the pre-shock and post-cooling region isothermal sound speeds (respectively).

The strong shock relation (obtained for $M_0 \gg 1$) then is :

$$\frac{\rho_2}{\rho_0} = \left(\frac{u_0}{c_2}\right)^2\,. \tag{5.15}$$

In other words, the compression is equal to the square of the Mach number $M_0' = u_0/c_2$ computed with the pre-shock velocity and the post-cooling region sound speed.

For the case in which $c_2 = c_0$, we obtain :

$$\frac{\rho_2}{\rho_0} = M_0^2\,. \tag{5.16}$$

This is called the "isothermal shock" jump relation, and is valid for all Mach numbers.

5.4 Oblique shock jump relations

Let us now consider a plane, oblique shock. In such a shock, the flow enters the shock at an angle different from $\pi/2$, and is refracted at its passage through the shock. This is shown schematically in Fig. 5.3.

Let us consider a cartesian coordinate system at rest with the shock, with its x-axis pointing along the normal to the plane shock (towards the post-shock region) and its y-axis in the plane that contains the normal to the

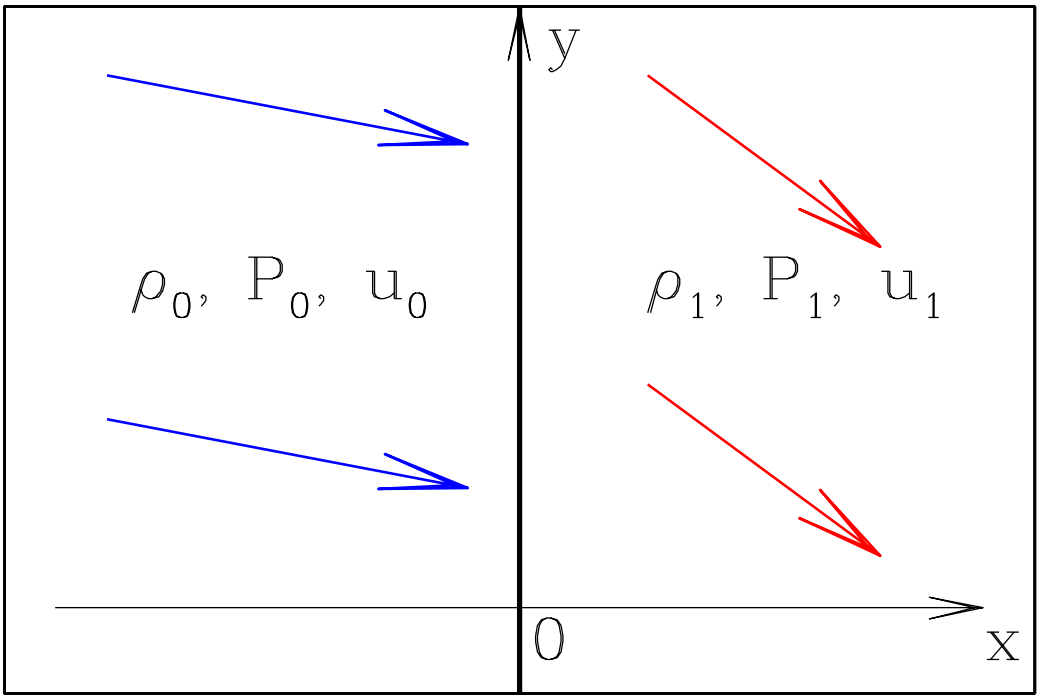

Figure 5.3: Schematic diagram of a plane, oblique shock.

shock and the pre-shock velocity $\underline{u}_0$. From simple symmetry arguments it is clear that the post-shock velocity $\underline{u}_1$ will also lie on the xy-plane.

We then write the steady, 2D Euler equations (see Eqs. 3.27-3.30) with no y-dependence :

$$\frac{\partial}{\partial x}\left(\rho u_n\right) = 0\,, \tag{5.17}$$

$$\frac{\partial}{\partial x}\left(\rho u_n^2 + P\right) = 0\,, \tag{5.18}$$

$$\frac{\partial}{\partial x}\left(\rho u_n u_t\right) = 0\,, \tag{5.19}$$

$$\frac{\partial}{\partial x}\left\{u_n\left[\frac{\rho}{2}\left(u_n^2+u_t^2\right)+\frac{\gamma P}{\gamma-1}\right]\right\} = 0\,, \tag{5.20}$$

where u_n and u_t are the components of the flow velocity parallel to the x- and y-axes, respectively (see Fig. 5.3).

From these equations, we can obtain the relations that have to be satisfied between the pre-shock variables (ρ_0, $u_{n,0}$, $u_{t,0}$ and P_0), and the post-shock variables (ρ_1, $u_{n,1}$, $u_{t,1}$ and P_1) :

$$\rho_0 u_{n,0} = \rho_1 u_{n,1}\,, \tag{5.21}$$

$$\rho_0 u_{n,0}^2 + P_0 = \rho_1 u_{n,1}^2 + P_1\,, \tag{5.22}$$

$$\rho_0 u_{n,0} u_{t,0} = \rho_1 u_{n,1} u_{t,1}\,, \tag{5.23}$$

$$u_{n,0}\left[\frac{\rho_0}{2}\left(u_{n,0}^2+u_{t,0}^2\right)+\frac{\gamma P_0}{\gamma-1}\right] = u_{n,1}\left[\frac{\rho_1}{2}\left(u_{1,0}^2+u_{t,1}^2\right)+\frac{\gamma P_1}{\gamma-1}\right]\,. \tag{5.24}$$

Eqs. (5.21) and (5.23) can be combined to give the jump condition for the tangential velocity :

$$u_{t,1} = u_{t,0}\,, \tag{5.25}$$

in other words, the component of the velocity parallel to the shock wave is preserved when going through the shock.

Now, combining Eqs. (5.21), (5.24) and (5.25), we obtain an energy equation involving only the normal component of the flow velocity :

$$\frac{u_{n,0}^2}{2} + \frac{\gamma}{\gamma-1}\frac{P_0}{\rho_0} = \frac{u_{n,1}^2}{2} + \frac{\gamma}{\gamma-1}\frac{P_1}{\rho_1}\,. \tag{5.26}$$

It is clear that Eqs. (5.21), (5.22) and (5.23) are the same equation system as the one for a plane-parallel shock (Eqs. 5.1-5.3, with Eq. 5.26 actually

being the ratio between Eqs. 5.1 and 5.3). Therefore, the compression and the post-shock pressure are given by Eqs. (5.7) and (5.9) :

$$\frac{\rho_1}{\rho_0} = \frac{u_{n,0}}{u_{n,1}} = \frac{(\gamma+1)M_{n,0}^2}{(\gamma-1)M_{n,0}^2+2}\,, \tag{5.27}$$

$$P_1 = P_0 + \frac{2(M_{n,0}^2-1)}{(\gamma+1)M_{n,0}^2}\rho_0 u_{n,0}^2\,, \tag{5.28}$$

but with $u_{n,0}$ instead of u_0, and the pre-shock Mach number being replaced with the Mach number $M_{n,0} = u_{n,0}/c_0$ associated with the normal component of the pre-shock velocity.

In the case of a radiative shock, Eqs. (5.27-5.28) would have to be replaced with the appropriate jump conditions, obtained by replacing the pre-shock flow velocity u_0 by $u_{n,0}$.

5.5 Examples of flows with plane shock fronts

5.5.1 Flow colliding normally with a rigid wall

Let us consider the problem of a plane, supersonic wind (of density ρ_w, pressure P_w and velocty v_w) hitting a rigid wall (oriented perpendicular to the direction of the wind velocity). The physical situation is shown in Fig. 5.4.

A shock is formed initially against the wall, and this shock then travels (at a velocity v_s, see Fig. 5.4) in the upstream direction, forming a post-shock region in which the gas is at rest with respect to the wall. In a reference frame moving with the shock, we have a medium with pre-shock flow parameters $\rho_0 = \rho_w$, $P_0 = P_w$ and $u_0 = v_w + v_s$. The fact that the post-shock flow is at rest with respect to the wall implies that $u_1 = v_s$.

Using Eq. (5.8), we have that

$$\frac{v_w+v_s}{v_s} = \frac{\gamma+1}{\gamma-1+\frac{2c_0^2}{(v_w+v_s)^2}}\,, \tag{5.29}$$

where $c_0 = \sqrt{\gamma P_0/\rho_0}$ is the pre-shock sound speed. From this equation, we can derive a quadratic equation for v_s :

$$2v_s^2 + v_s v_w(3-\gamma) - 2c_0^2 - (\gamma-1)v_w^2 = 0\,, \tag{5.30}$$

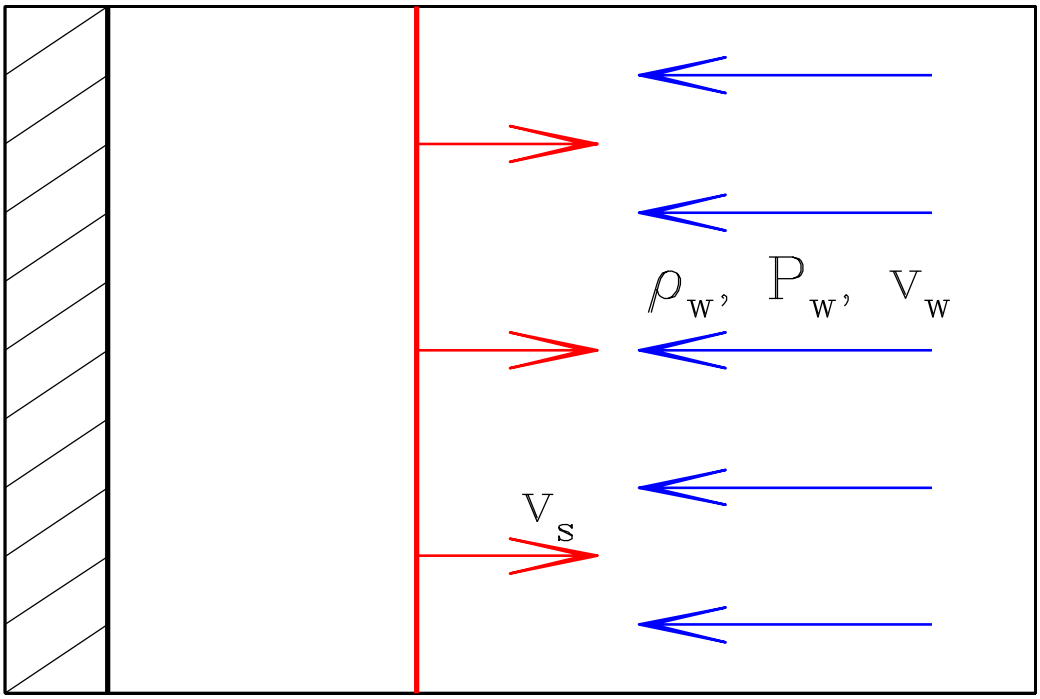

Figure 5.4: Schematic diagram of a flow constituted by a supersonic wind which collides with a solid wall (perpendicular to the direction of the flow).

which has the solution

$$\frac{v_s}{v_w} = \frac{1}{4}\left[\gamma - 3 + \sqrt{(\gamma+1)^2 + 16(c_0/v_w)^2}\right] , \tag{5.31}$$

which in the hypersonic regime ($v_w \gg c_0$) gives

$$\frac{v_s}{v_w} = \frac{\gamma - 1}{2} . \tag{5.32}$$

5.5.2 Flow hitting a wedge

Let us consider the problem of a supersonic flow which hits the leading edge of a rigid wedge. If the wedge has a small enough half-opening angle ϕ, a "regular shock reflection" occurs. In this configuration, two plane shocks (which are attached to the leading edge) redirect the incoming flow to directions parallel to the two plane surfaces of the wedge (see the top frame of Fig. 5.5). For large enough values of ϕ, instead of a regular shock reflection, a detached bow shock is formed (right frame of Fig. 5.5).

The regular reflection regime has a simple analytic solution. For deriving this solution, we consider one of the two sides of the flow/wedge interaction, as shown in Fig. 5.6. We have a flow which hits the surface of a plane "shelf" (at an angle ϕ to the surface), and an oblique shock (at an angle α to the surface) redirects the incoming flow to a direction parallel to the shelf.

From Fig. 5.6 it is clear that the pre-shock flow (of velocity u_0) has components $u_{n,0}$ and $u_{t,0}$ normal and parallel (respectively) to the shock given by :

$$u_{n,0} = u_0 \sin(\phi + \alpha) ; \quad u_{t,0} = u_0 \cos(\phi + \alpha) . \tag{5.33}$$

From the oblique shock jump conditions, the post-shock flow velocity then has the normal and tangential components :

$$u_{n,1} = \frac{u_{n,0}}{\xi} ; \quad u_{t,1} = u_{t,0} , \tag{5.34}$$

where ξ is the compression at the shock. If the shock is strong, we have

$$\xi = \frac{\gamma + 1}{\gamma - 1} . \tag{5.35}$$

The post-shock flow is parallel to the surface of the shelf. Therefore, the component v_{surf} normal to the shelf of the post-shock flow has to be zero :

$$v_{surf} = u_{t,1} \sin\alpha - u_{n,1} \cos\alpha = 0 . \tag{5.36}$$

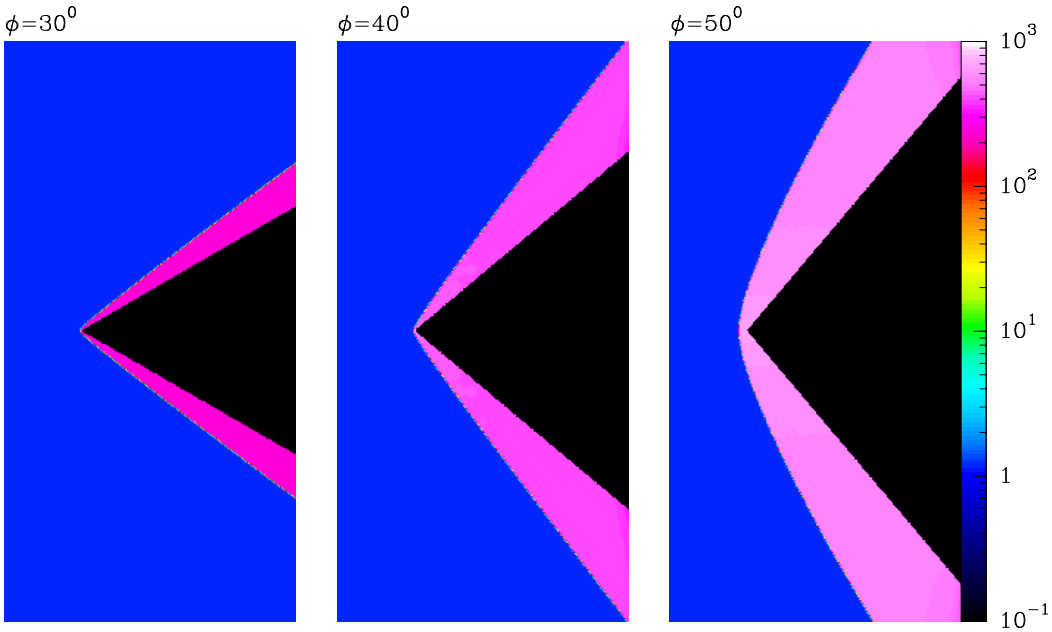

Figure 5.5: Pressure stratifications resulting from the interaction of a $M = 30$, $\gamma = 7/5$ flow (propagating to the right, along the abscissa) with a rigid wedge. The three plots are labeled with the half-opening angle of the wedges. The $\phi = 30°$ and $\phi = 40°$ flows are stationary. The flow obtained for the $\phi = 50°$ wedge (right frame) is non-stationary, and the displayed stratification corresponds to a time evolution equal to 3 times the flow crossing time scale of the abscissa of the displayed domain.

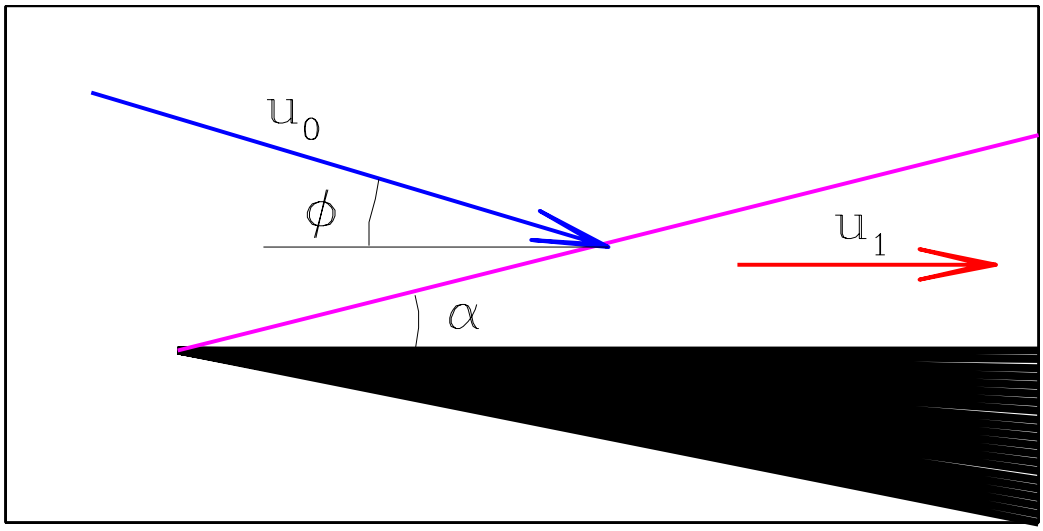

Figure 5.6: Schematic diagram showing the interaction of a flow that hits a plane, solid shelf (in black) at an angle ϕ to its surface. A regular reflection is produced, with an oblique shock (at an angle α) that redirects the flow to a direction parallel to the surface of the shelf.

Combining Eqs. (5.33), (5.34) and (5.36) we then obtain :

$$\tan(\alpha+\phi) = \xi \tan\alpha\,. \tag{5.37}$$

This is the equation that determines the angle α (between the shock and the shelf) as a function of the incidence angle ϕ (see Fig. 5.6) and the compression ξ at the shock.

Using the identity

$$\tan(\alpha+\phi) = \frac{\tan\alpha+\tan\phi}{1-\tan\alpha\tan\phi}\,, \tag{5.38}$$

we can rewrite Eq. (5.37) in the form

$$\xi\tan^2\alpha + \frac{1-\xi}{\tan\phi}\tan\alpha + 1 = 0\,. \tag{5.39}$$

This quadratic equation has solutions

$$\tan\alpha = \frac{\xi-1}{2\xi\tan\phi}\left[1 \pm \sqrt{1-\frac{4\xi\tan^2\phi}{(\xi-1)^2}}\right]\,. \tag{5.40}$$

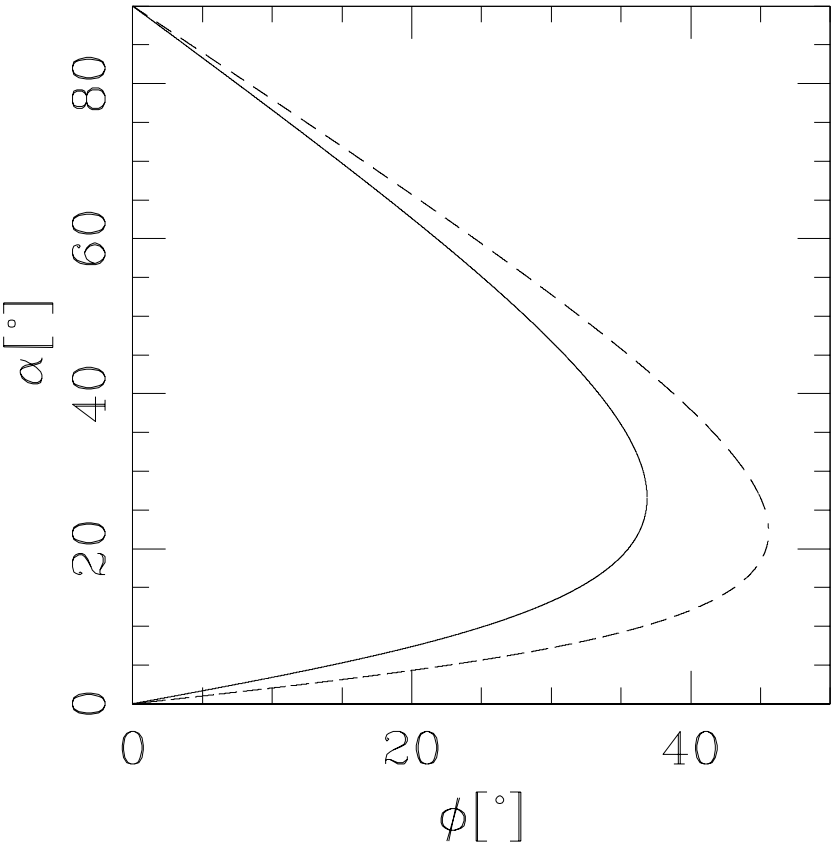

Figure 5.7: Angle α between the shock and the plane surface (in the regular shock reflection problem) as a function of the incidence angle ϕ for a hypersonic flow with $\gamma = 5/3$ (solid line) and $\gamma = 7/5$ (dashed line).

The α vs. ϕ relations obtained (from Eq. 5.40) for strong shocks with $\gamma = 5/3$ ($\rightarrow \xi = 4$) and $\gamma = 7/5$ ($\rightarrow \xi = 6$) are shown in Fig. 5.7.

In this figure, we see that for a given ϕ there are two possible values of α (obtained from the $+/-$ sign of Eq. 5.40). These are called the "strong" (larger α value) and the "weak" solutions. It is an experimental fact that regular reflections invariably adopt the weak solution. Numerical solutions of this problem (see Fig. 5.5) also adopt the weak solution.

From Fig. 5.7 it is clear that there is a maximum possible value ϕ_{max} beyond which there are no solutions to the regular shock reflection problem. The value of ϕ_{max} is obtained by setting the square root term of Eq. (5.40)

to zero, which gives

$$\tan \phi_{max} = \frac{\xi - 1}{2\sqrt{\xi}} \,. \tag{5.41}$$

Combining this equation with the strong shock jump condition (Eq. 5.35), we obtain $\phi_{max} = 36°.87$ for $\gamma = 5/3$ and $\phi_{max} = 45°.58$ for $\gamma = 7/5$.

For incidence angles of the flow $\phi > \phi_{max}$ a regular shock reflection is not possible, and the "flow on wedge" problem then adopts a solution with a curved bow shock (see the right frame of Fig. 5.5). There is no analytic solution for this flow configuration.

Chapter 6

1D, stationary, radiative shocks

6.1 General considerations

After the passage of an astrophysical shock wave, the hot, post-shock gas emits radiation and cools again. Provided that the shock velocity is high enough, the post-shock gas becomes rapidly ionised, and then emits a rich emission line spectrum. This radiative energy loss cools the gas, and the ions recombine to lower ionisation states.

The most simple possible model for this post-shock relaxation region is to consider a stationary, plane-parallel flow. The plane-parallel approximation is valid provided that the size of the relaxation region is small compared to the radius of curvature of the shock wave (a condition not necessarily met in ISM shock waves). The assumption that the flow is stationary is also dubious at best, since many objects have evolutionary timescales which are comparable to the post-shock cooling timescale. Also, it has been found that the relaxation regions behind shock waves of high enough velocities (> 100 km s^{-1}) are thermally unstable, so that the stationary solutions are probably never attained by a real shock.

Regardless of these problems, the plane-parallel, stationary radiative shock is the most simple possible problem with direct application to ISM shocks from which a concrete prediction of the emitted spectrum can be made. It serves as an illustration of the elements that have to be considered when trying to model more complex flows with shock waves in the ISM.

6.2 The equations for the recombination region

From the 1D Euler equations (Eqs. 3.35-3.37), we see that a radiative plane-parallel, stationary, $\gamma = 5/3$ flow (in the absence of external forces) satisfies the equations

$$\rho u = \rho_0 u_0 \,, \tag{6.1}$$

$$\rho u^2 + P = \rho_0 u_0^2 + P_0 \,, \tag{6.2}$$

$$\frac{dh}{dx} = \frac{G - L}{\rho u} \,; \quad h = \frac{u^2}{2} + \frac{5}{2}\frac{P}{\rho} \,, \tag{6.3}$$

where ρ_0, P_0 and u_0 are the flow variables at some point in which they are known (in our case, these would be the pre-shock conditions), and G, L are the energy gain and loss (respectively) per unit volume and time.

The procedure for calculating the structure of the recombination region is to integrate numerically Eq. (6.3) over a finite distance step Δx, going from $h(x)$ to $h(x + \Delta x)$, and then to use the relations

$$\rho = \frac{(5/2)(P_0 + \rho_0 u_0^2) + \sqrt{(5/2)^2 (P_0 + \rho_0 u_0^2)^2 - 8h\rho_0^2 u_0^2}}{2h} \,, \tag{6.4}$$

$$P = P_0 + \rho_0 u_0^2 \left(1 - \frac{\rho_0}{\rho}\right) \,, \tag{6.5}$$

$$u = \frac{\rho_0 u_0}{\rho} \,, \tag{6.6}$$

(which can be deduced from Eqs. 6.1-6.3) to calculate the flow variables ρ, P and u as a function of the "advanced position" specific enthalpy $h(x + \Delta x)$ and the pre-shock variables ρ_0, P_0 and u_0. From the flow variables one can then calculate

$$n = \frac{\rho}{\overline{m}} \,; \quad T = \frac{P}{k(n + n_e)} \,, \tag{6.7}$$

where n is the ion+atom number density, n_e the electron density, and $\overline{m}$ is the average mass per atom or ion ($\overline{m} = m_H$ for a pure H gas, and $\overline{m} = 1.3 m_H$ for a 90% H and 10% He gas).

Before actually being able to integrate Eq. (6.3) it is actually necessary to calculate what is the ionisation state of the gas. This is necessary in order to calculate n_e (see Eq. 6.7) and to calculate the heating and cooling functions (G and L, respectively).

6.3 The ionisation state of the gas

If the gas were in coronal ionisation equilibrium, we could compute the ionisation state of the gas as a function of the local temperature. Unfortunately, in the cooling region behind a shock wave the cooling and recombination timescales are comparable, so that the gas is actually not in ionisation equilibrium. Because of this, it is necessary to integrate the rate equations

$$u\frac{dy_{a,z}}{dx} = n_e \left\{ y_{a,z+1}\alpha_{a,z+1}(T) + y_{a,z-1}c_{a,z-1}(T) - y_{a.z}\left[\alpha_{a,z}(T) + c_{a,z}(T)\right]\right\} +$$

$$y_{a,z-1}\phi_{a,z-1} - y_{a,z}\phi_{a,z}\,, \tag{6.8}$$

where $y_{a,z} = n_{a,z}/n_a$ is the fractional ionisation state of the ion of charge z of the element a, and the α, c and ϕ coefficients are the recombination, collisional ionisation and photoionisation rates (respectively). We also have the auxilliary relations :

$$\sum_z y_{a,z} = 1\,, \tag{6.9}$$

$$\sum_a \left[n_a \sum_z y_{a,z} \right] = n\,, \tag{6.10}$$

$$\sum_a \left[n_a \sum_z z y_{a,z} \right] = n_e\,, \tag{6.11}$$

$$\frac{1}{n}\sum_a n_a m_a = \overline{m}\,, \tag{6.12}$$

$$n_a = f_a\, n\,, \tag{6.13}$$

where m_a is the mass and f_a the abundance (by number) of element a.

This then represents the main difficulty in computing the structure of the relaxation region behind an astrophysical shock wave. In order to compute the ionisation state of the gas (necessary for computing the electron density n_e and the heating and cooling functions) it is necessary to integrate a set of rate equations (see Eq. 6.8) including all of the relevant ions together with the equation for the specific enthalpy (Eq. 6.3).

6.4 The photoionisation rates

The main difficulty in computing the ionisation rate equations (Eqs. 6.8) is naturally related to the photoionisation rates

$$\phi_{a,z} = \int_{\nu_{a,z}}^{\infty} \frac{4\pi J_\nu}{h\nu} a_\nu^{a,z} d\nu \,, \tag{6.14}$$

where $\nu_{a,z}$ is the frequency associated with the ground state ionisation edge and $a_\nu^{a,z}$ the photionisation cross section of ion a, z.

The intensity I_ν is obtained through an integration of the plane-parallel radiative transfer equation :

$$\mu \frac{dI_\nu}{dx} = j_\nu - \kappa_\nu I_\nu \,, \tag{6.15}$$

where the emission coefficient j_ν is dominated by the contribution from the H Lyman continuum, but also has contributions from the He II and He III recombination continua, and from resonance lines of a limited set of ions (see, e. g., the paper of Shull and McKee 1979). In Eq. (6.15), $\mu = \cos\theta$ where θ is the angle between the propagation direction of the ray and the x-axis.

The radiative transfer equation (Eq. 6.15) has the integral form (for $\mu > 0$) :

$$I_\nu(x, \mu) = \frac{1}{\mu} \int_{-\infty}^{x} j_\nu(x') e^{-\tau_\nu(x', x)/\mu} dx' \,, \tag{6.16}$$

where

$$\tau_\nu(x', x) = \int_{x'}^{x} \kappa_\nu(x'') dx'' \,. \tag{6.17}$$

A similar expression (but with integration limits from $+\infty$ to x) is obtained for directions with $\mu < 0$. The average intensity J_ν can then be computed as :

$$J_\nu(x) = \frac{1}{4\pi} \oint I_\nu \, d\omega = \frac{1}{2} \int_{-1}^{1} I_\nu(x, \mu) d\mu \,. \tag{6.18}$$

Combining Eqs. (6.16-6.18) and commuting the position and angular integrals, we finally obtain :

$$J_\nu(x) = \frac{1}{2} \int_0^{\infty} j_\nu(x') E_1 \left[|\tau_\nu(x', x)| \right] \, dx' \,, \tag{6.19}$$

where the first order exponential integral $E_1(\tau)$ is defined by

$$E_1(\tau) \equiv \int_\tau^\infty \frac{e^{-t}}{t} dt = \int_0^1 \frac{e^{-\tau/\mu}}{\mu} d\mu \,. \tag{6.20}$$

Tabulations and rational/exponential approximations to $E_1(\tau)$ can be found in the book of Abramowitz & Stegun (1965).

Therefore, in order to calculate the photoionisation rates it is necessary to compute the average intensity J_ν at all positions x along the flow (Eqs. 6.17, 6.19 and 6.20) at least for a limited number of frequency values. For example, one finds in the literature numerical models that use a set of frequencies coinciding with the ionisation edges of all of the ions considered in the calculation.

In numerical integrations of the plane-parallel, radiative shock problem it is found that in general the photoionisation rates do not play a dominant role. Therefore, approximate solutions of the post-shock region can be obtained neglecting the photoionisation rates in the ionisation rate equations (Eqs. 6.8). Including the photoionisation rates forces one to do a more complex numerical solution, involving an iterative procedure.

6.5 The minimal relaxation region model

Let us now consider a very simple model for the post-shock relaxation region. In our model, we consider Eqs. (6.3-6.7), and write a single equation for the ionisation fraction $y = n_{HII}/n_H$ of Hydrogen :

$$\frac{dy}{dx} = \frac{ny}{u} \left[(1-y)c(T) - y\alpha(T) \right] , \tag{6.21}$$

with the interpolation functions given after Eq. (1.56) for the $\alpha(T)$ and $c(T)$ coefficients. In this equation we have set $n_e = yn$, $n_{HII} = yn$ and $n_{HI} = (1-y)n$, with $n = \rho/\overline{m}$ (with $\overline{m} \approx m_H$).

We now set $G = 0$ (we neglect the energy gain due to photoionisation, consistently with the fact that we have neglected the photoionistion rates in Eq. 6.21) and compute L as :

$$L = n^2 y(1-y)c(T)\chi_H + n^2 y \left(6.1 \times 10^{-19}\right) \left[1 - e^{-(T/10^5)^{1.63}} \right] , \tag{6.22}$$

where the first term on the right is the cooling due to collisional ionisation of H (with $\chi_H = 13.6$ eV) and the second term is an analytic approximation

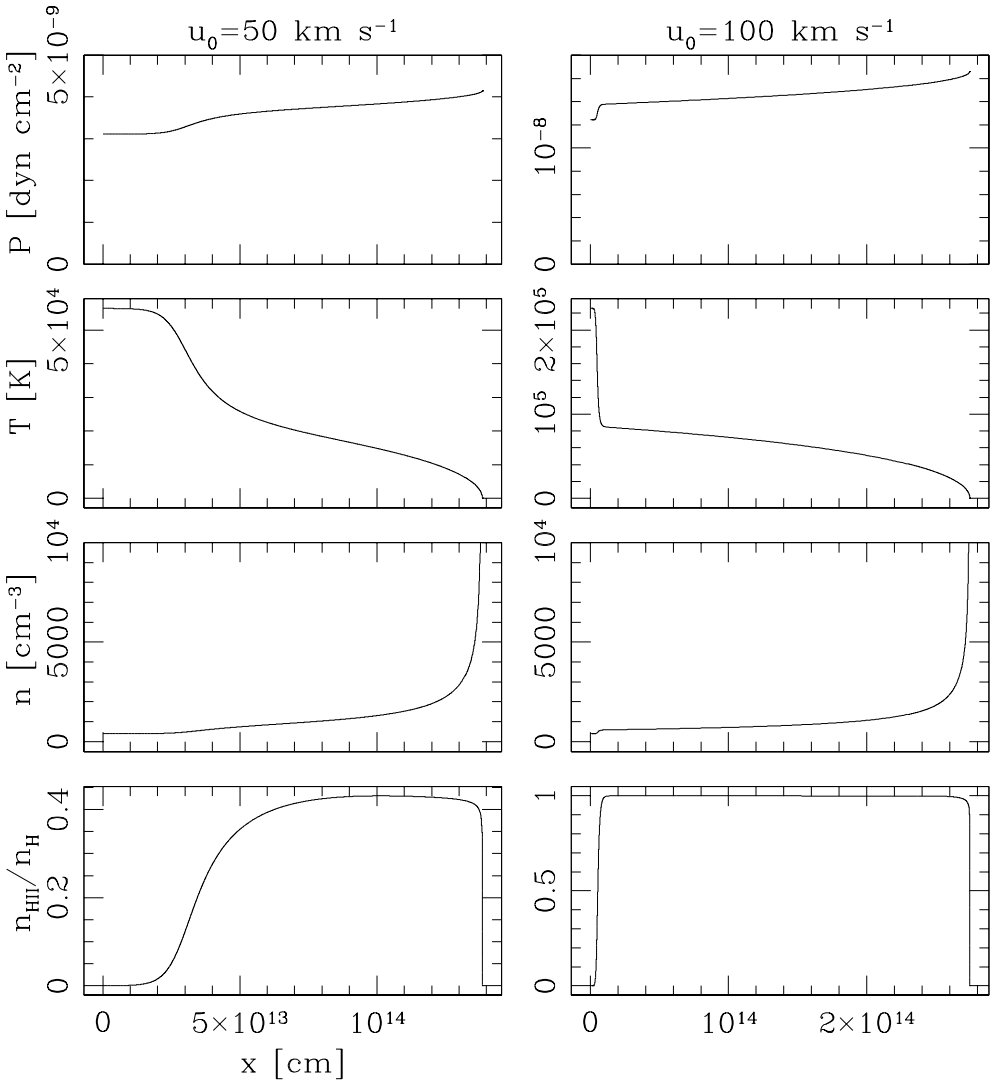

Figure 6.1: Structures of the relaxation region behind a shock wave computed from the "minimal model" described in the text.

to the temperature behaviour of the coronal ionisation cooling function (all variables are in cgs units).

We now choose a set of pre-shock parameters : u_0, T_0, n_0 and y_0, and numerically integrate Eqs. (6.3) and (6.21) until the gas recombines and reaches low temperatures. Results of this exercise obtained for $T_0 = 100$ K, $n_0 = 100$ cm^{-3}, $y_0 = 10^{-4}$ and $u_0 = 50$, 100 km s^{-1} are shown in Fig. 6.1.

These solutions show the typical stratification of the post-shock relaxation region : a region close to the shock wave in which the gas gets collisionally ionised, followed by a more extended, cooler region in which H eventually recombines again. This latter region is called the "recombination" or "cooling" region. There is an abundant literature on solutions of this type, of which Hartigan et al. (1987) is a standard reference.

6.6 The cooling distance

From models of the relaxation region behind a plane-parallel shock it is possible to calculate a "cooling distance" d_c. We define d_c as the distance from the shock to the point where the temperature has dropped to a value of 10^4 K. It is also possible to choose another value for this temperature (e. g., 10^3 K), but it is clear from Fig. 6.1 that similar values for d_c are obtained regardless of the precise temperature value that has been chosen.

Fig. 6.2 shows the cooling distance (to 10^4 K) as a function of shock velocity u_0, for a pre-shock number density $n_0 = 100$ km s^{-1}, obtained from the shock model tabulation of Hartigan et al. (1987). In order to obtain the scaling of the cooling distance with pre-shock density, we consider the following scaling argument. The cooling distance d_c can be estimated as :

$$d_c \sim \frac{E_{T,1}}{L_1} u_1 \propto \frac{n_1 k T_1 u_1}{n_1^2 \Lambda(T_1)} \propto \frac{f(u_0)}{n_0} \,. \tag{6.23}$$

In other words, the cooling distance is given by the ratio between the post-shock thermal energy ($E_{T,1}$) and cooling function ($L_1 = n_1^2 \Lambda(T_1)$, assuming low density regime cooling) multiplyed by the post-shock velocity u_1. Given the fact that for a strong shock, the post-shock velocity is $u_1 = u_0/4$, the post-shock density is $n_1 = 4n_0$ (Eqs. 5.6 and 5.8), and the post-shock temperature T_1 is a function of the pre-shock velocity u_0 (Eq. 5.12).

Therefore, provided that the cooling function is in the low density regime (i. e., $L = n^2 \Lambda(T)$), the cooling distance is proportional to the ratio of a

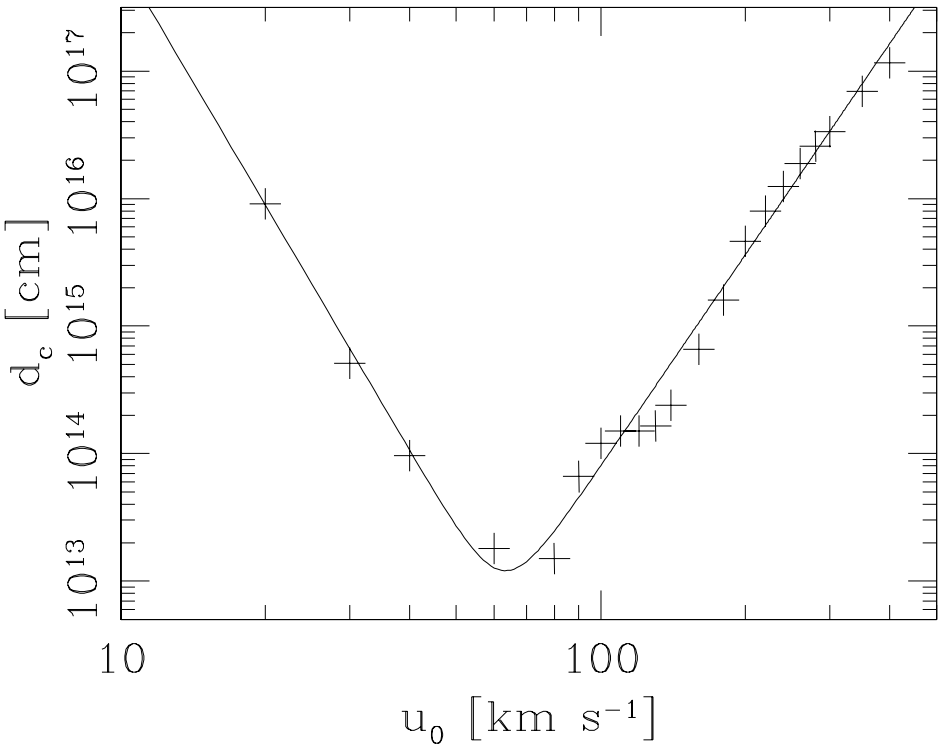

Figure 6.2: Cooling distance (to 10^4 K) as a function of shock velocity u_0 for shocks with a pre-shock number density $n_0 = 100$ cm^{-3} (values from Hartigan et al. 1987).

function of the shock velocity ($f(u_0)$, see Eq. 6.23) and the pre-shock density n_0. If one looks at the predictions of the radiative shock models of Hartigan et al. (1987), it is clear that the $d_c \propto n_0^{-1}$ scaling is indeed satisfied. The dependence of d_c on the shock velocity u_0 is shown in Fig. 6.2.

Different analytic fits to this d_c vs. u_0 dependence have been suggested in the literature. A possible fit (incorporating both the n_0 and the u_0 dependencies) is :

$$d_c = \left(\frac{100\,\mathrm{cm}^{-3}}{n_0}\right) \times$$

$$\left\{\left[3\times10^{11}\mathrm{cm}\right]\left(\frac{u_0}{100\,\mathrm{km\,s}^{-1}}\right)^{-6.4} + \left[8\times10^{13}\mathrm{cm}\right]\left(\frac{u_0}{100\,\mathrm{km\,s}^{-1}}\right)^{5.5}\right\}. \quad (6.24)$$

This fit is shown (together with the d_c values of Hartigan et al. 1987) in Fig. 6.2.

6.7 Preionisation

Shocks of velocity higher than ~ 100 km s^{-1} have a "radiative precursor". This is a region ahead of the shock wave in which ionising photons produced by the post-shock region photoionise the gas, producing a leading photoionised region (see Fig. 6.3). This region can be computed by solving the gasdynamic (6.1-6.3) and rate (6.8) equations, including the photoionisation rate and heating terms.

In this section, we present a simple, analytic model for this region (following Shull and McKee 1979). We first take the results from the shock models of Raymond et al. (1988), who give predictions of the flux F of ionising photons emitted into the pre-shock region as a function of the shock velocity u_0 and the pre-shock density n_0. The resulting $F/(n_0u_0)$ ratio (which is only a function of u_0) predicted from these models is plotted in Fig. 6.4. This function can be fitted with the interpolation :

$$\frac{F}{n_0u_0} = v_0^{2.8-0.6v_0}\,; \quad v_0 = \frac{u_0}{110\,\mathrm{km\,s}^{-1}} < 2.458\,,$$

$$= 3.293\,; \quad v_0 \geq 2.458\,. \quad (6.25)$$

A simple, Strömgren region argument gives the relation :

$$F = n_0u_0 + n_0^2\alpha_H d_p\,, \quad (6.26)$$

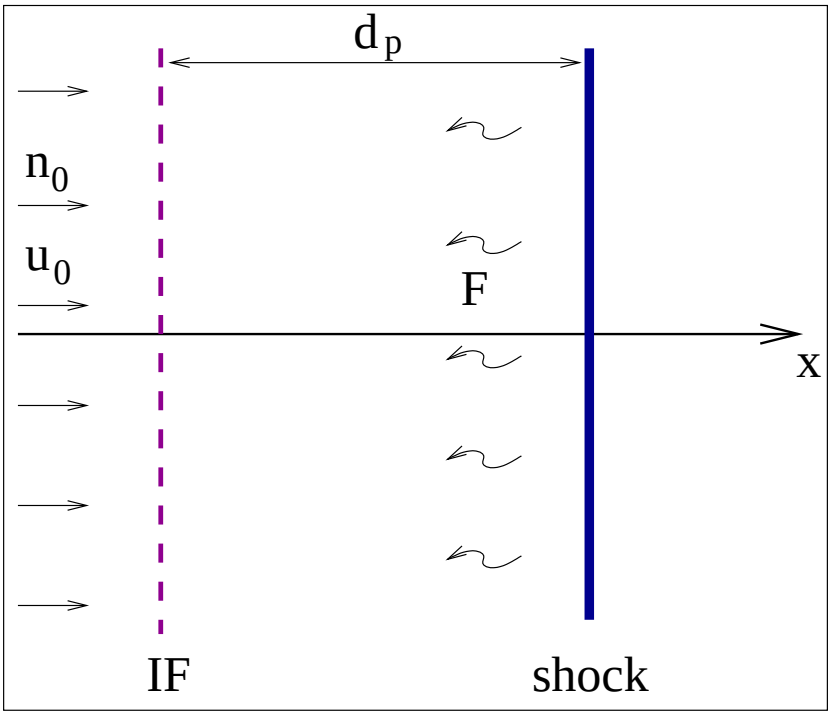

Figure 6.3: Schematic diagram showing the photoionisation region ahead of a shock wave. This region is preceded by an ionisation front (IF).

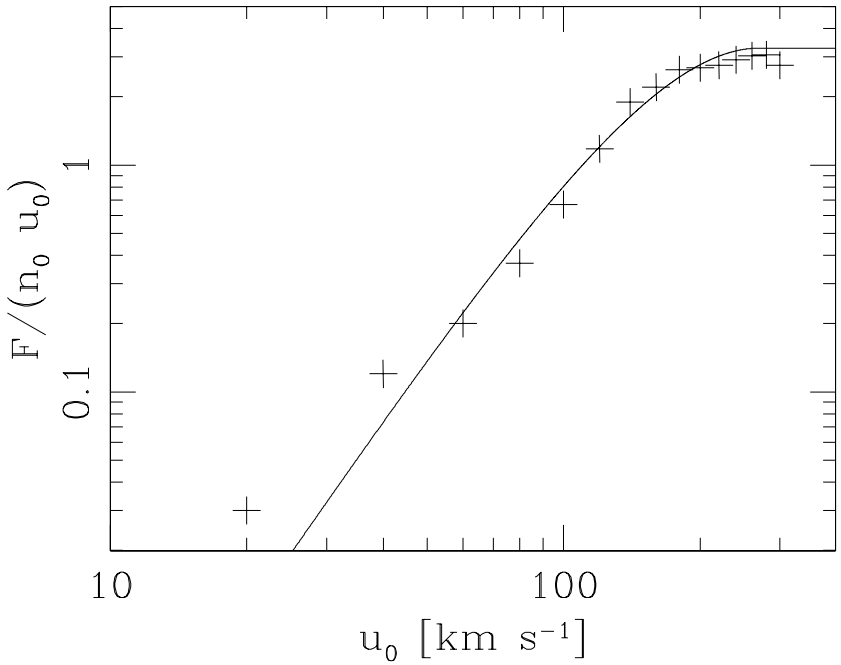

Figure 6.4: Flux F of ionising photons emitted by shock waves of different shock velocity u_0. Actually, the $F/(n_0 u_0)$ ratio is shown.

where d_p is the x-extent of the preionisation region (see Fig. 6.3), $\alpha_H \approx 2.56 \times 10^{-13}$ cm^{3}s^{-1} (see Eq. 1.13) is the H recombination coefficient, and $n_0 u_0$ is the flux of incoming neutrals. From this equation, we obtain :

$$d_p = \left[4.30 \times 10^{17}\mathrm{cm}\right] \left(\frac{100\,\mathrm{cm}^{-3}}{n_0}\right) v_0 \left(v_0^{2.8-0.6v_0} - 1\right) \; ; \quad v_0 = \frac{u_0}{110\,\mathrm{km\,s}^{-1}} \, . \tag{6.27}$$

The resulting d_p vs. u_0 relation is shown in Fig. 6.5. It is clear that $d_p = 0$ for $u_0 \leq 100$ km s^{-1}. In this shock velocity regime, the material entering the shock wave is only partially ionised, with the pre-shock H ionisation fraction given in an approximate way by

$$y_0 = \frac{F}{n_0 u_0} \, , \tag{6.28}$$

where the right hand side is given as a function of u_0 by Eq. (6.25). This ionisation fraction is shown (as a function of u_0) in Fig. 6.5.

6.8 The emission line spectra of shocks compared to photoionised regions

The optical emission line spectra of evolved supernovae remnants and of Herbig-Haro objects (both of which arise in shock waves with velocities of ~ 100 km s^{-1}) show lines of a wide range of ionisation energies. For example, collisionally excited lines of [O III], [O II] and [O I], lines of [C III], [C II] and [C I], and lines of [S III] and [S II]. Recombination lines of H and He are also seen. All of the collisionally excited lines cited above are strong (i. e., of intensities comparable to the ones of the H recombination lines).

Photoionised regions have qualitatively different spectra, with recombination lines of H and He and collisionally excited lines of ionised species, but with very faint lines of neutral (e. g., [C I] and [O I]) or low ionisation species (e. g., [S II]). The explanation for this is that C and O are at least singly ionised (and S twice ionised) within the Strömgren radius, and that outside the ionised region (where we do have C I and O I) the electron density is too small to produce an appreciable excitation of the levels giving rise to the emission lines. Therefore, in photoionised regions the emission of lines from neutrals come from the transition region around the Strömgren radius, where the gas is partially neutral (so that both neutrals and an appreciable electron

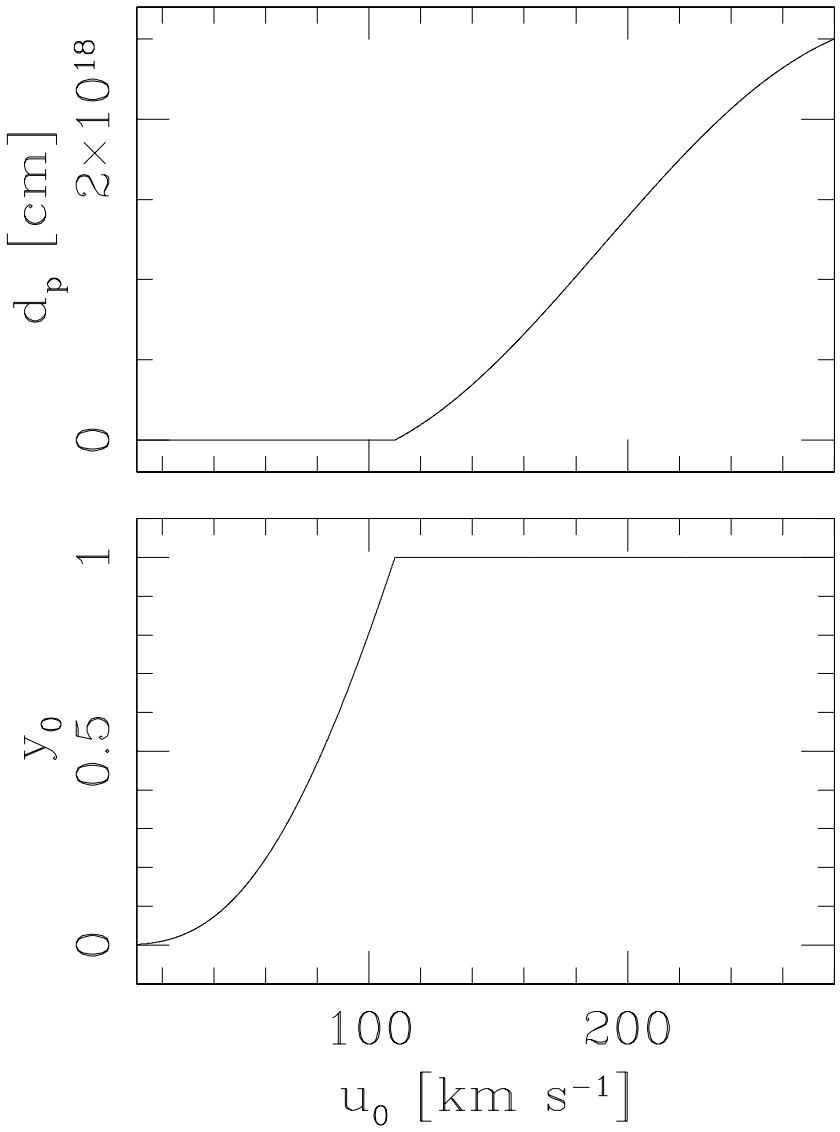

Figure 6.5: "Strömgren size" of the preionisation region d_p (top) and pre-shock H ionisation fraction y_0 (bottom) as a function of shock velocity u_0 for shocks with $n_0 = 100$ cm^{-3}.

density are present). Because this transition region is very narrow compared to the size of the photoionized region, the lines that exclusively come from the transition region are very faint compared to the lines produced within the bulk of the photoionized region.

On the other hand, the transition region between ionised and neutral gas is by far the densest part of a post-shock cooling region, so that its emission dominates the emission spectrum produced by the shock. The spectrum of a shock therefore corresponds to a transition region in which all ionisation states present (including neutrals) contribute strongly.

Chapter 7

The hydrodynamic expansion of an HII region

7.1 The final, pressure equilibrium configuration

Following the expansion to the initial Strömgren radius (see section 1.4.4), the hot, high pressure ionised region pushes away the cold, neutral surrounding gas. This expansion of the HII region stops when the photoionised gas has lowered its density enough so as to reach pressure equilibrium with the surrounding, undisturbed nuetral gas. This chapter describes the model derived in [16].

Let us consider a star with an ionising photon rate S_* in a uniform, neutral medium of density n_0 and isothermal sound speed c_0 ($c_0 \approx 1$ km s^{-1} for a 100 K environmental temperature). The initial, constant density expansion phase (section 1.4.4) leads to the formation of an ionised region of radius

$$R_S = \left(\frac{3S_*}{4\pi n_0^2 \alpha} \right)^{1/3} , \tag{7.1}$$

where $\alpha = 2.59 \times 10^{-13}$cm^{3}s^{-1} is the case B recombination coefficient of H at 10^4 K (see equation 1.8). The ionised region has a temperature $\sim 10^4$ K, so that its isothermal sound speed is $c_i \approx 10$ km s^{-1}.

The HII region will then expand until its number density (of atoms+ions) reaches a value n_f, determined by the condition of pressure equilibrium with

the surrounding environment :

$$n_f c_i^2 = n_0 c_0^2 \rightarrow n_f = n_0 \left(\frac{c_0}{c_i}\right)^2 . \tag{7.2}$$

The Strömgren radius of the pressure equilibrium configuration is then:

$$R_f = \left(\frac{3S_*}{4\pi n_f^2 \alpha}\right)^{1/3} = \left(\frac{c_i}{c_0}\right)^{2/3} R_S \, . \tag{7.3}$$

In other words, given that $c_i/c_0 \approx 10$ (see above), the final radius of the HII region (corresponding to the pressure equilibrium configuration) is ~ 5 times the initial Strömgren radius.

The mass of the final HII region then is :

$$M_f = \frac{4\pi R_f^3}{3} n_f 1.3 m_H = \left(\frac{c_i}{c_0}\right)^2 M_i \, , \tag{7.4}$$

where M_i is the mass within the initial Strömgren radius (before the hydrodynamic expansion), and $1.3m_H$ is the mass per atom/ion of a gas with a H fractional abundance (by number) of 0.9 and an He abundance of 0.1 . Therefore the mass of the HII region grows by a factor of ~ 100 as it evolves from the initial Strömgren radius to the final, pressure equilibrium configuration.

Interestingly, the expanding HII region pushes out an environmental mass

$$M_{env} \approx \frac{4\pi R_f^3}{3} n_0 1.3 m_H = \left(\frac{c_i}{c_0}\right)^2 M_f \, . \tag{7.5}$$

Therefore, the expanding HII region pushes out a mass M_f which is ~ 100 times larger than the mass $M_{ion} = M_f - M_i$. M_{ion} is the mass that was initially part of the neutral environment, which was photoionised (and therefore incorporated into the HII region) during the hydrodynamic expansion phase.

In this way, from the point of view of the neutral environment, the HII region acts as a piston, pushing out a mass $\sim M_{env}$ (see equation 7.5), and incorporating into the HII region only $\sim 1\%$ of this mass.

7.2 An analytic model for the expansion

We consider the problem of an HII region in its "hydrodynamic expansion phase", following the initial, constant density expansion to the "initial

Strömgren radius", given by equation (7.1). Once the ionization front has reached a radius R_S, the high temperature gas (of isothermal sound speed c_i and initial density n_0) starts to expand, pushing a shock into the surrounding environment (of sound speed c_0 and density n_0). If we assume that this shock is isothermal, and that it has a shock velocity v_s, the compression in the shock is $= M_0^2$, where $M_0 = v_s/c_0$. The velocity of the post-shock material relative to the shock therefore is

$$v_1 = v_s/M_0^2 \,. \tag{7.6}$$

If the ionization front moves at a velocity dR/dt (where R is the time-dependent radius of the photoionized region), the velocity v_s (with which the shock travels away from the source) is

$$v_s = \frac{dR}{dt} + v_1 = \frac{dR}{dt} + c_0^2/v_s \,, \tag{7.7}$$

where for the second equality we have used equation (7.6). Let us note that Dyson & Williams ([8]) assumed that $v_s = dR/dt$. From this equation, it is possible to find v_s as a function of dR/dt:

$$v_s = \frac{1}{2}\left[\frac{dR}{dt} + \sqrt{\left(\frac{dR}{dt}\right)^2 + 4c_0^2}\right] \tag{7.8}$$

and dR/dt as a function of v_s:

$$\frac{dR}{dt} = v_s - \frac{c_0}{v_s} \,. \tag{7.9}$$

We now assume that the expanding HII region is approximately homogeneous (of density n), and that it is in pressure balance with the shocked, neutral material:

$$nc_i^2 = n_0 v_s^2 \,, \tag{7.10}$$

and that it is in global photoionization equilibrium:

$$S_* = \frac{4\pi}{3} R^3 n^2 \alpha \rightarrow \left(\frac{n}{n_0}\right)^2 = \left(\frac{R_S}{R}\right)^3 \,, \tag{7.11}$$

where for deriving the second equality we have used the definition of the initial Strömgren radius (equation 1.8).

We now combine equations (7.9-7.11) to obtain :

$$\frac{1}{c_i}\frac{dR}{dt} = \left(\frac{R_S}{R}\right)^{3/4} + \sigma\left(\frac{R}{R_S}\right)^{3/4} , \tag{7.12}$$

where $\sigma = c_0^2/c_i^2$ is equal to 1/2 times the environment-to-ionized medium temperature ratio. If we set $\sigma = 0$ we regain the differential equation derived by Dyson & Williams ([8]).

With the boundary condition $R(t = 0) = R_S$, this equation can be integrated analytically to obtain :

$$t' = \frac{1}{3\sigma^{7/6}}\left[f(r) - f(1)\right] , \tag{7.13}$$

with

$$f(r) = -12\sigma^{1/6}r^{1/4} + 2\sqrt{3}\tan^{-1}\left(\frac{\sqrt{3}\sigma^{1/6}r^{1/4}}{1-\sigma^{1/3}r^{1/2}}\right)$$

$$+\ln\left[\frac{(\sigma^{1/3}r^{1/2} + \sigma^{1/6}r^{1/4} + 1)(\sigma^{1/6}r^{1/4} + 1)^2}{(\sigma^{1/3}r^{1/2} - \sigma^{1/6}r^{1/4} + 1)(\sigma^{1/6}r^{1/4} - 1)^2}\right] , \tag{7.14}$$

where $r = R/R_S$ and $t' = tc_i/R_S$.

It can be shown that for $\sigma = 0$ equation (7.13) coincides with the solution of the book of Dyson & Williams ([8]) :

$$t'_{DW} = \frac{4}{7}\left(r^{7/4} - 1\right) . \tag{7.15}$$

Figure 7.1 shows a comparison between the solution given (for different values of $\sigma = c_0^2/c_i^2$) by equation (7.13) and "Dyson's solution" (equation 7.15).

It is also possible to use the implicit $R(t)$ solution that we have derived (equation 7.13) to derive an equation of motion for the shock wave driven into the neutral medium. This is done by substituting the $R(t)$ solution into equation (7.12), and then inserting the derived $dR/dt(t)$ into equation (7.8). In this way, we obtain v_s as a function of t, and one can in principle integrate this equation numerically in order to obtain the radius of the shock wave as a function of time. This is done in the following section in order to compare the resulting prediction with the results of a gasdynamical simulation.

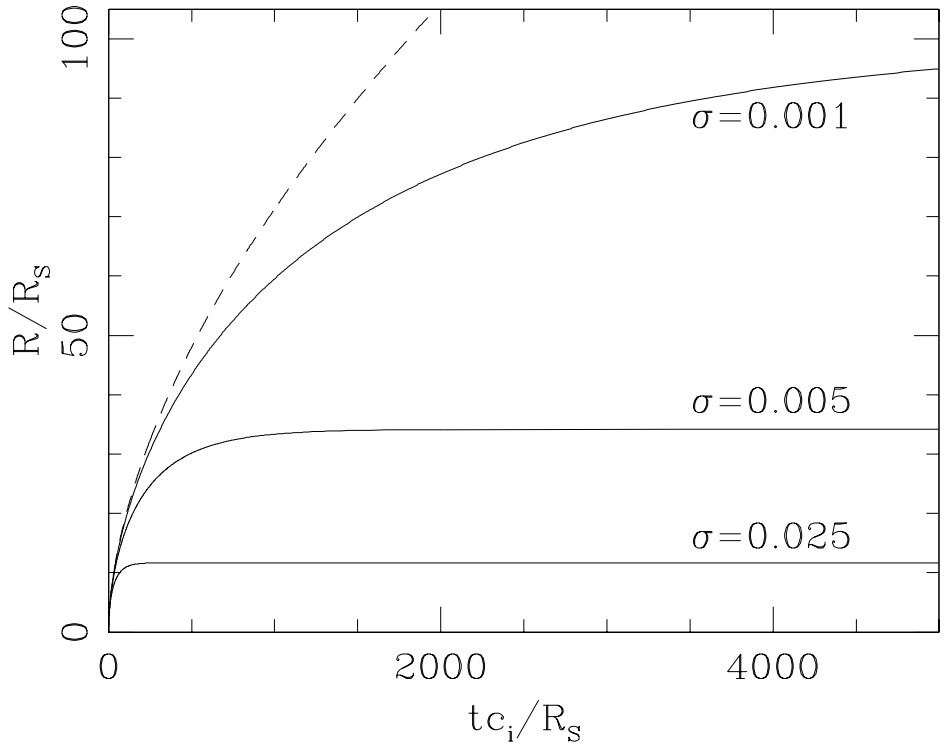

Figure 7.1: The solution for an expanding HII region into a pressureless, $\sigma = 0$ environment (Dyson's solution) is shown with a dashed line. The solid lines correspond to solutions with the σ values given by the corresponding labels.

7.3 Gasdynamic simulation

Let us now consider the gasdynamic equations for a spherically symmetric, two-temperature photoionized region:

$$\frac{\partial n}{\partial t} + \frac{\partial nu}{\partial R} + \frac{2nu}{R} = 0\,, \tag{7.16}$$

$$\frac{\partial nu}{\partial t} + \frac{\partial}{\partial R}\left[n(u^2 + c^2)\right] + \frac{2nu^2}{R} = 0\,, \tag{7.17}$$

$$\frac{\partial n_{HI}}{\partial t} + \frac{\partial n_{HI} u}{\partial R} + \frac{2n_{HI} u}{R} = (n - n_{HI})^2 \alpha - n_{HI}\phi\,, \tag{7.18}$$

$$\phi = \frac{S_* \sigma_{\nu_0}}{4\pi R^2} e^{-\tau_{\nu_0}}\,; \quad \tau_{\nu_0} = \sigma_{\nu_0} \int_0^R n_{HI}\, dR'\,, \tag{7.19}$$

where R is the spherical radius, u the (radial) fluid velocity, n is the number density of the (pure H) gas, n_{HI} is the neutral H number density, $n - n_{HI}$ is the ionized H density (equal to the electron density), $\alpha = 2.59 \times 10^{-13}$erg cm^{3}s^{-1} is the case B recombination coefficient of H at 10^4 K. The photoionization rate ϕ is computed in the standard "grey HII region" approximation (in which the frequency dependence of the photoionization cross section σ_ν is not considered), so that it is given (as a function of the ionizing photon rate S_* and the Lyman limit HI photoionization cross section $\sigma_{\nu_0} = 6.3 \times 10^{-18}$cm^2) by equation 7.19). Finally, the sound speed is computed as a function of the neutral fraction of the gas as :

$$c = \left(\frac{n_{HI}}{n_H}\right) c_0 + \left(1 - \frac{n_{HI}}{n_H}\right) c_i\,, \tag{7.20}$$

with $c_i = 10$ km s^{-1} (the isothermal sound speed of the ionized gas) and $c_0 = 1$ km s^{-1} (the sound speed of the external, neutral gas).

We compute a model with $S_* = 10^{49}$ s^{-1} (the ionizing photon rate of an O7 main sequence star). We initialize the spherical computational domain with a uniform, $n = 10^7$cm^{-3} number density. Initially, we set $n_{HI} = 0$ for $R \leq R_S$ and $n_{HI} = n$ for $R > R_S$, where $R_S = 4.52 \times 10^{15}$cm is the Strömgren radius obtained with the chosen values of S_* and n.

With these initial conditions, equations (7.16-7.19) are integrated in a spherical computational grid of 2000, equally spaced grid points extending from $R = 0$ to an outer radius $R_{out} = 10^{18}$cm. This outer radius is large enough to contain all perturbations within the computational domain.

Figure 7.2 shows the (R, t)-plane density stratification obtained from this simulation. The flow develops a low density, ionized region with a decreasing expansion velocity. The ionized region reaches its maximum outer radius at $t \approx 5.5 \times 10^4$yr, and then its radius decreases slowly with time, and finally stabilizes at a constant value for $t > 1.3 \times 10^5$ yr.

Also shown in Figure 7.2 are the analytic solution for the radius of the ionized region (equation 7.13) and the corresponding radius of the shock propagating into the neutral gas (obtained by integrating numerically equation 7.8, see the last paragraph of section 2). It is clear that the analytic solution (equation 7.13) reproduces well both the initial expansion and the final radius of the photoionized region. The analytic solution, however, fails to reproduce the "overshoot" (i.e., the HII region with radius larger than the final radius) obtained in the numerical simulation for $t \sim 5 \times 10^4$ yr. Finally, in Figure 7.2 we also show Dyson's solution (see equation 7.15).

7.4 The timescale for convergence to the pressure equilibrium configuration

The analytic model presented above allows us to make a simple prediction of the timescale for the expansion to attain the final, pressure equilibrium configuration. Equation (7.12) can be written in the form :

$$t = \frac{R_f}{c_0} I \,, \tag{7.21}$$

with

$$I = \int_{\sigma^{2/3}}^{R/R_f} \left(\frac{1}{x^{3/4}} - x^{3/4} \right) dx \,, \tag{7.22}$$

where $R_f = R_S/\sigma^{2/3}$ is the final, pressure equilibrium radius of the HII region expansion (with R_S given by equation 1.8) and $x = R/R_f$ is the spherical radius in units of R_f.

In order to obtain a simple prediction of the relaxation timescale of the HII region expansion, we now assume that $\sigma = (c_0/c_i)^2 \ll 1$ (which is generally true for a $\sim 10^4$ K HII region expanding into a ~ 100 K neutral/molecular environment), and therefore set the lower limit of the I integral (equation 7.22) to zero. We can then evaluate the time t in which a given fraction R/R_f of the final radius is attained from equations (7.21-7.22).

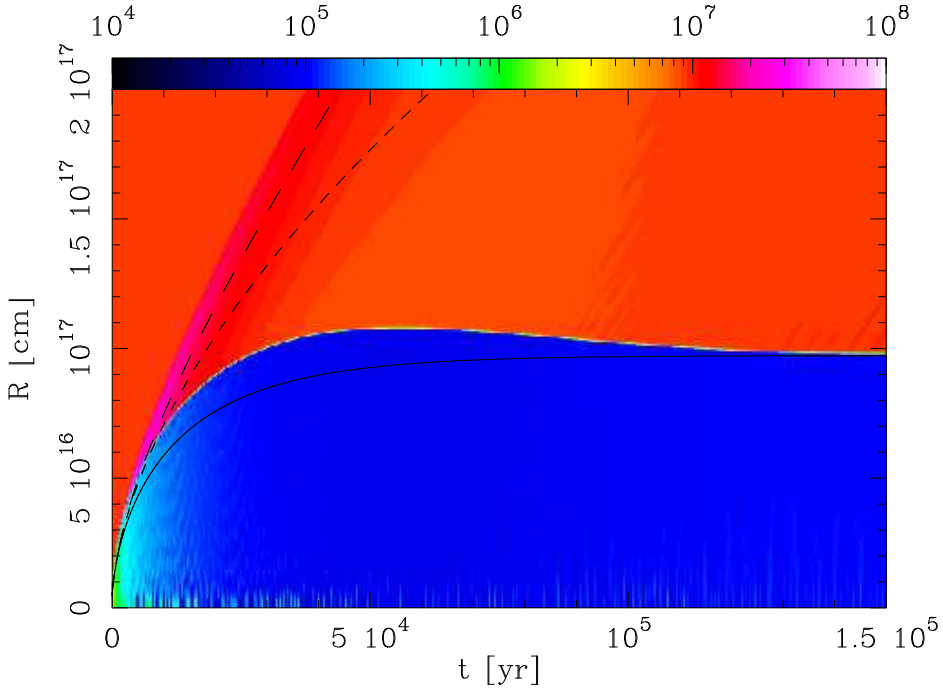

Figure 7.2: Density stratification in the (t, R)-plane of the numerical simulation described in the text. The low density region corresponds to the photoionised gas which first expands, and then reaches a final radius (determined by the pressure equilibrium of the ionised and neutral regions). The solid line is the prediction from the analytic model (equation 7.13) for the motion of the ionisation front, and the long-dash line the corresponding prediction for the motion of the shock wave. The short-dash line is Dyson's solution (equation 7.15). The density stratification is shown with the logarithmic scale given (in cm^{-3}) by the top bar.

For example, if we evaluate the I integral (equation 7.22, which has an analytic solution similar to the one given in equation 7.13), for $R/R_f = 0.8$ we obtain $I = I_8 = 0.7085$ and for $R/R_f = 0.9$ we obtain $I = I_9 = 1.1353$. Therefore, for obtaining an estimate of the timescale t_f in which the HII region attains $\sim$ 80-90% of its final radius R_f, we can set $I \approx 1$ in equation (7.21), which gives

$$t_f \approx 10^5\,\mathrm{yr}\,\left(\frac{R_f}{0.1\,\mathrm{pc}}\right)\left(\frac{1\,\mathrm{km\,s^{-1}}}{c_0}\right)$$

$$\approx 3\times 10^4\,\mathrm{yr}\,\left(\frac{S_*}{10^{49}\mathrm{s^{-1}}}\right)\left(\frac{10^7\mathrm{cm^{-3}}}{n_0}\right)^{2/3}\left(\frac{1\,\mathrm{km\,s^{-1}}}{c_0}\right)^{7/3}, \qquad (7.23)$$

where in the second equality we have set $c_i = 10$ km s^{-1}. Therefore, ultra compact HII regions (with radii of ~ 0.1 *pc*) have reached the final, pressure equilibrium configuration in a $t_f \sim 10^5$ yr timescale. Normal HII regions, with environmental densities $n_0 \sim 100$ cm^{-3} would reach the pressure equilibrium configuration in $\sim 6.5\times 10^7$ yr, which is close to 2 orders of magnitude larger than the main sequence lifetimes of the central O stars. Therefore, such regions will still be in the expansion phase when the central stars end their life in a SN explosion.

Chapter 8

Wind-driven HII regions

8.1 The general problem

HII regions are produced by the photoionization of the ISM due to the radiation of a massive O or B star. These stars also eject a stellar wind (see table 1.1), which pushes the surrounding ISM into a higher pressure, shell structure. In order to have a more realistic model for the expansion of an HII region, it is necessary to consider the effect of this wind (together with the photoionization process).

This problem has been described in some detail in the review paper of Capriotti & Kozminski [6], as well as in the book of Dyson & Williams [8]. The more detailed model of [17] is presented in the following sections.

8.2 The flow configuration

We assume that we have the flow configuration shown in Figure 8.1:

1. a star has an isotropic wind (of mass loss rate $\dot{M}$ and terminal velocity v_w) which is turned on at $t = 0$. At a time $t > 0$ the wind fills the inner, spherical region labeled "I" in the schematic diagram. The star also emits S_* ionizing photons per unit time (starting at $t = 0$). The outer boundary of this region is a spherical shock, which has a radius much smaller than the ones of all of the other regions of the flow,

2. the shocked stellar wind produces a hot bubble of coronal gas (region II, which is non-radiative for the case of an O/B central star) limited

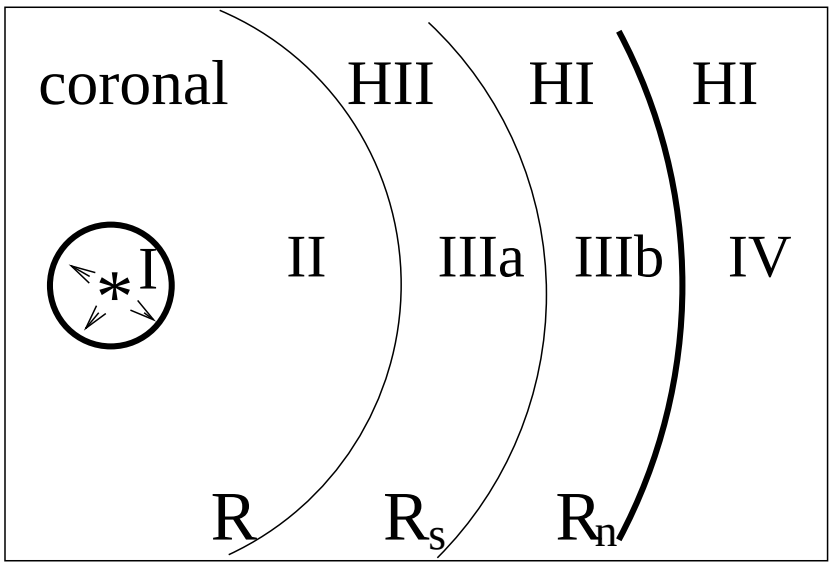

Figure 8.1: Schematic diagram of a wind-driven HII region. The asterisk indicates the position of the ionizing photon+stellar wind source. Region I is filled with the expanding stellar wind, ending at an outer shock (thick, inner circle). Region II is filled with the hot, shocked wind, and ends in a contact discontinuity (at a radius R). Region IIIa is the photoionized region (of outer radius R_S). Region IIIb is the perturbed, neutral environment region, pushed out by the outer shock (of radius R_n), which travels into the unperturbed environment (region IV).

on the outside by a contact discontinuity which separates the stellar wind from disturbed environmental material,

3. the hot bubble pushes out a shock wave (the outer boundary of region III in the schematic diagram) into the surrounding, neutral environment (region IV). The shell of displaced environmental material has an inner region (region IIIa) which is photoionized by the S_* ionizing photon rate of the central star, and a neutral outer region (region IIIb).

We first assume that region IIIa (the HII region) is much thinner than region IIIb (the region filled with shocked, neutral material, see Figure 8.1). For this "thin HII region" case, one can derive a model resulting in a first order differential equation with an approximate analytic solution. This model is described in section 8.3.

We then remove this assumption, and derive a "thick HII region" model, which results in a differential equation which we integrate numerically. This model is described in section 8.4.

8.3 Thin HII region model

8.3.1 Derivation of the model equation

As described in section 8.2, we assume that the stellar wind goes through a shock, and fills in a large bubble of hot, coronal gas. The kinetic energy of the wind feeds the thermal energy of the bubble and the kinetic energy of the swept-up material. The resulting energy equation is:

$$\frac{\dot{M} v_w^2}{2} t = \frac{3}{2} PV + \frac{1}{2} M_s v_s^2 \,, \tag{8.1}$$

where $\dot{M}$ is the mass loss rate and v_w the terminal velocity of the wind, P and V are the pressure and volume (respectively) of the stellar wind bubble and M_s and v_s are the mass and velocity (respectively) of the swept-up shell.

Following the classical derivation (see [8]), we use the estimates

$$P \approx \rho_0 \dot{R}^2 \,, \;\; M_s \approx \frac{4\pi}{3} R^3 \rho_0 \,, \;\; v_s \approx \dot{R} \,, \tag{8.2}$$

where R is the outer radius of the hot bubble (so that $V = 4\pi R^3/3$).

Combining equations (8.1-8.2), we obtain an energy conservation equation of the form:

$$\frac{\dot{M} v_w^2}{2} t = \frac{8\pi}{3} R^3 P \;\; \rightarrow \;\; P = \frac{3 \dot{M} v_w^2 t}{16 \pi R^3} \,, \tag{8.3}$$

for a bubble of uniform pressure P and radius R at an evolutionary time t.

The relations in equation (8.2) are strictly valid for the case in which the swept-up material (regions IIIa and IIIb in figure 8.1) forms a thin shell. However, we will apply equation (8.3) for the case in which region IIIb (of neutral swept-up gas, see figure 8.1) is not thin. This is not likely to result in large errors because the thermal energy of the shell dominates over the kinetic energy of the shell by a factor of ≈ 3. Therefore, an incorrect estimate of the kinetic energy of the (no longer thin) shell does not introduce large errors in the energy equation.

We now follow the derivation of Chapter 7, and assume that the outer shock (driven by the swept-up shell into the undisturbed environment) is isothermal, so that the postshock velocity v_{ps} and pressure P_{ps} are given by the isothermal Rankine-Hugoniot relations:

$$v_{ps} = \frac{c_0^2}{v_n}\,, \quad P_{ps} = \rho_0 v_n^2\,, \tag{8.4}$$

where v_n is the shock velocity and ρ_0 the ambient density. In the following, we set $P_{ps} = P$ (where P_{ps} is the post-shock pressure, see equation 8.4 and P the pressure of the hot bubble, see equation 8.3).

Also, from the standard "shock pushed by a piston" problem, we have the relation

$$v_n = v_{ps} + \dot{R}\,, \tag{8.5}$$

where $\dot{R}$ is the velocity of the outer edge of the hot bubble.

Now, combining equations (8.3-8.5), we obtain the differential equation:

$$\frac{dr}{d\tau} = \left(\frac{\tau}{r^3}\right)^{1/2} - \left(\frac{r^3}{\tau}\right)^{1/2}\,, \tag{8.6}$$

where $r = R/R_0$ (the dimensionless radius of the bubble) and $\tau = t/t_0$ (dimensionless time) with:

$$R_0 \equiv \sqrt{\frac{3\dot{M}v_w^2}{16\pi\rho_0 c_0^3}}\,, \quad t_0 \equiv \frac{R_0}{c_0}\,, \tag{8.7}$$

where c_0 is the isothermal sound speed of the undisturbed environment.

Once a solution $r(\tau)$ to equation (8.6) has been found, the outer radius R_n of the perturbed, neutral environment (region IV of figure 8.1) can be found by combining equations (8.4-8.5) to obtain

$$\frac{dr_n}{d\tau} = \left(\frac{\tau}{r^3}\right)^{1/2}\,, \tag{8.8}$$

where $r_n = R_n/R_0$ and r comes from the previously obtained solution (of equation 8.6). Equation (8.8) can then be integrated to obtain the (dimensional) radius $R_n = R_0 r_n$ of the spherical shock travelling into the neutral environment.

For parameters appropriate for a high density, ultracompact HII powered by a main sequence O7 star we have

$$R_0 = 0.76\,\mathrm{pc}\left(\frac{\dot{M}}{5\times10^{-7}\mathrm{M}_\odot\mathrm{yr}^{-1}}\right)^{1/2}$$

$$\left(\frac{v_w}{2500\,\mathrm{km\,s}^{-1}}\right)\left(\frac{10^7\,\mathrm{cm}^{-3}}{n_0}\right)^{1/2}\left(\frac{1\,\mathrm{km\,s}^{-1}}{c_0}\right)^{3/2}, \tag{8.9}$$

where n_0 is the number density of atomic nuclei. From this value of R_0 we can calculate the characteristic time $t_0 = R_0/c_0 \approx 7\times10^5$ yr. Therefore, ultracompact HII regions (with sizes of $\sim$ 0.1 pc and evolutionary times $\sim 10^5$ yr) are in a regime with a dimensionless radius $r = R/R_0 \sim$ 0.1-1 and a dimensionless time $\tau = t/t_0 \sim$ 0.1-1.

8.3.2 Numerical and analytic solutions

Equation (8.6) can be integrated numerically with the initial condition $r(0) = 0$ to obtain the radius R of the hot bubble as a function of time, and an integration of equation (8.8) gives the radius R_n of the outer shock vs. t. The results of such integrations are shown in Figure 8.2.

It is possible to find a series of approximate analytic solutions to equation (8.6). For $\tau \ll 1$ the first term on the right hand side of equation (8.6) dominates over the second term, and (neglecting the second term) one then obtains the integral

$$r(\tau) = \left(\frac{5}{3}\right)^{2/5}\tau^{3/5}, \tag{8.10}$$

which is the classical solution for an expanding, wind-driven bubble (see [8]).

For $\tau \gg 1$, the two terms on the right hand side of equation (8.6) become very large, reaching an approximate balance. Setting these two terms equal to each other, one obtains the solution

$$r(\tau) = \tau^{1/3}. \tag{8.11}$$

It can be straightforwardly shown that this solution corresponds to a bubble in pressure equilibrium with the surrounding environment, expanding quasi-statically as more material is progressively injected by the stellar wind.

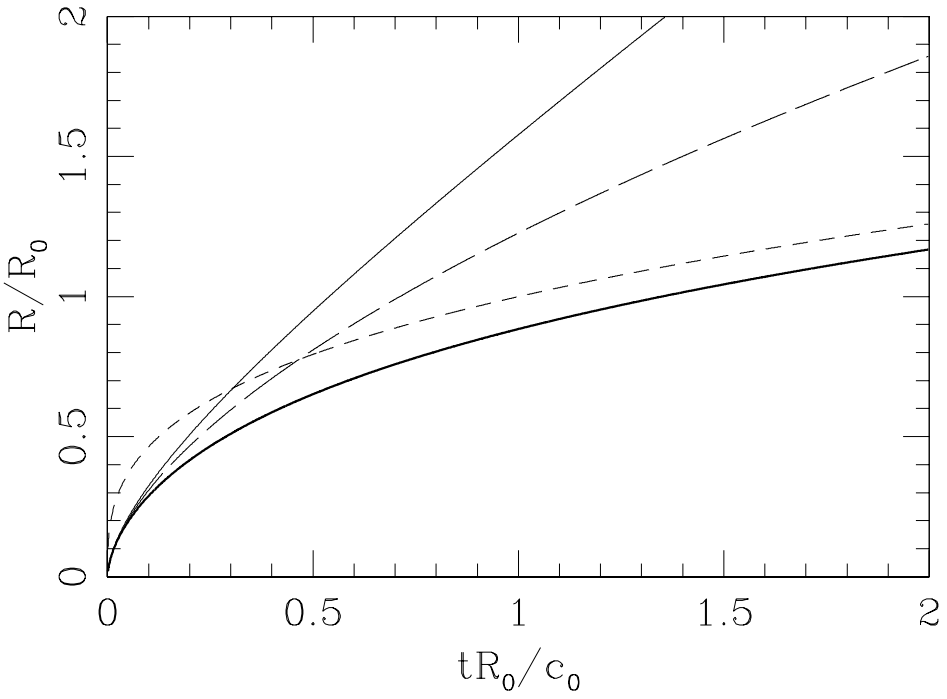

Figure 8.2: Radius R of the thick shell (thick, solid line) and R_n of the outer shock (thin, solid line) resulting from a numerical integration of equations (8.6) and (8.8). The radii are given in units of R_0 (see equation 8.9) and the time in units of R_0/c_0 (where c_0 is the isothermal sound speed of the surrounding, neutral environment). The long-dash line shows the inner analytic solution (equation 8.10, valid for $R \ll R_0$) and the short-dash line the outer analytic solution (equation 8.11, valid for $R \gg R_0$).

In Figure 8.2 we see that (as expected) the numerical integration of equation (8.6) gives a radius that approaches the low τ (equation 8.10) and high τ (equation 8.11) solutions in the appropriate limits. It is possible, however, to obtain approximate analytic solutions that reproduce the numerical solution for all values of τ.

To find these approximate solutions, we first rewrite equation (8.6) in the form:

$$\frac{dy}{dx} = \frac{3\,(x^2 - y^2)}{y^{2/3}}\,, \tag{8.12}$$

with $x = \tau^{1/2}$ and $y = r^{3/2}$. This equation can be straightforwardly solved

to obtain x as a function of dx/dy and y, and the resulting relation can then be used to do successive iterations of the form:

$$x_{n+1} = \sqrt{y^2 + \frac{y^{2/3}}{3(dx_n/dy)}}\,, \tag{8.13}$$

to obtain increasingly more accurate approximations to the $y(x)$ solution of equation (8.12).

Let us call $x_0(y)$ the first approximation to the solution of (8.12). One possibility is to set $x_0(y)$ equal to the large τ solution (equation 8.11), which in terms of the x, y variables takes the form

$$x_0(y) = y\,. \tag{8.14}$$

Inserting this relation in equation (8.13), we obtain the first iteration:

$$x_1(y) = \sqrt{y^2 + \frac{1}{3}y^{2/3}}\,. \tag{8.15}$$

Reinserting $x_1(y)$ in (8.13) we then obtain the second iteration:

$$x_2(y) = \sqrt{y^2 + \frac{3y\sqrt{y^2 + \frac{1}{3}y^{2/3}}}{1 + 9y^{4/3}}}\,. \tag{8.16}$$

It is possible to proceed with further iterations, but the resulting $x(y)$ relations are very extended.

A second possibility is to use the small τ solution (equation 8.10) as the first guess. The iterations then proceed as follows:

$$x_0(y) = \left(\frac{3}{5}\right)^{1/3} y^{5/9}\,, \tag{8.17}$$

$$x_1(y) = \sqrt{y^2 + \left(\frac{3}{5}\right)^{2/3} y^{10/9}}\,, \tag{8.18}$$

$$x_2(y) = \sqrt{y^2 + \frac{y^{2/3}\sqrt{y^2 + \left(\frac{3}{5}\right)^{2/3} y^{10/9}}}{3\left[y + \frac{1}{3}\left(\frac{5}{3}\right)^{1/3} y^{1/9}\right]}}\,. \tag{8.19}$$

The two "second iteration" solutions (equations 8.16 and 8.19) are shown (together with the results from a numerical integration of equation 8.6) in the top panel of Figure 8.3.

In order to evaluate the accuracy of our two "second iteration" solutions (equations 8.16 and 8.19), we first calculate the corresponding τ vs. r relations, and then calculate the relative error in the radius

$$\epsilon(\tau) = \left| \frac{r_e(\tau) - r_2(\tau)}{r_e(\tau)} \right| , \tag{8.20}$$

where $r_e(\tau)$ is the "exact" solution (obtained from a an accurate numerical integration of equation 8.6) and $r_2(\tau)$ is one of the two "second iteration" approximate solutions (equations 8.16 and 8.19).

The two corresponding relative errors are plotted as a function of time in the bottom panel of Figure 8.3. From this graph we see that the approximate solution given by equation (8.16) has a maximum deviation from the exact solution of $\sim 10\%$, and that the more complex approximate solution given by equation (8.19) has a maximum deviation of $\sim 5\%$.

8.4 Thick HII region model

8.4.1 Derivation of the model equation

We now develop a similar model to the one of section 8.3.1, but relaxing the condition that the photoionized region (region IIIa in Figure 8.1) is narrow. If we assume photoionization equilibrium (correct for all HII regions, see [15]), the outer radius R_S of the photoionized region obeys the relation:

$$S_* = \frac{4\pi}{3} n_i^2 \alpha_H \left(R_S^3 - R^3 \right) , \tag{8.21}$$

where R is the radius of the hot bubble (region II of Figure 8.1), n_i is the ion number density of region IIIa (assumed to be homogeneous within the region), S_* is the rate of photoionizing photons (emitted by the central star), $\alpha_H \approx 2.6 \times 10^{-13} \mathrm{cm^3 s^{-1}}$ is the case B hydrogen recombination coefficient at 10^4K.

The conditon of pressure equilibrium between the photoionized region and the hot bubble is

$$P = \overline{m} n_i c_i^2 , \tag{8.22}$$

where P is the pressure of the stellar wind bubble (see equation 8.3), c_i (≈ 10 km s^{-1}) is the isothermal sound speed of the photoionized gas and $\overline{m}$ is the average mass per ion ($= 1.3 m_H$ for a 90% H, 10% He gas, by number).

Also, the condition of pressure equilibrium between regions IIIa (the photoionized region) and IIIb (the shocked, neutral region) implies that

$$P = \rho_0 v_n^2 \,, \tag{8.23}$$

where we have used the isothermal shock jump conditions (equation 8.4). As described in section 3.1, v_n is the velocity of the outer shock driven into the undisturbed environment.

Finally, the "shock pushed by a piston" relation (equation 8.5) now takes the form:

$$v_n = v_{ps} + \dot{R}_S = \frac{c_0^2}{v_n} + \dot{R}_S \,, \tag{8.24}$$

where $\dot{R}_S$ is the velocity of the outer edge of the photoionized region, and for obtaining the second equality we have used equation (8.4).

Combining equations (8.3) and (8.21-8.24), we obtain a differential equation for R_S of the form:

$$\frac{1}{c_0}\frac{dR_S}{dt} = \sqrt{\frac{P}{\rho_0 c_0^2}} - \sqrt{\frac{\rho_0 c_0^2}{P}} \,, \tag{8.25}$$

where

$$\frac{P}{\rho_0 c_0^2} = \lambda \left(\frac{R_f}{c_0} t\right) \left(\frac{R_f}{R_S}\right)^3 + \sqrt{\left(\frac{R_f}{c_0}\lambda t\right)^2 \left(\frac{R_f}{R_S}\right)^6 + \left(\frac{R_f}{R_S}\right)^3} \,. \tag{8.26}$$

The solutions of equations (8.25-8.26) depend on the value of the dimensionless parameter

$$\lambda \equiv \frac{1}{2}\left(\frac{R_0}{R_f}\right)^2 \,, \tag{8.27}$$

where R_0 is given by equations (8.7,8.9) and

$$R_f = \left(\frac{3 S_*}{4\pi n_0^2 \alpha_H}\right)^{1/3} \left(\frac{c_i}{c_0}\right)^{4/3} \,. \tag{8.28}$$

R_f is the final radius obtained by a "wind-less" HII region which has reached pressure equilibrium with a surrounding, homogeneous neutral environment (see, e. g., the book of Dyson & Williams [8]). For parameters appropriate for an ultracompact HII region powered by an O7 star, we have

$$\lambda = 290 \left(\frac{\dot{M}}{5 \times 10^{-7} \mathrm{M}_{\odot} \mathrm{yr}^{-1}} \right)^{1/2} \left(\frac{v_w}{2500 \, \mathrm{km \, s^{-1}}} \right)^2 \left(\frac{10^7 \, \mathrm{cm^{-3}}}{n_0} \right)^{1/3} \left(\frac{10^{49} \, \mathrm{s^{-1}}}{S_*} \right)^{2/3} \left(\frac{1 \, \mathrm{km \, s^{-1}}}{c_0} \right)^{1/3} \left(\frac{10 \, \mathrm{km \, s^{-1}}}{c_i} \right)^{8/3} . \quad (8.29)$$

It is straightforward to see that equations (8.25-8.26) have the following two limits:

1. for $\lambda \gg 1$, these equations become equation (8.6) of section 3.1, i.e., the model for a wind-driven shell with a negligibly thin HII region,

2. for $\lambda = 0$, these equations are identical to the ones derived in chapter 7 for the expansion of an HII region in the absence of a stellar wind).

Therefore, by spanning all positive values of the dimensionless parameter λ, we have models ranging from a "wind-less" to a "wind dominated" expanding HII region.

In the following section we present numerical solutions (of equations 8.25-8.26) giving the radius R_S of the expanding HII region as a function of time. We also integrate equation (8.8) (setting $r = R_S/c_0$ in the right hand term) to obtain the radius R_n if the outer shock driven into the undisturbed environment, and combine equations (8.21-8.22) to obtain the radius of the hot bubble (region II of figure 8.1):

$$\left(\frac{R}{R_f} \right)^3 = \left(\frac{R_S}{R_f} \right)^3 - \left(\frac{\rho_0 c_0^2}{P} \right)^2 , \quad (8.30)$$

where the second term on the right is given by equation (8.26).

8.4.2 Numerical solutions

In Figure 8.4, we show the numerical results obtained from numerical integrations of the "thick HII region" model (described in section 4.1) for different values of the dimensionless parameter λ (see equations 8.27, 8.29). The $\lambda = 0$ solution (top left panel) is identical to the "wind-less expanding HII region" model of chapter 7. The $\lambda = 100$ solution is most similar to the "thin HII region" model described in section 3 (i.e., the solution shown in Figure 8.2).

As can be seen in Figure 8.4, for progressively larger values of λ, a larger, inner hot wind bubble and a narrower HII region are obtained. In order to evaluate the relative thickness of the HII region, we have computed the value of

$$\frac{\Delta R}{R_S} = \frac{R_S - R}{R_S}\,, \tag{8.31}$$

(where R_S and R are the outer radii of the HII region and of the hot bubble, respectively) as a function of t. The results are shown in Figure 8.5, in which we see that for $\lambda = 10$, the HII region has become a shell with a thickness of $\sim 1\%$ of the radius of the ionized nebula. For the $\lambda \sim 100$ value expected for ultracompact HII regions driven by a main sequence O star (see equation 8.29), the photoionized gas is confined to an extremely narrow shell (see figure 8.5).

8.5 Summary

In this chapter, we have applied the "thick shell" formalism of chapter 7 to the case of a source producing both a photoionizing radiation field and a stellar wind. For the case in which the HII region is thin (compared to the width of the swept-up ambient medium shell), the problem can be solved analytically with an iterative method. This method gives solutions which approximate the exact solution with accuracies of better than $\sim 5\%$ (see section 3.2). Our new solution to the wind-driven bubble expansion problem has a transition from a $R \propto t^{3/5}$ law (i.e., the "classical" solution, see [8]) for $R \ll R_0$ (see equation 8.9) to a $R \propto t^{1/3}$ law for $R \gg R_0$. Ultracompact HII regions lie close to the transition between these two regimes.

The problem in which the HII region is not thin leads to a more complex differential equation, which we have integrated numerically (see sections 4.1 and 4.2). Different solutions are found for different values of the dimensionless parameter $\lambda \equiv R_0/(2R_f)$ (where R_0 is given by equation 8.9 and R_f

is the final, pressure equilibrium radius of an HII region from a wind-less source). For increasing values of λ, we obtain solutions ranging from the wind-less case ($\lambda = 0$) to solutions in which the HII region becomes a very thin shell (approaching the "thin HII region" analytic solutions derived in section 3.2).

The transition to the thin HII region regime (for increasing λ values) is shown in Figures 8.4 and 8.5. Interestingly, for the nominal parameters that we have chosen for an ultracompact HII region, we obtain $\lambda \approx 300$ (see equation 8.29), so that they are clearly in the "thin HII region" regime.

In order to illustrate the effect of a stellar wind on the characteristics of an HII region, in Figure 8.6 we show the HII region radius R_S and the expansion velocity (dR_S/dt) obtained for $\lambda = 0$ (i.e., a wind-less HII region), $\lambda = 290$ (the value obtained for our chosen ultracompact HII region parameters, see equation 8.29) and for $\lambda = 10$ (an arbitrary, intermediate λ value). From this figure we see that while for $\lambda = 0$ the expansion velocity falls below ≈ 1 km s^{-1} in ~ 500 yr, for $\lambda = 10$ the expansion velocity remains above ≈ 1 km s^{-1} for an evolutionary time $\sim 1.5 \times 10^5$ yr. For $\lambda = 290$, the expansion velocity remains above ~ 3 km s^{-1} for $\sim 2 \times 10^4$ yr and above ~ 2 km s^{-1} for $\sim 1.5 \times 10^5$ yr.

Interferometric observations show that some ultracompact HII regions have a "thick shell" morphology, with shell widths of $\sim$ 10-20% of the nebular radius (see [7]). Comparing this result with our predictions of the thickness of the HII region, we would conclude that these "thick shell" objects have a dimensionless parameter $\lambda < 1$ (see Figure 8.5).

However, from equation (8.29) and the table of main sequence O/B stellar parameters of Sternberg et al. [23], we see that HII regions (expanding into a $n_0 = 10^7 \mathrm{cm}^{-3}$, uniform environment) have $\lambda = 150 \rightarrow 670$, the lower limit corresponding to a B0 star, and the upper limit to an O3 star. If we lower the environmental density to $n_0 = 10^4 \mathrm{cm}^{-3}$, we would obtain a $\lambda = 15 \rightarrow 70$ range (see equation 8.29), still an order of magnitude higher than the λ values necessary for producing a "thick HII shell" morphology (see above and Figure 8.5).

Interestingly, the more recent paper of Marcolino et al. [11] calculates mass loss rates for O8 and O9 main sequence which are two orders of magnitude below previously obtained rates (such as the ones of Sternberg et al. [23], given in Table 1.1, see above). These new mass loss rates would imply that $\lambda \sim 1$ for late OV stars.

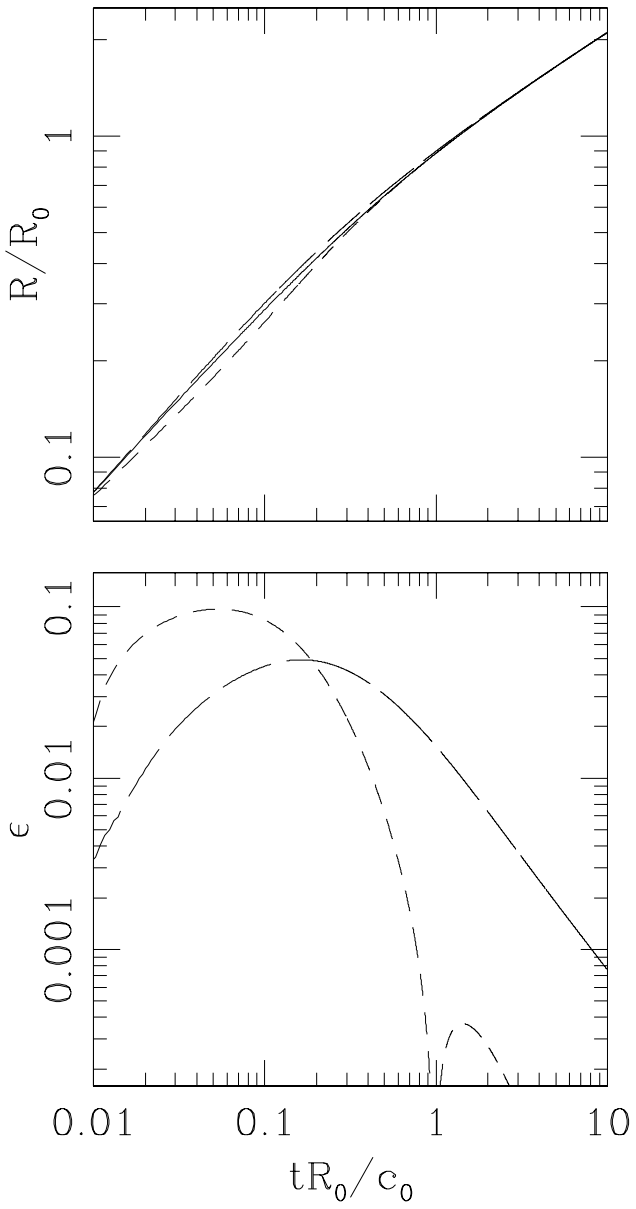

Figure 8.3: Top panel: radius of the hot bubble as a function of time obtained from the "exact" (i.e., numerical) solution of equation 8.6 (solid line) and the radii obtained from the two approximate analytic solutions (short dash: equation 8.16; long dash: equation 8.19). Lower panel: relative deviations (see equation 8.20) of equation 8.16 (short dash) and equation 8.19 (long dash) from the "exact" solution.

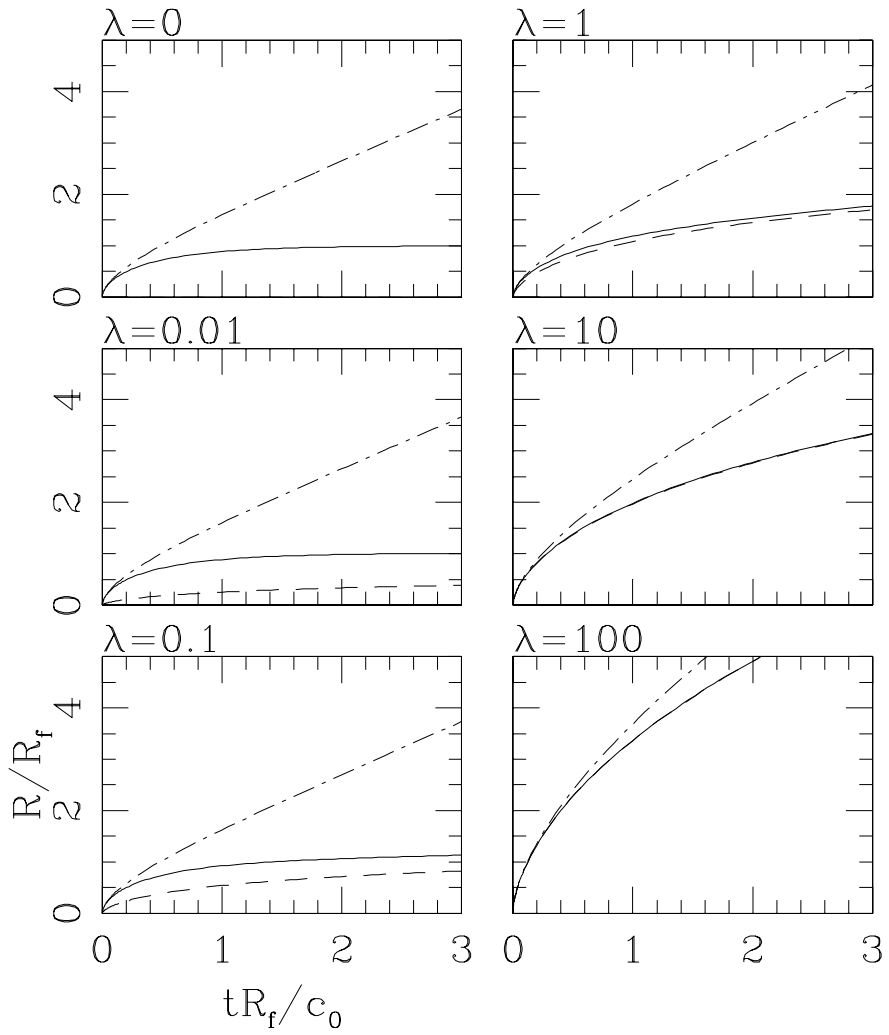

Figure 8.4: Hot bubble radius (dashed line), outer radius of the HII region (solid line) and radius of the shock driven into the surrounding environment (dash-dot line) as a function of time, obtained from numerical solutions of the "thick HII region model" of section 8.4. The six panels are labeled with the values of the dimensionless parameter λ (see equations 8.27, 8.29) used for each solution.

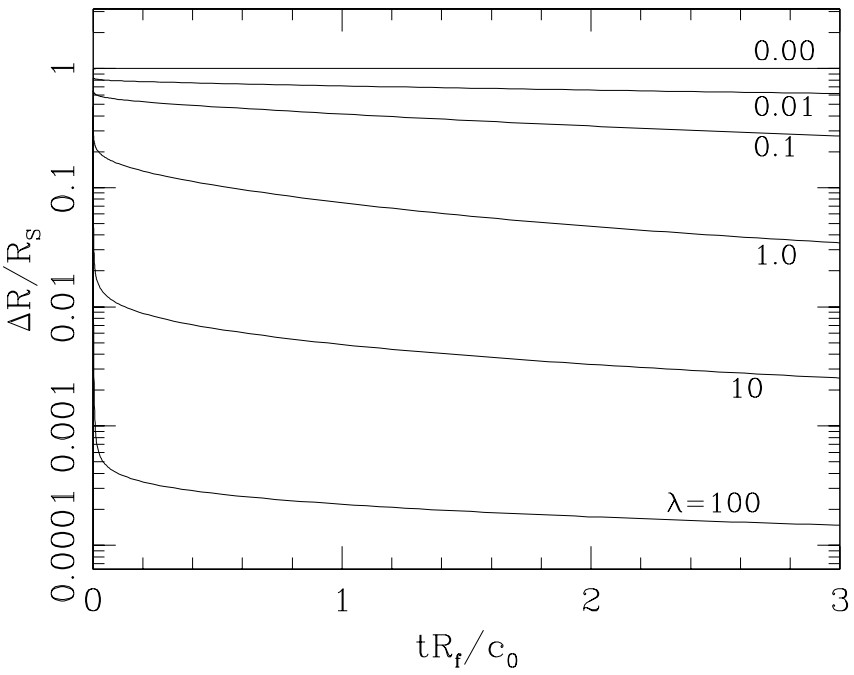

Figure 8.5: Relative width of the HII region (see equation 8.31) as a function of time obtained for different values of the dimensionless parameter λ (see equation 8.27).

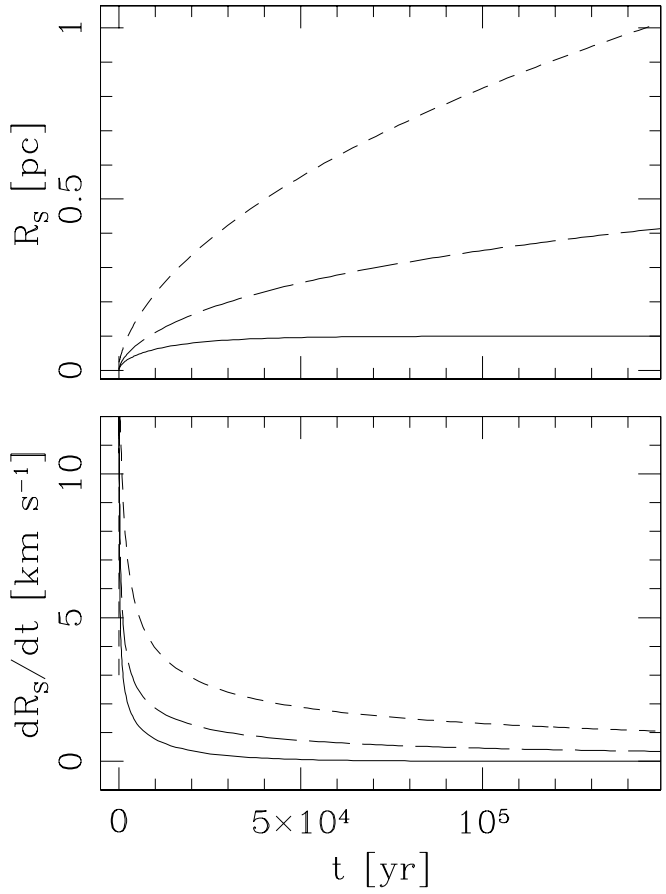

Figure 8.6: Outer radius of the HII region (top panel) and expansion velocity (lower panel) for an ultracompact HII region (of isothermal sound speed $c_i = 10$ km s^{-1}) driven by a source with $S_* = 10^{49}$s^{-1} into a uniform environent of density $n_0 = 10^7$cm^{-3} (and isothermal sound speed $c_0 = 1$ km s^{-1}). Three solutions are shown, corresponding to stellar winds such that the dimensionless parameter λ (see equations 8.27, 8.29) has values of 290 (short dash line), 10 (long dash line) and 0 (solid line).

Bibliography

[1] Abramowitz, M., Stegun, I. A. 1965, Handbook of Mathematical Functions (New York: Dover)

[2] Aldrovandi, S. M. V., Péquignot, D. 1973, A&A, 25, 137

[3] Aldrovandi, S. M. V., Péquignot, D. 1976, A&A, 47, 321

[4] Brocklehurst, M. 1971, MNRAS, 153, 471

[5] Brown, R. L., Mathews, W. 1970, ApJ, 160, 939

[6] Capriotti, E. R., Kozminski, J. F. 2001, PASP, 113, 677

[7] Carral, P., Kurtz, S.E., Rodríguez, L. F., Menten, K., Cantó, J., & Arceo, R. 2002, AJ, 123, 2574

[8] Dyson, J. E., Williams, D. A. 1997, IoP Publishing

[9] Hartigan, P., Raymond, J. C., Hartmann, L. W. 1987, ApJ, 316, 323

[10] Huggins, W. 1871, RSPS, 20, 379

[11] Marcolino, W. L. F., Bouret, J.-C., Martins, F., Hillier, D. J., Lanz, T., & Escolano, C. 2009, A&A, 498, 837

[12] Osterbrock, D. E. 1989, "Astrophysics of gaseous nebulae and active galactic nuclei" (Mill Valley: Univ. Sci. Books)

[13] Pengelly, R. M., Seaton, M. J. 1964, MNRAS, 127, 165

[14] Raga, A. C., Noriega-Crespo, A., Cantó, J., Steffen, W., Van Buren, D., Mellema, G., Lundqvist, P. 1997, RMxAA, 33, 73

[15] Raga, A. C., Cantó, J., Rodríguez, L. F. 2012, RMxAA, 48, 149

[16] Raga, A. C., Cantó, J., Rodríguez, L. F. 2012, MNRAS, 419, L39

[17] Raga, A. C., Cantó, J., Rodríguez, L. F. 2012, RMxAA, in press

[18] Raymond, J. C., Hartigan, P., Hartmann, L. W. 1988, ApJ, 326, 323

[19] Seaton, M. J. 1955, PPSA, 68, 457

[20] Seaton, M. J. 1959, MNRAS, 119, 81

[21] Seaton, M. J. 1960, Rept. Prog. Phys., 23, 313

[22] Shull, J. M., McKee, C. F. 1979, ApJ, 227, 131

[23] Sternberg, A., Hoffman, T. L., Pauldrach, A. W. A. 2003, ApJ, 599, 1333